Development and Experimental Investigation of a Helium Thermosiphon

by

Daniel C. Potratz

A thesis submitted in the partial fulfillment of the

requirement for the degree of

MASTER OF SCIENCE

(Mechanical Engineering)

at the

UNIVERSITY OF WISCONSIN-MADISON

2011

Approved:

Professor J.M. Pfotenhauer
Department of Mechanical Engineering
University of Wisconsin-Madison

Date

ABSTRACT

Development and Experimental Investigation of a

Helium Thermosiphon

Daniel C. Potratz

Under the supervision of Professors J.M. Pfotenhauer and F.K. Miller

Superconducting undulator insertion devices are currently under development at Argonne National Lab (ANL) for installation on the Advanced Photon Source (APS). Analyses have been carried out through the University of Wisconsin in conjunction with the APS-Magnetic Devices group on cooling schemes to maintain the superconducting windings below their current sharing temperature. The presented study focuses on the development of a helium thermosiphon running through the undulator cores and addresses several unique features of the design, including: the importance of sub-cooling associated with hydrostatic heating, the impact of a heat load primarily deposited along the horizontal channel, and two-phase flow characterization at extremely low quality conditions.

The experiment centers on the measurement of flow rates using a Venturi flow element in the sub-cooled region of the flow path. Thermal loads were applied along both the horizontal and vertical sections of the piping assembly. Flow measurements were recorded on two different test assemblies to mimic the proposed core geometry. The first sets of tests were run with a single channel making up the horizontal testing section; the second sets of tests were run with a three-channel test fixture oriented in two directions. These results were compared against a theoretical model and subsequently resulted in the determination of an anticipated heat transfer

coefficient. Data indicate that minor pressure losses dominate overall performance and that stand pipe placement has a considerable impact on flow stability. Furthermore, while the horizontal and vertical heat applications agree with modeled operating conditions in terms of an averaged signal, the observed flow behavior can vary widely in time.

ACKNOWLEDGEMENTS

First and foremost I would like to thank my advisors, Professors Pfotenhauer and Miller, for their continual guidance on this research. It has not always been easy given that the experiment took place on-site at ANL as opposed to the UW, but you both have been honest, challenging, and exceptionally helpful with any questions I have had. Much gratitude must also be extended to my colleagues at Argonne National Lab – namely Quentin Hasse, Matt Kasa, Kurt Boerste, Joel Fuerst Ph.D., Liz Moog Ph.D., Yury Ivanyushenkov Ph.D. and Bob Kustom Ph.D. All of you have outstanding knowledge of the project at hand and have been particularly patient yet questioning given the one-of-a-kind nature of this experiment. I would also like to acknowledge all of my office mates, but in particular Dan Schick, who will be continuing this work by focusing on the project's recondensing efforts. Finally I would like to thank my family for all their support through the years, and in particular my future wife Amanda for moving with me to Madison to continue on in school and supporting me in all my endeavors. And Ann.

This work was supported by Argonne National Laboratory under contract No. 9F-31982, and by the U. S. Department of Energy, Office of Science, under contract No. DE-AC02-06CH11357.

TABLE OF CONTENTS

Abstract…….. i

Acknowledgements…… iii

Table of Contents…….. iv

List of Figures…… vii

List of Tables……. x

Nomenclatures……... xi

1 Introduction……... 1

1.1 Objective…….. 1

1.2 Review of Undulator Insertion Devices and Subsequent Motivation……... 2

1.3 Competing and Contemporary Designs…… 6

1.4 References…… 10

2 Theory of Operation……. 11

2.1 Fundamental Thermosiphon Relationships……. 11

2.2 Two-Phase Flow Characteristics……... 25

2.3 Heat Transfer Characteristics……... 31

2.4 Instability Avenues……. 34

2.4.1 Horizontal Instabilities…… 34

2.4.2 Vertical Instabilities……. 35

2.5 Thermoacoustic Oscillations……. 36

2.6 References…… 46

3 Experimental Apparatus…….. 48

3.1 Experiment Description……. 48

3.1.1 Vacuum Chamber…… 49

3.1.2 Helium Vessel……... 50

3.1.3 Piping and Test Sections…….. 51

3.1.4 Venturi Flow Element…….. 52

3.1.5 Other Principal Components…….. 54

3.2 Experiment Instrumentation……. 54

3.2.1 Temperature Sensors……... 56

3.2.2 Heaters…….. 56

3.2.3 Liquid Level Indicator……. 59

3.2.4 Differential Pressure Transducer……... 59

3.2.5 Other Principal Electrical Equipment……... 60

3.3 Pressure Transducer Calibration…….. 60

3.4 Data Acquisition System……. 63

3.5 Experimental Procedure……. 63

3.6 References..…….. 66

4 Results…….... 67

4.1 Raw Data Discussion……... 67

4.2 Single Channel Results……... 69

4.3 Core Geometry Orientation 1 Results……... 74

4.4 Core Geometry Orientation 2 Results……... 79

4.5 Discussion and Recommendations……..…... 83

4.6 References…… 86

5 SCU Operation and Considerations…… 87

5.1 Anticipated SCU Flow Rate……... 87

5.2 Thermal Conductivity of the Core…… 91

5.2.1 Experimental Description and Test Procedure……. 91

5.2.2 Conductivity Discussion…….. 99

5.3 Lack of Flow/Stagnation…….……... 104

5.4 Finite Element Analysis and Design Modifications……. 105

5.5 References…… 110

6 Summary and Conclusions……... 111

6.1 Thermosiphon Design and Experiment…… 111

6.2 SCU Considerations…… 112

6.3 References…… 113

7 Appendices……..……... 114

7.1 Drawings…….. 114

LIST OF FIGURES

1.1. Photon beam exiting a beam-line shutter and interacting with a test specimen…… **3**
1.2. Two-dimensional electron movement and pulse formation occurring at relativistic speeds…….. **4**
1.3. Conventional ring layout of a synchrotron radiation facility…… **4**
1.4. Generic insertion device comparison…….. **4**
1.5. Conventional undulator brilliance curve……. **5**
1.6. Comparison of on-axis brightness between a conventional undulator A device and the superconducting undulator under development…… **6**
1.7. Superconducting undulator cryostat in use at ANKA……. **8**
1.8. Superconducting wiggler cooling system installed at the Diamond Light Source…. **8**
2.1. Pressure temperature diagram for helium with exaggerated pressure differences…. **11**
2.2. Comparison of friction factor correlations for use in the thermodynamic model…. **14**
2.3. Inlet loss coefficient as a function of geometry…….. **17**
2.4. Minor loss coefficient for a sudden expansion and contraction of in-flow elements. **17**
2.5. Secondary flow pattern for a 90^0 tube bend…… **18**
2.6. Cartoon representing thermosiphon operation and the impact of subcooling…….. **21**
2.7. Expected flow rates under different model conditions as a function of horizontal heat load for a single channel test……... **23**
2.8. Expected flow rates for 1.5 W heat load to single channel assembly as a function of head height…….. **23**
2.9. Expected vapor quality under different model conditions as a function of horizontal heat load for the three-channel test……..... **24**
2.10. Expected flow rates inside the three-channels under different operating conditions as a function of horizontal heat load for the three-channel test……. **24**
2.11. Traditional two-phase flow regimes……... **25**
2.12. Baker diagram for two-phase helium flow……..... **26**
2.13. Filippov flow map example for helium……... **26**
2.14. Graphic of equilibrium for stratified flow……... **27**
2.15. Anticipated flow pattern for single channel test……. **30**
2.16. Anticipated flow pattern for three-channel test…….. **30**
2.17. Anticipated heat transfer coefficient for single channel assembly……. **33**
2.18. Anticipated heat transfer coefficient for three-channel assembly……. **33**
2.19. Visual representation of geysering…….. **35**
2.20. Stability curves of helium for $\xi < 1$……. **42**
2.21. Stability curves of helium $\xi > 1$……... **42**
2.22. Anticipated temperature profile based on 304 SS conductivity data from NIST… **43**
2.23. Stability diagram of temperature profile vs. tube diameter for SCU feed through sizing……... **43**
3.1. Three dimensional, transparent representation of the experimental assembly……. **48**
3.2. Vacuum chamber used in experimental assembly……. **49**
3.3. Helium vessel and support structure……... **50**
3.4. Three-channel test assembly installation…… **51**

3.5. Single channel test assembly…….. **52**
3.6. Three-channel test assembly……... **52**
3.7. Venturi assembly section view……... **53**
3.8. Piping and instrumentation diagram for thermosiphon test apparatus…… **55**
3.9. Heaters installed on the three-channel assembly…… **57**
3.10. Horizontal test assembly covered in 20 layers of MLI…….. **57**
3.11. Kulite CT-190 installed with reference port extension……... **60**
3.12. Pressure transducer calibration schematic…….. **61**
3.13. Kulite CT-190 pressure transducer response at 4.2 K……. **62**
3.14. Kulite CT-190 pressure transducer response at 4.2 K referencing vacuum…… **62**
4.1a. Top core geometry orientation…… **67**
4.1b. Bottom core geometry orientation……. **67**
4.2. Transducer signal vs. horizontal heat load for top core geometry test…… **68**
4.3. Transducer signal vs. vertical heat load for top core geometry test…… **68**
4.4a. Average mass flow rate as a function of horizontal heat load for single channel test……... **70**
4.4b. Average mass flow rate as a function of horizontal heat load for single channel test……... **71**
4.5a. Average mass flow rate as a function of vertical heat load for single channel test… **72**
4.5b. Average mass flow rate as a function of vertical heat load for single channel test… **72**
4.6. Coefficient of variation as a function of horizontal heat load for single channel test **73**
4.7. Coefficient of variation as a function of vertical heat load for single channel test. **74**
4.8. Average mass flow rate as a function of horizontal heat load for three-channel test #1…… **75**
4.9. Coefficient of variation as a function of horizontal heat load for three-channel test #1……. **75**
4.10. Average mass flow rate as a function of vertical heat load for three-channel test #1. **76**
4.11. Coefficient of variation as a function of vertical heat load for three-channel test #1. **76**
4.12. Average mass flow rate as a function of combined heat load for three-channel test #1……. **78**
4.13. Coefficient of variation as a function of combined heat load for three-channel test #1……. **78**
4.14. Coefficient of variation as a function of power ratio (vertical/horizontal) for three-channel test #1……. **79**
4.15. Average mass flow rate as a function of horizontal heat load for three-channel test #2……. **80**
4.16. Coefficient of variation as a function of horizontal heat load for three-channel test #2……. **80**
4.17. Average mass flow rate as a function of vertical heat load for three-channel test #2. **81**
4.18. Coefficient of variation as a function of vertical heat load for three-channel test #2. **81**
4.19. Average mass flow rate as a function of combined heat load for three-channel test #2……. **82**
4.20. Coefficient of variation as a function of combined heat load for three-channel test #2……. **82**
4.21. Coefficient of variation as a function of power ratio (vertical/horizontal) for three-channel test #2……. **83**

5.1. Superconducting undulator cryostat with 42-pole cores……. **87**
5.2. Anticipated flow rate inside the undulator cores as a function of total thermosiphon heat load…….. **88**
5.3. Anticipated heat transfer coefficient as a function of total thermosiphon heat load.. **88**
5.4. Method to create annular channels using a wound coil as a spacer…….. **89**
5.5. Anticipated mass flow rate in the undulator cores as a function of hydraulic diameter for a constant heat load of 1.5 W…… **90**
5.6. Anticipated heat transfer coefficient in the undulator cores as a function of hydraulic diameter for a constant heat load of 1.5 W…… **90**
5.7a. Top core end-view…….. **91**
5.7b. Bottom core end-view……. **91**
5.8. Thermal conductivity test schematic……... **93**
5.9. Thermal conductivity test rig assembled…… **93**
5.10. Conductivity test rig radiation model…….. **96**
5.10. Temperature response of the thermal conductivity test…….. **98**
5.11. Thermal conductivity test results…… **101**
5.12. Thermal conductivity of 1006-1008 carbon steel as a function of average test temperature…….. **101**
5.13. Temperature response of thermal conductivity test…… **102**
5.14. Superconducting undulator core……. **103**
5.15. Bracket connection to SCU core from beam chamber…… **103**
5.16a. Simplified bracket geometry used in FEA…….. **105**
5.16b. Simplified core geometry used in FEA……... **105**
5.17. Temperature dependent thermal conductivities used in FEA……. **106**
5.18. Temperature profile of SCU core and bracket with a beam chamber temperature of 10 K……. **106**
5.19. Design modification extending the core past the first pole…… **108**
5.20. Design modification extending the bracket and trimming any face contact with the end poles……. **108**

LIST OF TABLES

2.1. Dimensions of test assembly used in modeling analysis…… **22**
2.2. The G-function for helium…….. **40**
3.1. Instrumentation schematic notation…… **56**
3.2. Heater characterization for three test runs…….. **58**
4.1. Listing of parameters used in mass flow and uncertainty calculations……... **69**
5.1. Finite element analysis results table…… **109**

NOMENCLATURE

Symbol

A	area
c	speed of sound
c	Kirchoff's constant of a gas
c_p	specific heat
C	variable used to define the horn region for TAO predictions
COV	coefficient of variation
d	diameter
d	Kramer's constant of a gas
D	numerical value used in defining right asymptote for TAO predictions
e	surface roughness
E_b	total blackbody emissive power
f	friction factor
F	view factor
$f_{Adjusted}$	friction factor adjusted for entry effects
$f_{Blasius}$	Blasius correlation friction factor
$f_{Colebrook}$	Colebrook correlation friction factor
f_{Huang}	Huang correlation friction factor
$f_{Petukhov}$	Petukhov correlation friction factor
f_T	Turbulent friction factor
g	gravity
G	mass flux
G_I	imaginary component of G-function
G_R	real component of G-function
h	enthalpy
h	liquid height
h	heat transfer coefficient
h_{DB}	heat transfer coefficient using the Dittus-Boelter correlation
$h_{J\text{-}TP}$	heat transfer coefficient using the Johannes two-phase correlation
J	radiosity
k	thermal conductivity
K	minor loss coefficient
K_{bend}	minor loss coefficient due to tube bend
K_{con}	minor loss coefficient due to converging
K_{div}	minor loss coefficient due to diverging
K_{SC}	minor loss coefficient due to sudden contraction
K_{SE}	minor loss coefficient due to sudden expansion
K_{tee}	minor loss coefficient due to tee fitting
L	length
$\dot{m}$	mass flow rate
n	coefficient
p	perimeter

PF	power factor
p_i	liquid-vapor interface length
Pr	Prandtl number
$\dot{Q}$	heat load
$\bar{\dot{Q}}_{applied}$	average applied heat load
$\bar{\dot{Q}}_{observed}$	average observed heat load
$\bar{\dot{Q}}_{parasitic}$	average parasitic heat load
R	radius
R	thermal resistance
R_{bend}	bend radius
Re	Reynolds number
S	steepness
T	temperature
$time$	time duration
U	superficial liquid velocity
U_A	uncertainty in accuracy of sensor
U_I	uncertainty in accuracy of current measurement
U_T	total uncertainty in measurement
U_V	uncertainty in accuracy of voltage measurement
V	velocity
w	width
x	integration variable
x	position
X	variable in defining the right asymptote for TAO predictions
X_{tt}	Leckhart-Martinelli parameter
Y	ratio of the tube radius to the Stokes boundary layer
z	vertical integration variable

Greek Symbols

α	two-phase adjustment parameter based on density
α	bend loss parameter
α	ratio of hot to cold mean temperatures
α_1	angle of convergence
α_2	angle of divergence
β	two-phase adjustment parameter based on viscosity
β	exponent of T in the power law dependence of viscosity
γ	specific heat ratio
ΔP	pressure drop
ΔP_A	acceleration pressure drop
ΔP_F	frictional pressure drop
ΔP_H	hydrostatic pressure drop
ΔP_{Minor}	minor loss pressure drop
ΔT	temperature difference
Δx	distance between two points
ε	interpolation variable for G-function
ε	emissivity

θ	stratification angle
$\lambda_{c,linear}$	asymptote parameter for TAO predictions
μ	dynamic viscosity
ξ	ratio of hot to cold lengths
ρ	density
σ	surface tension
σ	Boltzmann's constant
υ	specific volume
φ	two-phase friction multiplier
φ_f	void fraction
χ	vapor quality

Subscripts

ave	average
c	at the cold end
c	cross section
down	associated with down tube length
g	gram basis
H	at the hot end
heat	associated with heated length/location
horizontal	horizontal cross-section
inlet	associated with inlet
in	associated with inlet piping to test section
large	associated with larger diameter
liq	liquid
lower	referring to lower term error bar
o	baseline
out	associated with outlet piping to test section
return	return piping
s	surface
sat	saturation
small	associated with smaller diameter
subcooled	associated with subcooled length
supply	associated with supply piping
tot	total
throat	associated with throat diameter
upper	referring to upper term error bar
vap	vapor

1 Introduction

1.1 Objective

Currently, the Advanced Photon Source (APS) at Argonne National Lab (ANL) is undergoing an upgrade that will entail the installation of several new types of insertion devices. One such device, a superconducting undulator, offers several distinct performance advantages over current technologies – most notably the generation of high photon flux densities at small undulator period lengths that result in high brightness at high photon energies [1]. To keep the superconducting windings below their current sharing temperature, a thermosiphon system employing two-phase helium near 4.2 K as the working fluid has been developed to convectively cool the undulator cores through three internal channels. The thermosiphon system provides several advantages such as: minimal footprint, lack of mechanical components acting as possible failure mechanisms, robustness with regard to hold-time and quench protection (in contrast to conduction-only designs), and minimal overall consumption of helium compared to bath-cooled alternatives. This experimental investigation centers on mimicking the proposed geometry of the undulator system and determining the mass flow as a function of applied heat load in low quality conditions.

Conventionally, two-phase flow is utilized for its cooling properties because it provides increased heat transfer characteristics compared with single-phase systems. Much work has been done on the two-phase conditions of room temperature fluids for power systems, chemical processing equipment, heat exchangers, boilers and the like, but there is a notable lack of reporting on helium cryogenic systems. Two-phase helium studies have either focused on forced flow systems regulated with a pump or natural circulation results for vertical systems without a

long horizontal length. This report aims to validate a thermodynamic flow model by focusing entirely on low heat load, natural circulation behavior.

The organization of this thesis follows the same progression as the cooling system design process. The introductory section describes the motivation behind the superconducting undulator and its related cooling scheme and displays competitive design alternatives. Chapter 2 focuses on the governing thermodynamic model, flow behavior, and possible instability avenues. It also provides a review of previous work. Chapter 3 details the experimental set-up and procedures. Chapter 4 delivers the test results and compares the behavior to the derived model. Chapter 5 discusses the thermal implications by presenting a steady-state finite element study of the proposed undulator assembly. Chapter 6 finishes with conclusions and recommendations for both the design and future study.

1.2 Review of Undulator Insertion Devices and Subsequent Motivation

The Advanced Photon Source (APS) is one of the premier synchrotron radiation facilities in the world, providing this hemisphere's brightest high energy x-rays for scientific studies [2]. Radiation sourced at the APS has led to advances in combustion processes, new pharmaceuticals, progressive nano-materials and more. Current research groups focus on studies employing spectroscopy (determination of electron binding energies by the photoelectric effect), microscopy, tomography (akin to a 3D x-ray based on focal length), residual stress analysis, crystallography and diffraction in disciplines ranging from polymers/materials to environmental/biological sciences and fundamental physics to soil/geologic investigations.

Traditionally, light sources such as the APS used bending magnets to cause an accelerating electron to produce an electromagnetic pulse. This can be imagined like a radio antenna operating while moving at relativistic speeds, with the subsequent Doppler Shift

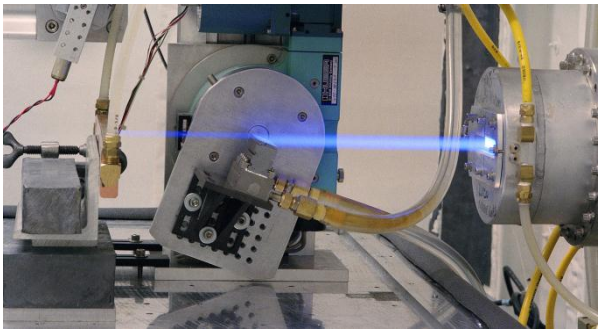

Figure 1.1. Photon beam exiting a beam-line shutter and interacting with a test specimen [4].

narrowing the radiation cone and period length – see FIGURE 1.2. The resulting time contraction at such speeds requires radiation emission according to the Abraham-Lorentz-Dirac (ALD) force and is the result of a charged particle moving through an electromagnetic field. Resultant radiation interacts with a test specimen, exciting its primary resonance and gives scientists the data they need.

While still in use, bending magnets have fairly limited brightness (photon flux) compared to contemporary options and are outperformed by wiggler and undulator insertion devices despite their accessibility and broad energy range. Wiggler-sources behave similarly to bending magnets, but have a notable increase in their resulting spectral brightness. On the other hand, undulators offer several orders of magnitude higher brightness than the counterparts. The radiation produced is coherent, taking advantage of constructive interference in the wave pattern and creating a finely tuned radiation source that requires less data mining, results in higher photon flux densities, and allows for higher photon energies to be explored. FIGURE 1.4 presents a broad comparison of insertion device characteristics and the increased return of undulator magnets. For reference purposes the photon energy along the x-axis can be associated with its wavelength and the brightness can be related to the solid angle such as used in radiation heat transfer studies.

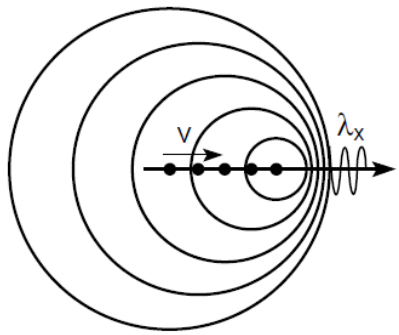

Figure 1.2. Two-dimensional electron movement and pulse formation occurring at relativistic speeds [3].

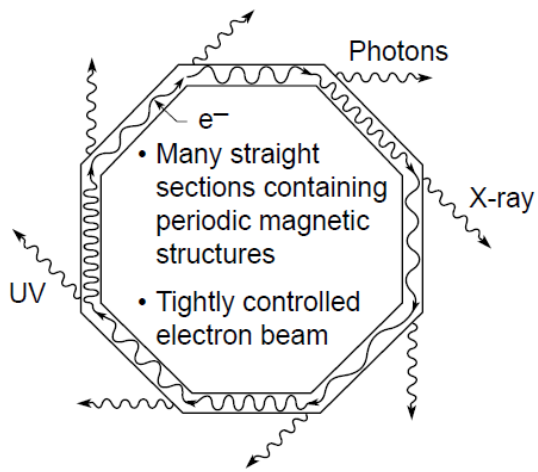

Figure 1.3. Conventional ring layout of a synchrotron radiation facility. Adapted from [3].

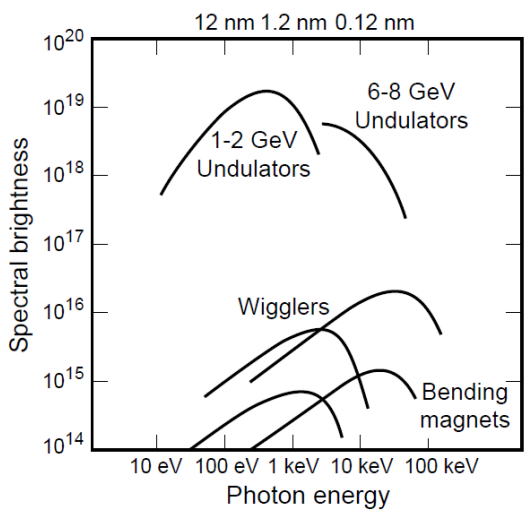

Figure 1.4. Generic insertion device comparison. Adapted from [3].

Increased performance associated with undulators is directly related to being able to operate at shorter wavelengths and the resulting tune-ability, delivering a focused photon spot and allowing for more refined measurements. Superconducting undulators under development take this one step further in that high magnetic fields produce radiation at shorter wavelengths, increasing the brightness produced by the ALD force. FIGURE 1.5 displays the performance of conventional undulator structures used at the APS and demonstrates the large tuning gaps associated with small period coherence at high energies. FIGURE 1.6 shows the increase in performance associated with superconducting devices – namely the broad energy range available and nearly a tenfold increase at times in the brightness produced. For comparison, a 3 cm conventional undulator results in the same magnetic field of 1 T to that of a 1.5 cm superconducting undulator device.

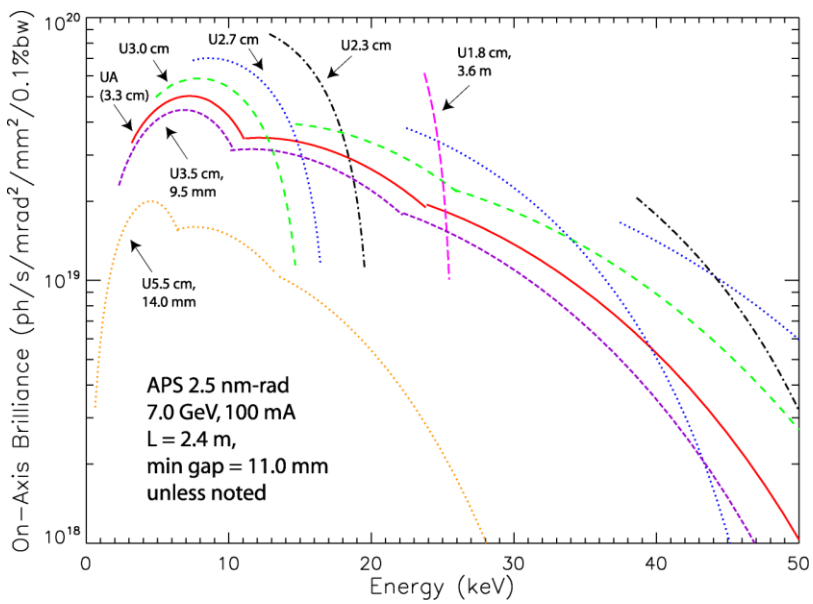

Figure 1.5. Conventional undulator brilliance curve [5].

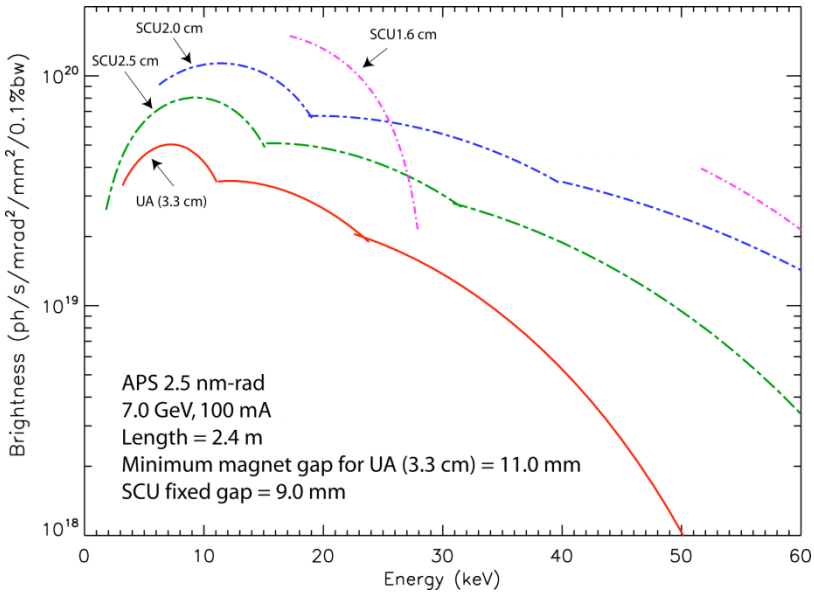

Figure 1.6. Comparison of on-axis brightness between a conventional undulator A device and the superconducting undulator under development [5].

1.3 Competing and Contemporary Designs

Superconducting cooling schemes have been around for quite some time, maintaining high energy physics experiments and magnets below their current sharing temperatures on projects at a number of research laboratories. Even today, large magnetic devices and current leads such as those employed at CERN and Fermi Lab use helium channels and bath-cooled systems as heat transfer mediums for highly sensitive magnetic assemblies. Due to the number and size of such experiments, dedicated cooling systems have been developed and installed, supplying liquid helium from on-site liquefaction facilities and tying systems together through insulated piping networks. Starting in the 1980s, forward-thinking researchers hoped to scale down such structures and implement similar strategies on smaller footprints at light sources. Superconducting wigglers were developed both at the National Synchrotron Light Source (NSLS) and Daresbury Laboratory (DRAL), but the apparatuses still required connection to centralized cryogenic facilities due to re-liquefaction requirements [6-7].

In the decades since, undulator technologies have been refined and, given their performance advantages, efforts have focused on their installation and use. The advent of high capacity, 4 K cryocoolers has re-invigorated several research groups on superconducting devices as a result of their remarkable characteristics, particularly at light sources lacking conventional helium refrigeration infrastructures. Designs have been predicated on closed-system, cryogen-free platforms and are currently under construction and installation. These projects limit helium consumption (an important consideration given its non-renewable nature and ever-increasing price), require fewer structural resources, and take up considerably less space in the light source storage ring.

One prominent research group, working out of the ANKA synchrotron radiation facility at the Karlsruhe Institute of Technology in Germany, has successfully installed a superconducting device and has been characterizing its operation since 2005 with a second device brought online in 2010 [8-10]. The ANKA design is based on a closed-bath structure that completely encapsulates the cores; the cryostat can be seen in FIGURE 1.7. The system is directly related to the magnetic instrumentation projects of COLDDIAG and CASPER [11]. The cooling circuit does not have a designated internal recondenser, which is quite unusual given its stand-alone operation.

Another leading contemporary is the Budker Institute of Nuclear Physics out of Russia, which has collaborated with the APS on this project. The Budker group has a design similar to ANKA's helium baths for wiggler insertion devices, as shown in FIGURE 1.8. The concept has been somewhat successfully installed both at the Diamond Light Source (DLS) and the Canadian Light Source (CLS) [13-14]. This system includes a recondenser, but its effectiveness is suspect as the reported efficiency is less than 30%. The lack of adequate re-liquefaction has caused

issues with pressure rising inside the helium vessel and not seeing a steady-state condition [15]. If stability is not attained, the pressure safety valves can release and the settling temperature can end up above the current sharing temperature. Superconducting devices at the Taiwan Light Source, ELETTRA, and the National Synchrotron Radiation Research Center all are employing a cryostat structure and cooling methodology similar to this design [16-19].

Figure 1.7. Superconducting undulator cryostat in use at ANKA [12].

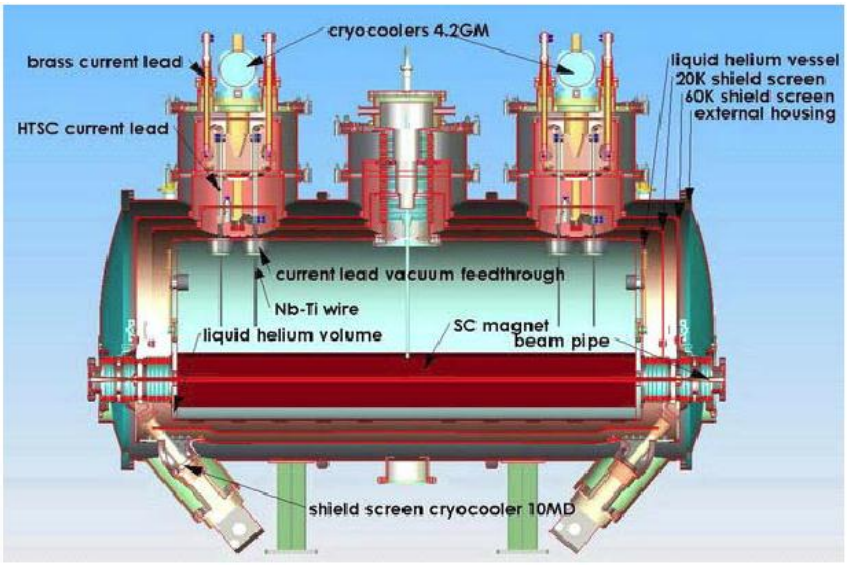

Figure 1.8. Superconducting wiggler cooling system installed at the Diamond Light Source [13].

Similarities in previous design studies can mean one of two things: other designs have been tested and this is the only one found to work for broad operating conditions, or a single design was developed and others have mimicked it in the hopes of being optimized or rugged enough to suit their needs. Currently, studies are underway focusing on conduction-dominated cooling brackets by a principal developer of the technology. Couple this with the fact that closed-loop cryocooler-operated insertion devices are a relatively immature technology, and developmental breakthroughs are still likely to be had.

This thesis is broken up into four main sections. The first (chapter 2) develops the thermosiphon model and anticipated flow behavior in the tests to be performed. Two different horizontal test assemblies were investigated – a single channel assembly consisting of only the venturi and one pipe to verify thermosiphon principles and operation, and a three-channel network to mimic the SCU core geometry. Chapter 3 gives a detailed summary of the experimental set-up and procedure, providing greater details on the test sections and the equipment used. Chapter 4 provides test results that verify the model developed in chapter 2. Chapter 5 then applies the thermosiphon model to the SCU cryostat and details its potential thermal impacts in steady-state operation. Finally, Chapter 6 summarizes the results of the experiment and provides recommendations for future work.

1.4 References

1. *Advanced Photon Source Upgrade Project: Conceptual Design Report*, to be published.
2. *Advanced Photon Source Overview*, Advanced Photon Source Homepage, http://www.aps.anl.gov/About/APS_Overview/, accessed May 11 2011.
3. Atwood, D.T, *Lecture 6: Synchrotron Radiation*, Soft X-rays and Extreme Ultraviolet Radiation, http://ast.coe.berkeley.edu//sxreuv/, accessed March 13 2011.
4. *NSLS Image Library*, National Synchrotron Light Source, http://www.nsls.bnl.gov/about/imagelibrary/, accessed March 20 2011.
5. Moog, E., "Introduction to the Superconducting Undulator Technical Design Review", February 5 2010.
6. Decker, G., "The Superconducting Wiggler at the NSLS: Systems Description and Initial Experience," Brookhaven National Lab, Upton, New York, December 1990.
7. Heron, M.T., Higgins, D.S.G, and Poole, D.E., "A Common Cryogenics System for Two Superconducting Wigglers on the Daresbury SRS," Daresbury Laboratory, Warrington, Wales, 1994.
8. Boffo, C. et al., "Development of the Next Generation Superconductive Undulators for Synchrotron Light Sources," *European Superconductivity News Forum*, Number 7, January 2009.
9. Casalbouli, S. et al., "Beam Heat Load in the ANKA Superconducting Undulator," http://care-hhh.web.cern.ch/CARE-HHH/ECL2/Proceedings/Casalbuoni_ECL2_1.pdf.
10. Bernhard, A. et al., "Performance of the First Superconducting Cold-Bore Undulator in an Electron Storage Ring," *IEEE Transactions on Applied Superconductivity*, Volume 17, Number 2, June 2007.
11. Casalbouli, S. et al., "Progress on the Superconducting Undulator for ANKA and on the Instrumentation for R&D," *AIP Conference Proceedings*, Volume 1234, pp. 33-36, 2010.
12. *Present Activities – ANKA*, Karlsruhe Institute of Technology, http://ankaweb.fzk.de/website.php?page=instrumentation_insert&id=6, accessed May 13, 2011.
13. Krushchev, V.L., et al., "3.5 Tesla 49 Pole Superconducting Wiggler for DLS," *RuPac 2006 Proceedings*, pp. 398-400, 2006.
14. Bekhtenev, E.A., et al., "A Multipole Superconducting Wiggler for Canadian Light Source," *Physics of Particles and Nuclei Letters*, Volume 3, Issue 1, pp. 16-21, December 2006.
15. Ivanyushenkov, Y., Private communication, September 23 2010.
16. Jan, J.C., et al., "Design of Cryogen-Free Mini-Pole Superconducting Undulator," *IEEE Transactions on Applied Superconductivity*, Volume 12, Number 2, pp. 1259-1262, June 2007.
17. Chang, C.H., et al., "In-Achromatic Superconducting Wiggler in Taiwan Light Source: Installation and Test Results," *EPAC Proceedings*, Edinburgh, Scotland, pp. 3613 – 3615, 2006.
18. Zangrando, D., "The ELETTRA 3.5 T Superconducting Wiggler: Assembling, Installation, and Test Results, Superconducting Undulators and Wigglers," ERSF, Grenoble, 2003.

2 Theory of Operation

2.1 Fundamental Thermosiphon Relationships

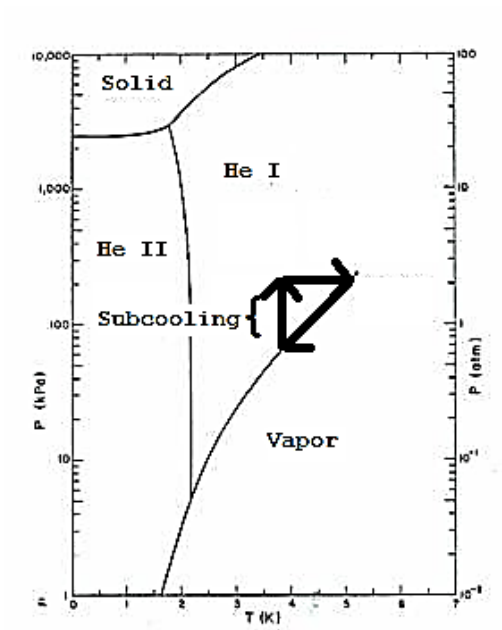

Figure 2.1. Pressure-temperature diagram for helium modified from [12] with exaggerated pressure differences.

Mass flow in a thermosiphon results from a difference in the hydrostatic head between the supply and return legs of a continuous flow loop. The vapor that is generated in the loop from heating the fluid in either the horizontal or vertical return leg results in a lower density in the vertical return leg. In steady state conditions, the hydrostatic pressure difference ΔP_H is balanced by the various system losses

$$\Delta P_H = \Delta P_A + \Delta P_F + \Delta P_{Minor} \tag{2.1}$$

where ΔP_F represents the frictional pressure loss associated with wall interactions, ΔP_A is the acceleration pressure loss required by mass continuity, and ΔP_{Minor} represents the minor losses

associated with bends, inlets, expansion and contraction of the flow. When the horizontal load is the principle heating mechanism, the hydrostatic head equation is represented by

$$\Delta P_H = g * (\rho_{liq} * L_{head} - \rho_{return} * L_{return}) \tag{2.2}$$

where L corresponds to the length of the vertical supply and return legs, respectively, and ρ is the density in the corresponding supply or return legs (the supply side always being single-phase liquid). For the condition in which the heat load is only applied the vertical return leg, equation (2.2) becomes

$$\Delta P_H = g * \rho_{liq} * L_{head} - g * \int_0^{L_{return}} \rho \, dz \tag{2.3}$$

In this study, when heat is applied on the vertical leg, it is localized to a one-inch length, allowing for a simplification of the integrated term to a piecewise algebraic model

$$g * \int_0^{L_{return}} \rho \, dz \approx g * \rho_{liq} * L_{heat} + g * \rho_{return} * (L_{return} - L_{heat}) \tag{2.4}$$

The acceleration pressure drop is governed by

$$\Delta P_A = \chi * (\frac{\dot{m}}{A})^2 * (v_{vap} - v_{liq}) \tag{2.5}$$

with χ representing the quality of the flow, A representing the cross sectional area where the heating is applied, $\dot{m}$ representing the mass flow rate, and v being the specific volume of the

vapor and liquid states, respectively. The frictional losses involve a summation over the various subsections

$$\Delta P_F = \sum f_i * \frac{\dot{m}^2 * L_i}{2 * \rho_{liq} * {A_i}^2 * d_i} \tag{2.6}$$

where *A*, *L*, and *d* are given the appropriate values of the supply, return, and horizontal geometry conditions; ρ is the density of the liquid state; and f_i is the friction factor corresponding to the ith tubing section, corrected with a two-phase multiplier where appropriate.

Traditionally, the friction factor for turbulent flow is obtained through correlations involving the Reynolds number – such as the Blasius solution (equation (2.7)), the Petukhov equation for smooth ducts (equation (2.8)), or the Colebrook equation that accounts for surface roughness, *e*, and is implicit in nature (equation (2.9)) [1-2]. By relying on non-dimensional parameters, these equations are thought to be valid for a variety of working fluids.

$$f_{Blasius} = \frac{0.3164}{Re^{0.25}} \tag{2.7}$$

$$f_{Petukhov} = \frac{1}{(0.79 * \ln(Re) - 1.64)^2} \tag{2.8}$$

$$\frac{2}{\sqrt{f_{Colebrook}}} = 3.48 - 1.7373 * \ln(\frac{2e}{d} + \frac{18.7}{Re * \sqrt{f_{Colebrook}}}) \tag{2.9}$$

Helium, however, does not behave like a typical fluid. Despite a liquid density of ~125 kg/m^3, the liquid viscosity is ~1e-6 kg-m/s, the same order as nitrogen gas at room temperature. Even in "slow flow" cases helium tends to find itself in the turbulent regime. In terms of impact on the friction factor, a hydrodynamics study by Huang found turbulent flow to follow equation (2.10), which is quite different than expected [3]. FIGURE 2.2 presents the differences in the experimentally observed frictions factors.

$$f_{Huang} = \frac{0.21}{Re^{0.25}} \tag{2.10}$$

In regions of developing flow the friction factors are corrected according to

$$f_{Adjusted} = f * (1 + \left(\frac{d}{L}\right)^{0.7}) \tag{2.11}$$

as outlined in [8].

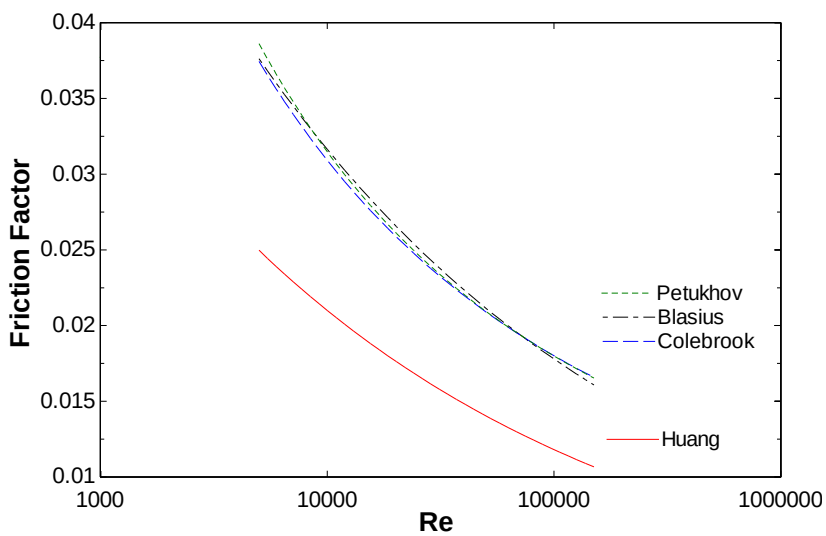

Figure 2.2. Comparison of friction factor correlations for use in the thermodynamic model.

In two-phase flow regimes, the homogenous model is to adjust the friction factor. The homogenous model represents the mixture based on mean fluid properties, including:

1. Equal liquid and vapor velocities
2. Thermodynamic equilibrium among phases

The two phase friction multiplier can be expressed according to

$$\varphi^2 = (1 + \chi * \alpha)(1 + \chi * \beta)^{-n} \tag{2.12}$$

with *n* given an observed value of 0.25 for two-phase turbulent flow and

$$\alpha = \frac{\rho_{liq}}{\rho_{vap}} - 1 \tag{2.13}$$

$$\beta = \frac{\mu_{liq}}{\mu_{vap}} - 1 \tag{2.14}$$

where μ refers to the dynamic viscosity in the liquid and vapor states. Along the horizontal leg for uniform heat application, equation (2.6) then becomes

$$\Delta P_F = f * \frac{\dot{m}^2 * L_{subcooled}}{2 * \rho_{liq} * A^2 * d} + f * \frac{\dot{m}^2}{2 * \rho_{liq} * A^2 * d} * \int_{L_{subcool}}^{L} \varphi(x) dx \tag{2.15}$$

The homogenous model has been confirmed to work quite well for both bubbly and mist flow patterns (see section 2.2 for explanation) and with some varying success for stratified and annular patterns. Separated flow correction methods, such as the Lockhart-Martinelli correlation, have been widely used at ambient conditions for a number of fluids with the highest success rate involving water/steam systems in annular or stratified flow situations. Several helium studies, notably by Khalil and Huang separately, have shown such corrections to be invalid due to the vastly different property relationships [3-7].

Finally, minor losses associated with secondary flow patterns are created whenever a fluid turns, expands or contracts. These losses can dominate thermosiphon performance, especially if the head length is short. Sometimes expressed in a form similar to frictional losses, the minor losses are

$$\Delta P_{Minor} = \sum \mathrm{K_i} * \frac{\dot{m}^2}{2 * \rho_i * {A_i}^2} \tag{2.16}$$

with K_i representing an experimentally determined coefficient for a particular geometry and flow condition. As most loss coefficients are listed according to observation in water/steam systems or simply listed in ill-documented tables, care was taken to find correlations directly or indirectly as a function of the Reynolds number [2-4].

For submerged inlet losses associated with sharp edges (90^0), K is given a value of 0.5 based on convergence, as seen in FIGURE 2.3. Submerged exits converge similarly to a K value of 1.0.

Sudden expansion and contraction losses follow equations (2.17) and (2.18), respectively. FIGURE 2.4 displays their impact as a function of geometry. Notice the cartoons of FIGURE

2.4 and how they display the losses as a result of turbulent eddies and the vena contracta of the flow.

$$K_{SE} = (1 - \frac{d_{small}^2}{d_{large}^2}) \tag{2.17}$$

$$K_{SC} = 0.42 * (1 - \frac{d_{small}^2}{d_{large}^2}) \tag{2.18}$$

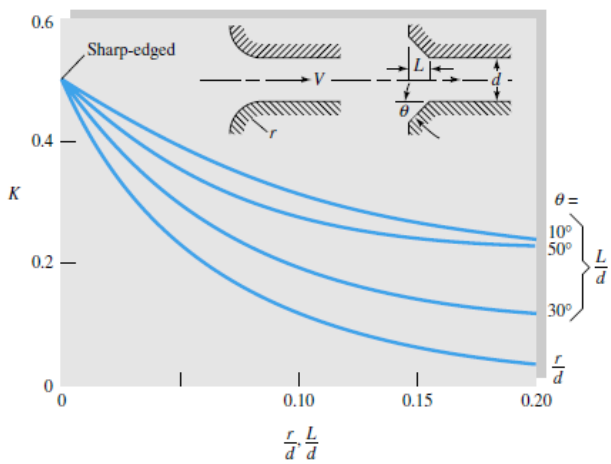

Figure 2.3. Inlet loss coefficient as a function of geometry. Taken from [9].

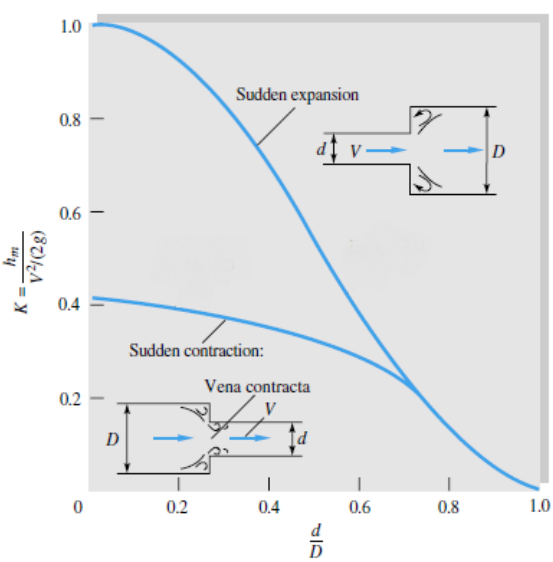

Figure 2.4. Minor loss coefficient for sudden expansion and contraction of in-flow elements. Taken from [9].

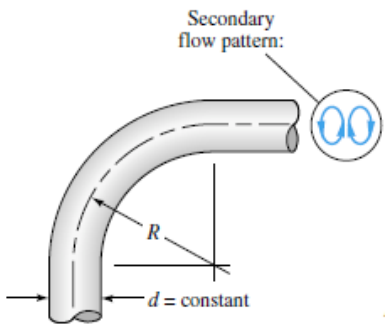

Figure 2.5. Secondary flow pattern for a 90^0 tube bend. Adapted from [9].

Four curved bends appear in the horizontal flow network: two at the inlet and two at the outlet. These bends follow equation (2.19) and are a result of the secondary flow pattern exhibited in FIGURE 2.5.

$$K_{bend} = 0.388 * \alpha * \left(\frac{R_{bend}}{d}\right)^{0.84} * Re^{-0.17} \tag{2.19 a}$$

with

$$\alpha = 0.95 + 4.42 * \left(\frac{R_{bend}}{d}\right)^{-1.96} \tag{2.19 b}$$

Another network loss that will be relevant to this study is associated with two flanged-tee adapters at the inlet and outlet of the horizontal test sections. These losses are characterized by equation (2.20) and are a function of the turbulent friction factor, which in turn is dependent on the Reynolds number (equation (2.10)) [10].

$$K_{tee} = 60 * f_T \tag{2.20}$$

Two different models for losses associated with a Venturi flow element are compared below: one developed by combining separate loss coefficients for converging then diverging sections (Venturi (a)), and the other directly from a published chart for Venturis (Venturi (b)). The first method uses equations derived by the Crane Corporation [10]. The converging section obeys (2.21) and the diverging section is governed by (2.22)

$$K_{con} = 0.5 * \left(1 - \left(\frac{d_{throat}}{d_{inlet}}\right)^2 * \sqrt{\sin\left(\frac{\alpha_1}{2}\right)}\right) / \left(\frac{d_{throat}}{d_{inlet}}\right)^4 \tag{2.21}$$

$$K_{div} = 2.6 * \left(1 - \left(\frac{d_{throat}}{d_{inlet}}\right)^2 * \sin\left(\frac{\alpha_2}{2}\right)\right) / \left(\frac{d_{throat}}{d_{inlet}}\right)^4 \tag{2.22}$$

where α_1 is the angle of convergence and α_2 is the angle of divergence. The second method uses tables/relationships devised in [11] and charts shown in [9] that, adjusted for a larger than normal contraction angle, result in a K of ~0.22. This approach also assigns the area term in equation (2.16) to that of the throat instead of the piping. As liquid helium is generally not investigated in minor loss characerization studies, it is unknown which is more accurate and both methods are included for comparison.

FIGURE 2.6 schematically displays the geometric configuration of the thermosiphon being addressed in this study. The analysis of the system begins with an inspection of the thermodynamic states at various locations along the flow path. It is assumed that in the reservoir saturation conditions with an operating temperature of 4.22 K and a pressure of one atmosphere exist. The pressure rise from the hydrostatic head results in a subcooled state at the bottom of the vertical supply tube – represented in FIGURE 2.6 and exaggerated in FIGURE 2.1. If a heat

load is applied along the horizontal leg, it is possible for the fluid to reach saturation. The heating rate associated with the change from the subcooled state to a saturated state is calculated from

$$\dot{Q}_{subcool} = \dot{m} * (h_{sat} - h_{inlet}) \tag{2.23}$$

The saturation state, and the enthalpy there (h_{sat}), is determined by two properties – the pressure and the quality. The pressure at the saturation state is obtained from the pressure at the subcooled state and the pressure drop along the horizontal leg – that in turn being determined by the liquid mass flow rate. The enthalpy at the inlet to the horizontal leg, h_{inlet}, is determined by the pressure at the inlet of the horizontal test section. The mass flow rate of the vapor at the outlet of the horizontal section, and the associated flow quality, are respectively determined by

$$\dot{m}_{vap} = (\dot{Q} - \dot{Q}_{subcool})/(h_{vap} - h_{liq}) \tag{2.24}$$

$$\chi = \dot{m}_{vap}/\dot{m} \tag{2.25}$$

where h_{vap} and h_{liq} are the respective enthalpies of saturated vapor and liquid in the horizontal section, and $\dot{Q}$ is the total heat load applied.

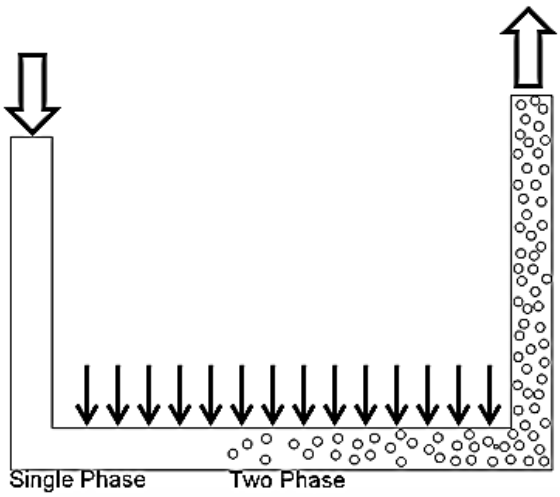

Figure 2.6. Cartoon representing thermosiphon operation and the impact of subcooling.

Combining the previous equations enables the mass flow to be characterized as a function of the applied heat load, subcooled height, and minor losses. FIGURE 2.7 displays the mass flow rate for a subcooled height of 0.31 m, a channel cross sectional area of 195 mm^2, and the inclusion of various loss terms. FIGURE 2.10 displays the same information for the three-channel test having an equivalent horizontal length of 1.13 m and the horizontal mass flow rate being one third the total flow rate. The "No Losses" line represents the theoretical limit absent of minor losses. The "Including Minor Losses" line shows the flow with the inclusion of minor losses for the test geometry but omits those associated with the venturi. "Venturi losses (a)" adds the minor loss associated with the venturi to the model, using the converging and diverging method to determine the loss coefficient. "Venturi losses (b)" uses the table model. The quality at the exit of the same three-channel horizontal test section of FIGURE 2.10 is shown in FIGURE 2.9. Due to the low quality associated with the low heat loads, the flow rate never reaches a stagnant value that would be seen when the vapor fraction pressure losses balance the hydrostatic pressure drop. This balance is generally observed at qualities above 0.2 – more than a factor of 4 greater than shown in FIGURE 2.9. FIGURE 2.8 indicates the impact of the

hydrostatic head height on the flow rate in a thermosiphon. In the case of ideal flow (no losses), an optimal head height is observed, above which the mass flow rate decreases monotonically. This interesting feature results from the subcooled condition at the horizontal tube inlet. In short, a higher head causing larger subcooling requires a larger portion of the horizontally distributed heat to bring the fluid back to saturation conditions. Any heat deposited along the remaining horizontal length produces vapor, increasing the exit quality. As a result, larger subcooling results in smaller exit qualities, decreasing the driving force and reducing mass flow rates. The addition of minor losses imposes a greater flow resistance than in the ideal case, reducing the mass flow for the same driving force. However, while the mass flow rates are reduced the optimal head height is increased and broadened.

Variable	Dimension
d, d_{inlet}, d_{small}	15.75 mm
d_{large}	47.24 mm
L_{head}, L_{return}	0.31 m
L_{supply}	0.1 m
$L_{horizontal}$ *(single channel)*	0.44 m
$L_{horizontal}$ *(three-channel equivalent)*	1.13 m
L_{in}, L_{out} *(associated with inlet/outlet piping)*	0.29 m
d_{throat}	0.29 m
α_1	7.62 mm
α_2	18°
R_{bend}	0.076 m

Table 2.1. Dimensions of test assembly used in modeling analysis.

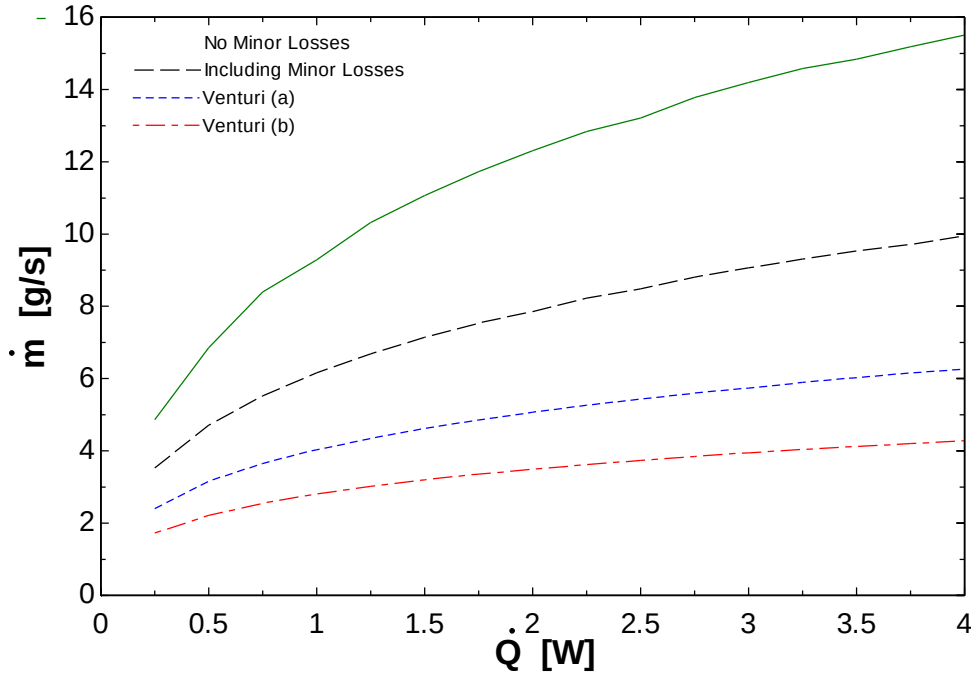

Figure 2.7. Expected flow rates with various loss terms included as a function of horizontal heat load for the single channel test.

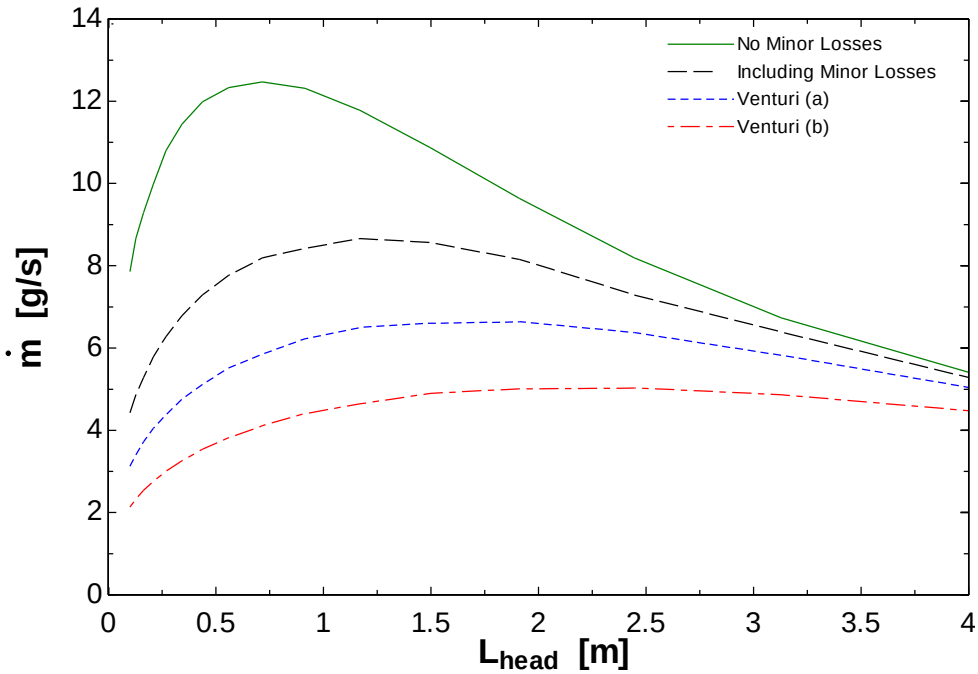

Figure 2.8. Expected flow rates for a 1.5 W heat load to the single channel assembly as a function of head height.

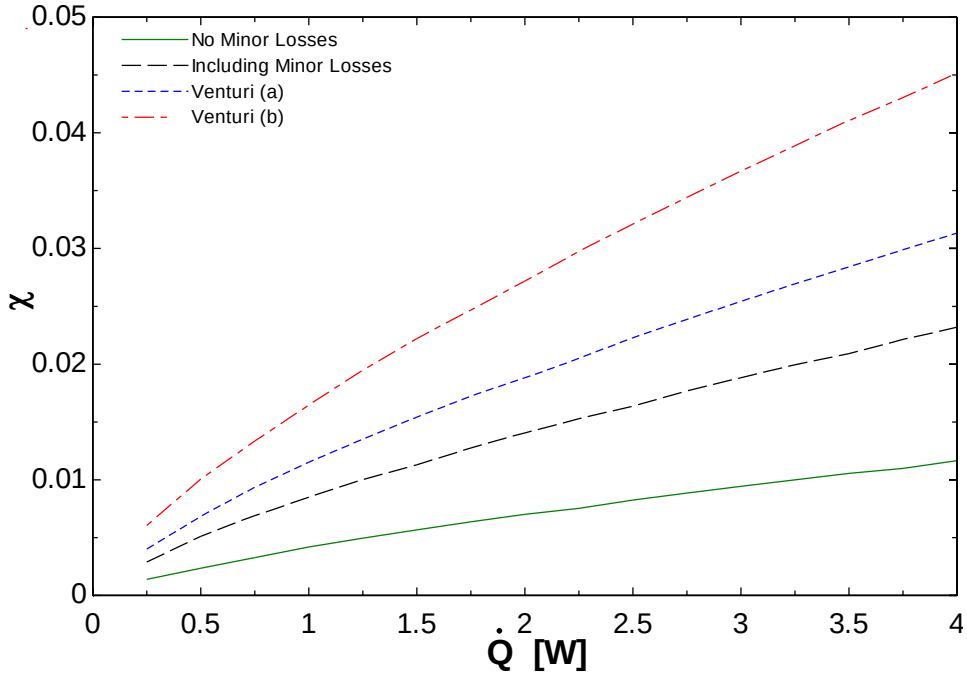

Figure 2.9. Expected vapor quality under different model conditions as a function of horizontal heat load for the three-channel test.

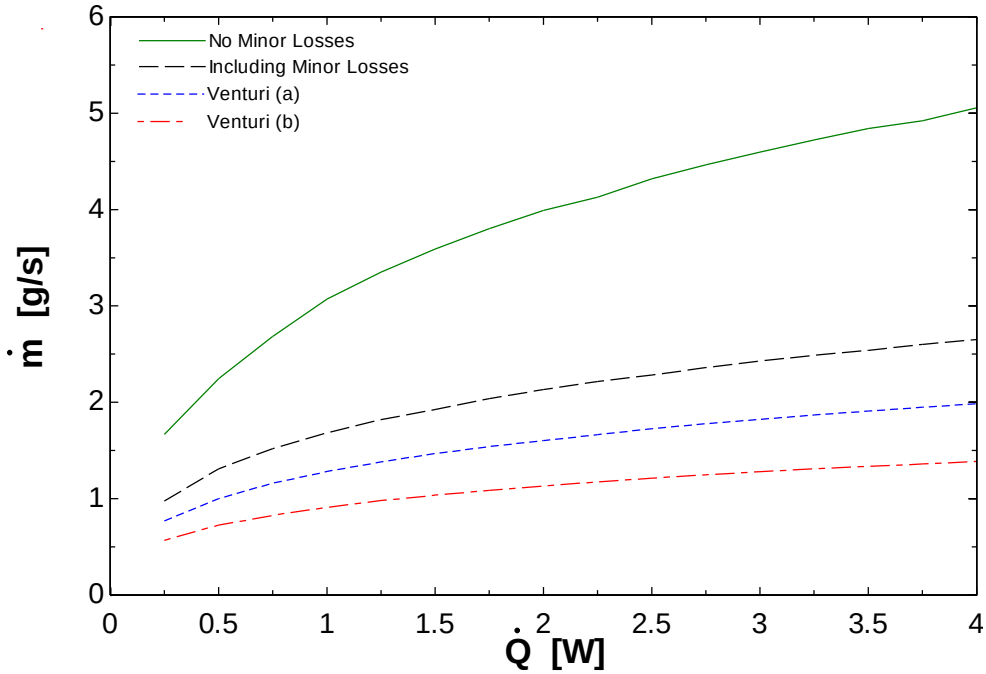

Figure 2.10. Expected flow rates inside the three-channels for various loss conditions as a function of horizontal heat load in three-channel test.

2.2 Two-Phase Flow Characteristics

The two phase flow resulting from vapor formation in the flow channels can take on a variety of patterns, or flow regimes, and each of the regimes have distinct heat transfer characteristics. Because the thermosiphon's primary purpose is to provide cooling for the superconducting undulator under development at ANL, it is important to know which flow pattern will be present as it will impact the heat transfer coefficient in the core. Normally, a two-phase fluid will exhibit either homogenous (froth, dispersed, bubbly) or non-homogenous (stratified, plug/slug, wavy, annular) patterns shown in FIGURE 2.11.

Theilacker and Rode previously found that the flow regimes for two-phase helium do not follow those shown above as defined in the traditional Baker diagram, seen in FIGURE 2.12 [12]. From their measurements and observations, further confirmed by data from Mamedov, et al, they concluded that it is extremely difficult to get out of stratified flow [13].

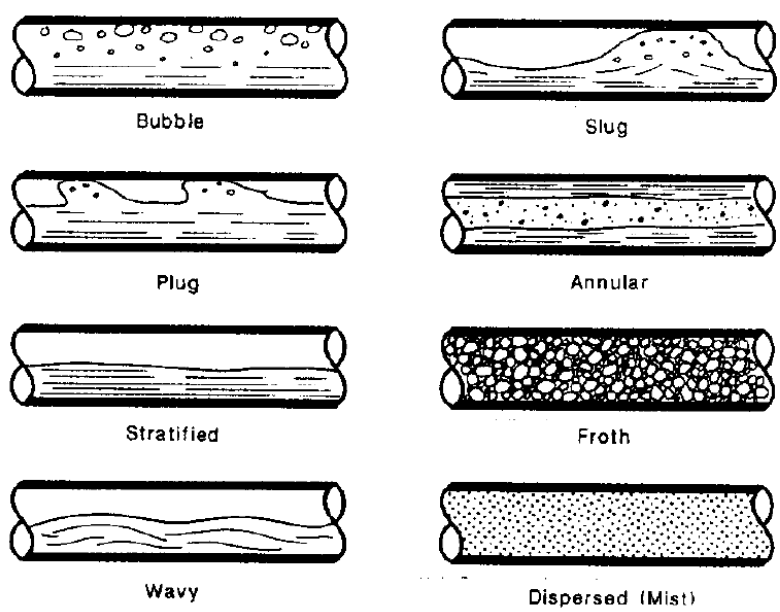

Figure 2.11. Traditional two-phase flow regimes. Taken from [12].

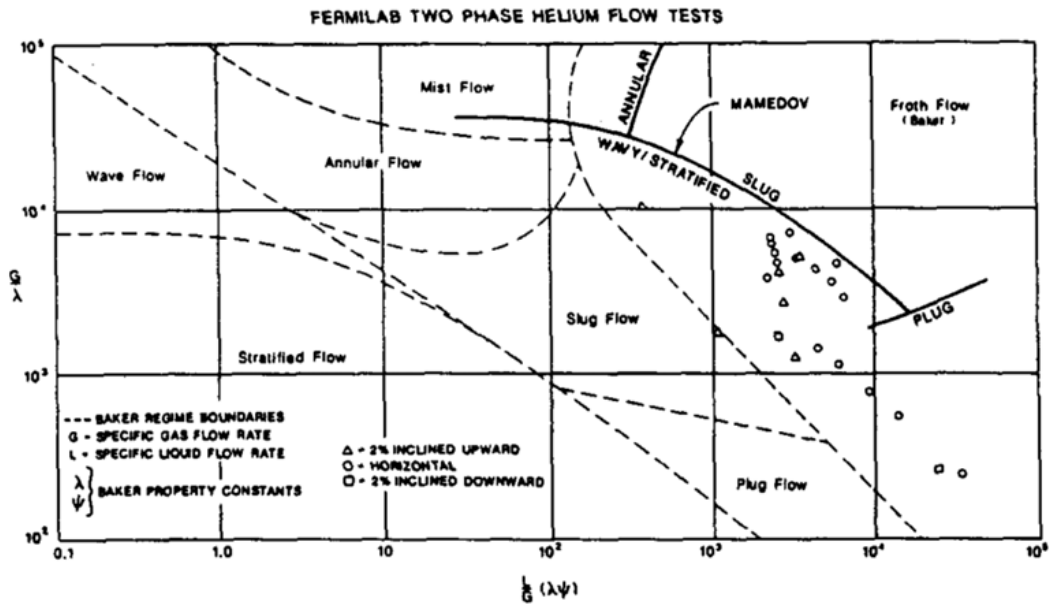

Figure 2.12. Baker diagram for two-phase helium flow [12].

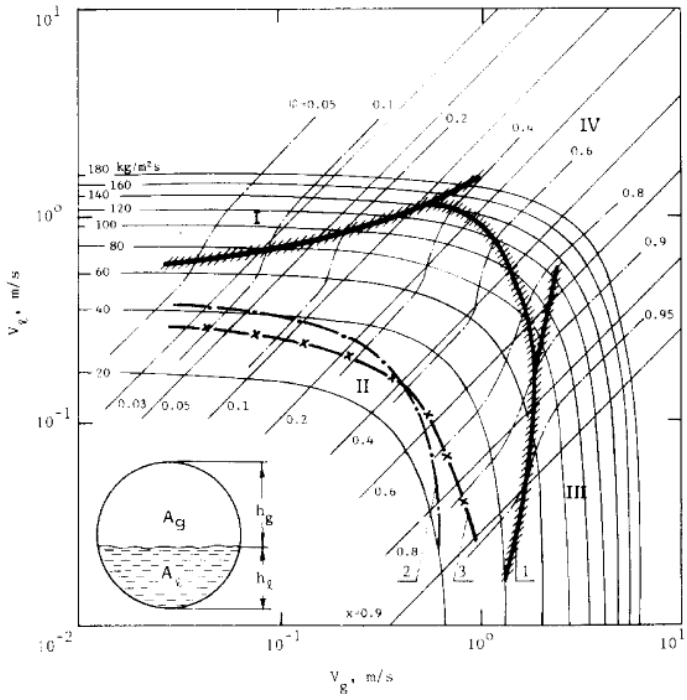

Figure 2.13. Filippov flow map example for helium – I. bubbly, II. stratified, III. dispersed, IV. mist [15].

Filippov furthered the commentary by creating and verifying a new mapping technique for use with two-phase helium, as shown in FIGURE 2.13 [14, 15]. The refined method accounts for the fact that helium's fluid properties – especially density – are similar on both sides

of the vapor dome. The similarity is in stark contrast to a conventionally mapped fluid like water (the ratio of liquid to vapor density at atmospheric pressure for helium is ~7; the density ratio for water is ~1000). On the map, the vertical axis is a liquid pseudo-velocity and the horizontal is a vapor pseudo-velocity. The lines that go from horizontal to vertical represent lines of constant mass flux, and the lines on the diagonal are lines of constant quality.

As shown in FIGURE 2.9, the anticipated vapor quality of this experiment is extremely low. Based on the Filippov map, either stratified or bubbly flow patterns are possible. To determine the transition line between these two regions, equations (2.26-2.38) are iteratively solved with Filippov's method, borrowing the convention from [16, 17] and using pseudo-velocity axes. First, one calculates the void fraction from the quality, using the expression

$$\varphi_f = \frac{\chi * \rho_{liq}}{(1-\chi) * \rho_{vap} + \chi * \rho_{liq}} \tag{2.26}$$

The areas of the vapor and liquid are then determined by

$$A_{vap} = A_{tot} * \varphi_f \tag{2.27}$$

$$A_{liq} = A_{tot} - A_{vap} \tag{2.28}$$

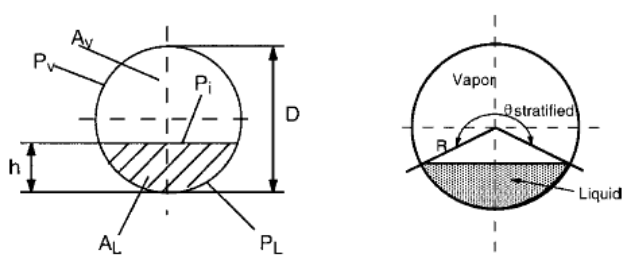

Figure 2.14. Graphic of equilibrium for stratified flow [17].

Three equations are iteratively solved to calculate the liquid-vapor interface length, p_i

$$\theta = \sin^{-1}\left(\frac{h}{R} - 1\right) \tag{2.29}$$

$$p_i = d * \cos(\theta) \tag{2.30}$$

$$A_{liq} = \pi * \frac{R^2}{2} + \theta * R^2 + p_i * \frac{h - R}{2} \tag{2.31}$$

with h representing the liquid height and θ the angle above the diameter to the liquid level. The liquid and vapor perimeters are calculated by

$$p_{liq} = R * (\pi + 2 * \theta) \tag{2.32}$$

$$p_{vap} = \pi * d - p_{liq} + p_i \tag{2.33}$$

The transition line between bubbly and stratified flow is governed by the boundary condition defined by equation (2.34), where g is the acceleration due to gravity. The equation is solved for the liquid velocity, U, which is then converted to a corresponding superficial liquid velocity, v,

$$U_{liq}^2 = \frac{4 * A_{vap}}{p_i} * \frac{g}{f_{liq}} * \left(1 - \frac{\rho_{vap}}{\rho_{liq}}\right) \tag{2.34}$$

$$v_{liq} = U_{liq} * \left(1 - \varphi_f\right) \tag{2.35}$$

Note that the friction factor in equation (2.34) is only with respect to the liquid flow in the channel and uses the Blasius definition, unlike the thermosiphon model presented earlier. The liquid velocity allows one to calculate the mass flux, G, according to

$$v_{liq} = G * \frac{1-\chi}{\rho_{liq}} \tag{2.36}$$

The superficial vapor velocity is then evaluated by

$$v_{vap} = G * \frac{\chi}{\rho_{vap}} \tag{2.37}$$

To determine the boundary condition for entrainment, equation (2.34) becomes

$$1.4 \leq \frac{\left(\left(\rho_{liq} - \rho_{vap}\right) * f_{liq} * U_{liq}^2\right)}{\left(\rho_{liq} * g * \sigma\right)^{0.5}} \tag{2.38}$$

with σ defined as helium's surface tension, as outlined in [18]. The resulting maps for the horizontal loads of the single channel and three-channel tests (inside the channels) are shown in FIGURES 2.15 and 2.16. The low quality and large bore sizes of the experiment create stratified flow conditions regardless of heat load, confirming Theilacker's, Rode's, and Mamedov's observations.

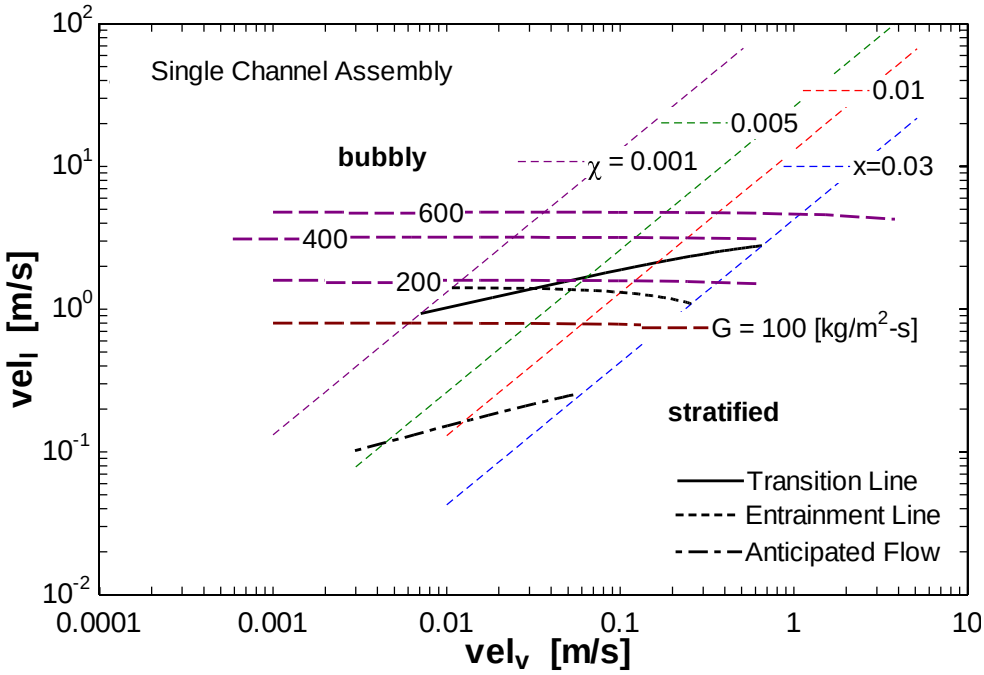

Figure 2.15. Anticipated flow pattern for single channel test.

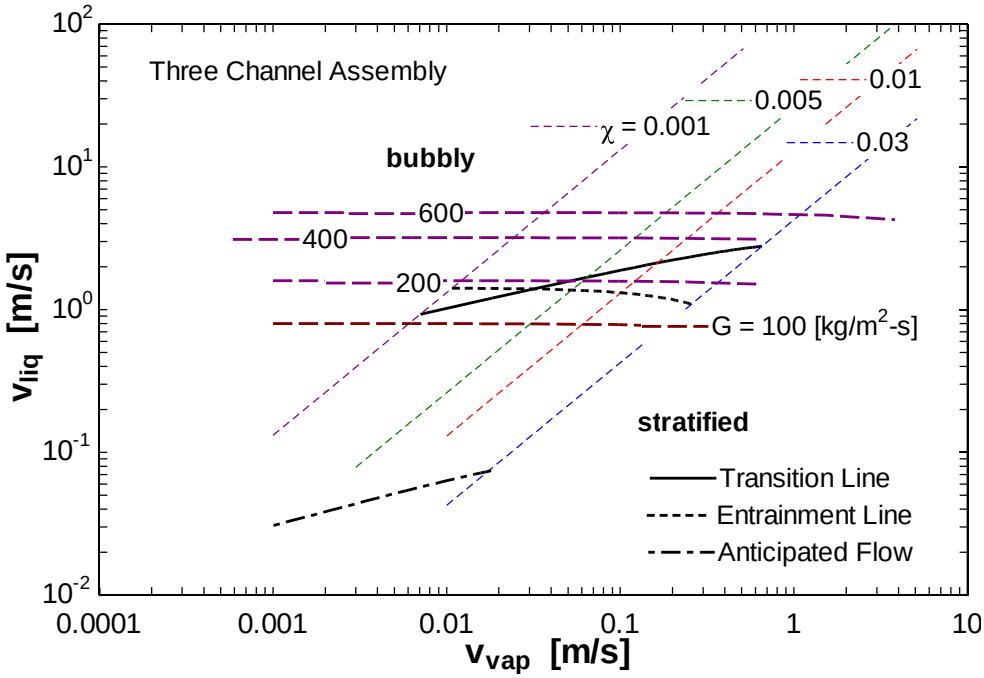

Figure 2.16. Anticipated flow pattern for three-channel test.

2.3 Heat Transfer Characteristics

Predicting the heat transfer coefficient as a function of heat load inside the superconducting undulator magnets is a critical design consideration. The principal operating characteristic of a thermosiphon is that it acts as a passive heat transfer mechanism by natural convection. With helium as the working fluid, the induced circulation proves exceptionally important given liquid helium's thermal conductivity of just ~0.02 W/m-K. If helium were allowed to stagnate in the channels, any heat applied via radiation or conduction would find its preferred path through that of the core structure, creating the possibility for hot spots on the metal's surface (see Chapter 5 for further discussion). Furthermore, stratified conditions also provide poor heat transfer into the vapor regions at the top of horizontal flow sections.

Heat transfer coefficients for single-phase, turbulent internal flow are typically obtained from the Dittus-Boelter equation

$$h_{DB} = 0.023 * Re^{0.8} * \mathrm{Pr}^{0.4} * \frac{d}{k} \tag{2.39}$$

where *h* is the heat transfer coefficient, *Re* is the Reynolds number, *Pr* is the Prandtl number, and *k* is the thermal conductivity of the fluid. The Dittus-Boelter equation has three requirements in application – the Reynolds number must be greater than 10,000, the Prandtl number must be between 0.7 and 160, and the length-to-diameter ratio must be greater than 10. Helium's Prandtl number is 0.867, the anticipated Reynolds number is never less than 17,000, and the experiment *L/d* ratio is 17.

For vertical thermosiphons, the Johannes correlation provides a well-documented method for two-phase helium flow

$$h_{J-TP} = h_{DB} * A * X_{tt}^{-n} \tag{2.40}$$

where the subscript *J-TP* refers to Johannes two-phase, *A* and *n* are best fit coefficients, 5.4 and 0.385 respectively, and X_{tt} represents the Lockhart-Martinelli parameter

$$X_{tt} = \left(\frac{1-\chi}{\chi}\right)^{0.9} * \left(\frac{\rho_{vap}}{\rho_{liq}}\right)^{0.5} * \left(\frac{\mu_{liq}}{\mu_{vap}}\right)^{0.1} \tag{2.41}$$

where χ is the quality, ρ is the density, and μ is the dynamic viscosity. Based on observations in [19], vertically oriented helium thermosiphons tend to have heat transfer characteristics twice as effective as anticipated by this relationship. The enhancement is attributed to the fact that flow is developing, both thermally and hydrodynamically, along the entire length of the thermosiphon; forced convection theories underestimate the effects of the friction factor and the heat transfer coefficient [20]. However, for horizontal stratified flow with exceptionally low quality, the single phase Dittus-Boelter correlation, adjusted to take into account only the liquid's contribution provides a conservative calculation of the heat transfer coefficient

$$h = h_{DB} * (1-\chi)^{0.8} \tag{2.42}$$

FIGURES 2.17 and 2.18 present the anticipated heat transfer coefficients for the single and three-channel assemblies of this test as a function of heat load for given minor loss impacts.

It should be noted there is a surprising lack of two-phase heat transfer correlations available for horizontal configurations using liquid helium above the lambda point. This is likely

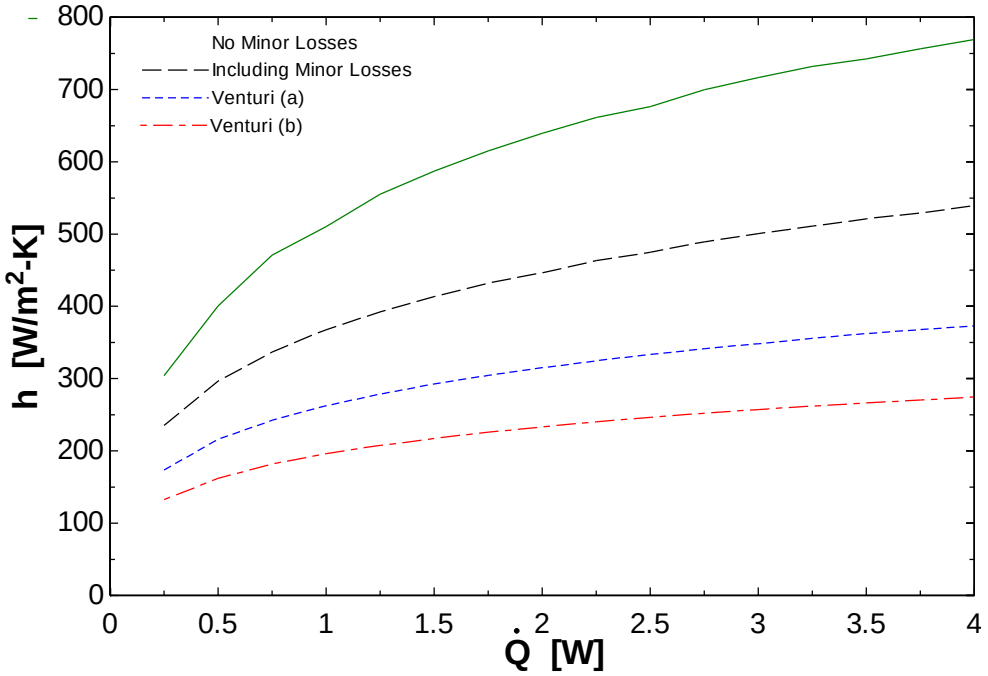

Figure 2.17. Anticipated heat transfer coefficient for single channel assembly.

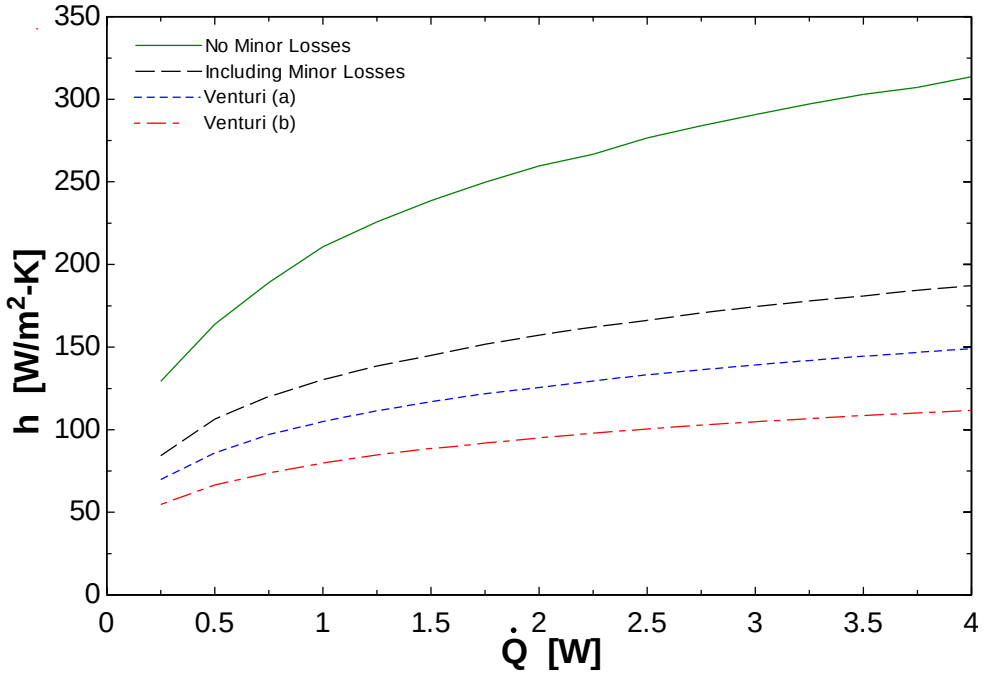

Figure 2.18. Anticipated heat transfer coefficient for three-channel assembly inside the channels.

due to the difficulties void fraction measurements in liquid helium as mentioned earlier, but presents a future avenue for study.

2.4 Instability Avenues

Two-phase cryogenic experiments are often plagued by a variety of instabilities that can greatly affect the flow behavior. As thermosiphons operate by completely passive means, they tend to display oscillatory instabilities and not excursion types that are caused by mechanical components creating multiple equilibrium conditions. A more thorough discussion can be found in [21], but a brief primer will be given here to describe the possible instabilities that may result from the heat being applied to both the horizontal and vertical legs.

2.4.1 Horizontal Instabilities

The most common instability in horizontal flow systems is the density wave. Density waves occur in slug or plug flows when an uncharacteristically large section of liquid passes through a restriction, decelerating the flow. The deceleration causes the liquid inside the channels to have more time in contact with the heat source, resulting in more vapor formation. When the vapor segment reaches the restriction, the flow accelerates and a section of fluid in the channel is temporarily left with a decrease in vapor content. When this liquid section flows through the restriction, the cycle starts over.

Although infrequent, thermal excursion coupled oscillations can present themselves if sufficiently high heat fluxes are encountered to initiate nucleate boiling. In such a case, the heat flux into the liquid of the channel is a function of the film boiling layer thickness as well as the applied heat load. If a perturbation occurs, the flow can accelerate. The acceleration decreases the vapor boundary layer, increasing the heat flux. The increase in heat flux causes the boundary layer to grow, decreasing the heat flux. Given the right conditions, oscillations are sustained.

2.4.2 Vertical Instabilities

Vertical instabilities most often come in two varieties – geyser-like and density-driven. Density waves were discussed earlier and occur from upstream restrictions. In the vertical leg of a thermosiphon, the instabilities tend to require a large density change. A flow perturbation or restriction that changes inside of the vertical tube causes the inlet flow rate to vary. The oscillation is gravity dominated.

Geyser instabilities, on the other hand, can occur in systems of low heat flux and low vapor formation. Much as their name implies, superheating (not boiling) arises from a lack of nucleation sites along the smooth vertical piping. If a flow disturbance occurs in the network, a rapid boil begins. Quick vapor formation reduces the pressure head at the boiling site, increasing the superheat and associate pressure, forcing more liquid from the system. Eventually an equilibrium condition is met, vapor production ceases, and liquid re-enters the system from the reservoir. The process is analogous to that in naturally occurring geysers – hence the name. A closely related phenomenon to geysering is the U-tube oscillation observed in manometer-type experiments, which is just a periodic form of geysering. FIGURE 2.19 offers a visual representation of geysering as it is the most commonly encountered phenomenon in thermosiphon experiments.

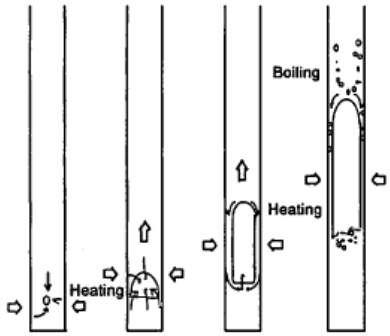

Figure 2.19. Visual representation of geysering. Taken from [22].

2.5 Thermoacoustic Oscillations

A final instability, the thermoacoustic oscillation, although not related to two-phase flow, deserves its own discussion due to its potential impact on closed cryogenic containers, such as the helium reservoir for the superconducting undulator. This analysis focuses on the SCU cryostat instead of the test assembly because the experimental test rig outlined in chapter 3 because it is operated as an open system due to lack of a recondenser.

First observed by Lord Rayleigh in 1887 [32] and then investigated by Taconis in 1949 (and subsequently known as Taconis oscillations) [33], thermoacoustic oscillations (TAOs) have both fascinated and plagued those working on cryogenic experiments. TAOs occur when a tube of stagnant gas is capped off at its warm end while the cold end is still open. They are the mechanism by which pulse tube refrigerators and certain helium level indicators operate. However, since they are also able to increase the heat load on cryogenic systems by several orders of magnitude, it is crucial to understand what conditions give rise to the oscillations. The long tubing and low heat load tolerances associated with the superconducting undulator being developed at Argonne National Lab requires careful consideration of the size of the tubes connecting the liquid helium reservoir to the room temperature environment.

The often cited reliable theory for thermoacoustic oscillations was first proposed by Rott in 1969 [23] and subsequently refined numerically in 1973 [24] and 1975 [25]. To predict when thermoacoustic oscillations would occur, a long tube approximation based on a second order Stokes boundary layer was used. Stability maps characterized by the ratio of the tube radius to the boundary layer thickness, the hot-to-cold temperature and length ratios were then generated. The numerical model developed by Rott is based on a discontinuous temperature distribution; as

long as the temperature profile of the system being investigated has a certain steepness, S, the maps are valid. ($S = \infty$ for the perfectly discontinuous case.)

$$S = \frac{2L_c}{T_H - T_C}\frac{dT}{dx}_{x=L_c} \tag{2.43}$$

In the above equation, T_H represents the mean temperature of the warm tube section, T_C represents the mean temperature of the cold open-ended tube, and L_c represents the cold length of the tube. Any steepness larger than 10 generally has been found to follow the discontinuous model. The anticipated value of S for the helium fill channels out of the SCU cryostat is on the order of 1.5, making the prediction less certain. That said, the anticipated temperature profile (FIGURE 2.22) is somewhat gradual, creating poor conditions for TAOs – there is a reduced temperature disjoint to promote the shifting of gas between cold and hot regions, mitigating spontaneous oscillations.

The stability boundary differentiating the region where TAOs can occur from those where they cannot is made up of three sections: a left asymptote representative of capillary-like tubing, a right asymptote representing larger diameter piping, and a horn region bridging the two asymptotes. Subscripts of C and H refer to the respective cold and warm end of the pipe being examined. To develop the map, several fluid properties are needed (notation via Rott):

μ_c viscosity of vapor at cold end

ρ_c density of vapor at cold end

c_c vapor speed of sound of at cold end

γ specific heat ratio (for helium, γ=5/3)

β exponent of T in the power law dependence of viscosity (for helium, β = .647)

Pr Prandtl number (for gaseous helium, σ = 2/3)

D a numerical value used in defining the right asymptote

Two coefficients, *c* and *d* (Kirchoff's and Kramer's constants of a gas, respectively), can be derived using some of these properties

$$c = \frac{1}{2}\left(1 + \frac{\gamma - 1}{\sqrt{Pr}}\right) \tag{2.44}$$

$$d = \frac{1}{1+\beta}\frac{2}{Pr + \sqrt{Pr}} - \frac{\gamma - 1}{\sqrt{Pr}} \tag{2.45}$$

For plotting purposes, two non-dimensional quantities are introduced: *Y* and α. *Y* is the ratio of the radius of the tube to the Stokes boundary layer and α is the ratio of the hot to cold mean temperatures.

$$Y = R * \left(\frac{\rho_c c_c}{L_c \mu_c}\right)^{1/2} \tag{2.46}$$

$$\alpha = \frac{T_H}{T_C} \tag{2.47}$$

Before mapping for TAOs, ξ, the ratio of the hot length of pipe to the cold length (the length exposed to the cold reservoir and up to the transition point), must be defined

$$\xi = (L - L_c)/L_c \tag{2.48}$$

To determine the asymptotes, a value for the parameter $\lambda_{c,linear}$ based on a linear approximation is first calculated

$$\xi = \frac{\cot(\lambda_{c,linear})}{\lambda_{c,linear}} \tag{2.49}$$

For $\xi < 1$, the right asymptote is defined by assigning either values of α or Y_c and solving

$$Y_C = 2D\ (1 + \xi^{-1} + {\lambda_{c,linear}}^2 \xi)^{-1}\ \alpha^{1+\beta} \tag{2.50}$$

For $\xi > 1$, the right asymptote is defined similarly by

$$Y_C = \frac{2D}{1 + \xi^{-1} + {\lambda_{c,linear}}^2 \xi} \frac{\alpha^{\frac{3+\beta}{2}}}{\alpha^{\frac{1-\beta}{2}} + X} \tag{2.51a}$$

where

$$X = \frac{2}{3} {\lambda_c}^2\ \xi^2 (1 + \xi^{-1} + {\lambda_c}^2 \xi)^{-1} \tag{2.51b}$$

For $\xi < 1$, the left asymptote is defined by

$$\alpha = \ .228\ \xi\ {Y_C}^{2.214} \tag{2.52}$$

and for $\xi > 1$

$$\alpha = \ .0264\ \xi\ {Y_C}^{2.429} \tag{2.53}$$

ε	G_R	G_I
0	1	0
0.2	0.9978	0.0291
0.4	0.985	0.1078
0.6	0.9397	0.2441
0.8	0.7977	0.3734
1	0.6268	0.4158
1.2	0.4901	0.4015
1.4	0.3923	0.3678
1.6	0.3228	0.3314
1.8	0.2722	0.2979
2	0.2348	0.2686
2.5	0.1719	0.212
3	0.1346	0.1728
3.5	0.11	0.1447
4	0.0926	0.1238

Table 2.2. The G-function for helium.

In the horn region, values of Y_H (the ratio of the tube radius to the Stokes boundary layer on the warm end of the tube) are assigned. These values determine the value of ε

$$\frac{2}{Y_H} = \varepsilon \tag{2.54}$$

ε is then used to interpolate the G-function (developed in Rott's 1969 paper), allowing for λ_c to be calculated

$$\xi(G_R + G_I) = \frac{\cot(\lambda_c)}{\lambda_c} \tag{2.55}$$

Another variable, *C*, is then able to be determined

$$C = \frac{\cot(\lambda_c)}{\lambda_c} \tag{2.56}$$

Y_C is then

$$Y_C = \frac{\sqrt{2}}{\xi\, G_I}\left\{\left[c\left(1 + C + {\lambda_c}^2 C\right) + dC\right]\right\} \tag{2.57}$$

and α derived from

$$\frac{Y_C}{Y_H} = \alpha^{\frac{1+\beta}{2}} \tag{2.58}$$

This approach works surprisingly well for $\xi < 1$, but if one is interested in greater refinement of the horn region (particularly regarding hot to cold length ratios greater than 1) one should see Rott's 1st paper and not make a linear 1st order approximation regarding the G-function. As the asymptotes (derived by the 1st order approximation regardless of length ratio) offer conservative bounds for the stability region, they should be sufficient for tube sizing purposes.

Experimental confirmation of the derived stability diagrams were first provided by Leinert et al. [26]; notably by Fuerst [28] for straight tube sections; and Yazaki, et al. [27] for U-shaped tubes. The worst case scenario (largest instability region) occurs when $\xi = 1$. For the SCU, the largest temperature ratio will be 293 K (ambient) to 4 K (liquid helium temperature).

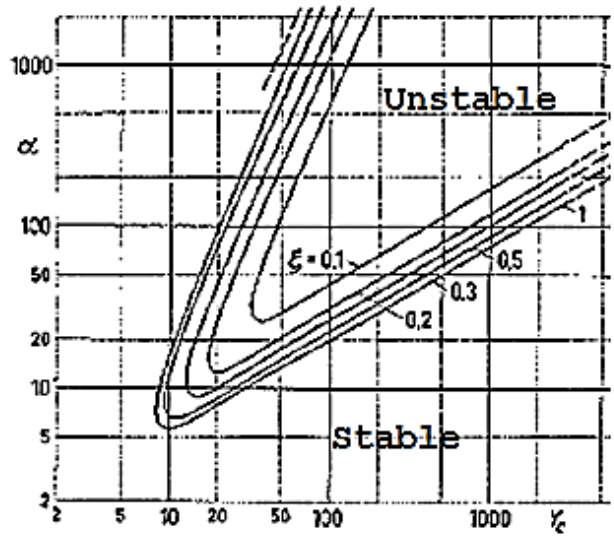

Figure 2.20. Stability curves of helium for $\xi < 1$ [24].

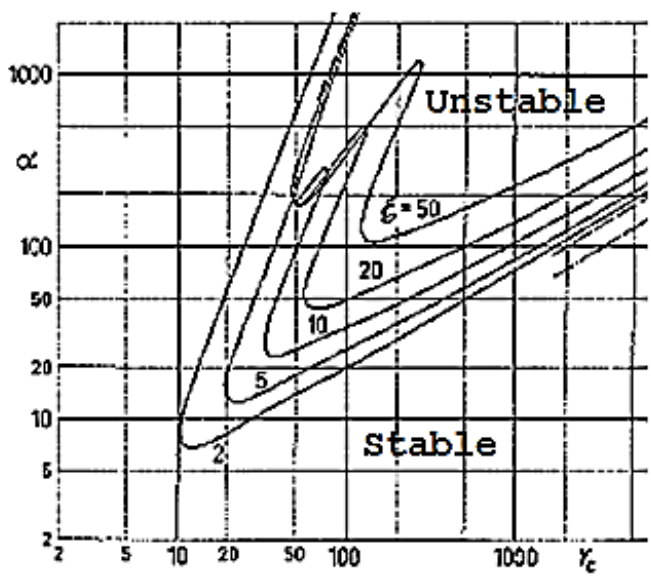

Figure 2.21. Stability curves of helium $\xi > 1$ [25].

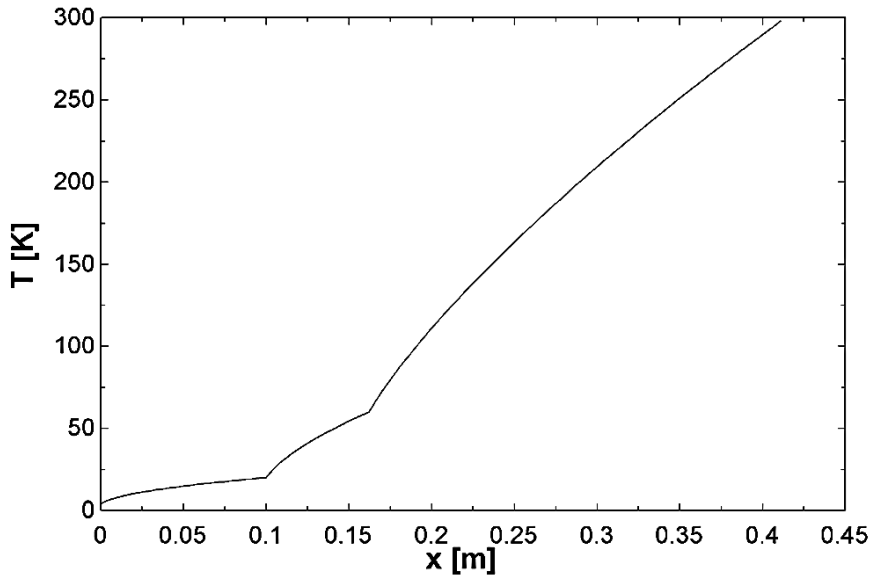

Figure 2.22. Anticipated temperature profile of SCU tubing into the helium reservoir based on 304 SS conductivity data from NIST [30, 31]. The method to generate the plot is outlined in Example 1.5-1 of [8]. This temperature profile allows for the determination of the steepness, *S*, at the two shield temperatures.

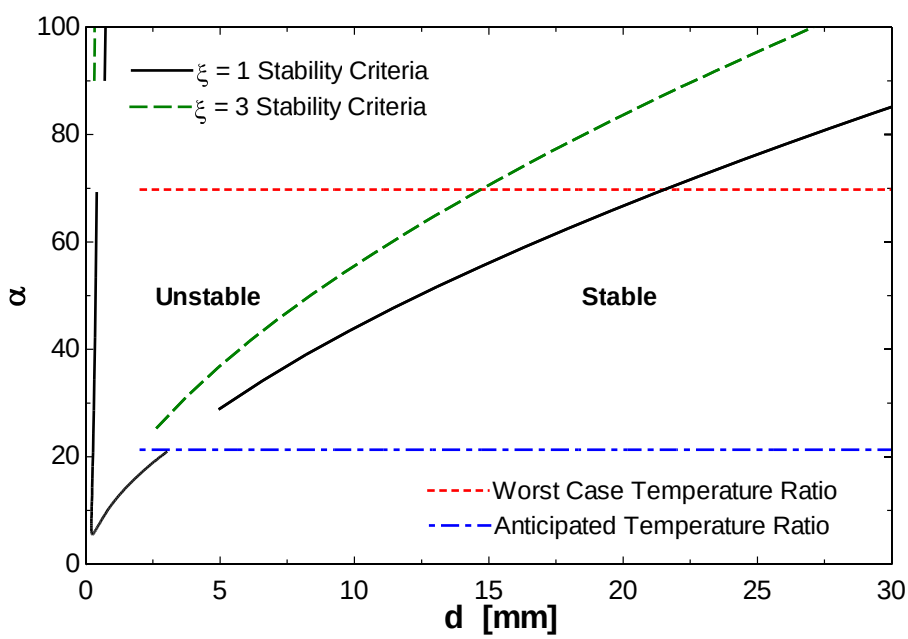

Figure 2.23. Stability diagram of temperature profile vs. tube diameter for SCU feed through sizing. An α of 70 and a ξ = 1 result in the worst case operating conditions (the broadest conditions to see TAOs). The anticipated α using the average cold side temperature is 21.3.

The total length of tubing entering the SCU cryostat is 0.41 m and the cold length is 0.1 m (the length exposed to the helium reservoir to the 20 K shield). Ignoring the cold length and assuming balanced hot to cold lengths of 0.2 m (ξ = 1 is the optimum conditions for TAO occurrence) results in a recommended tube diameter of 21.5 mm. The called out diameter for the SCU is currently 11.7 mm. However, the cold length temperature should be thought of as the mean temperature of the section to the 20 K shield (T_{CMean} = 14 K) and not just the coldest end point. Using this integrated average results in an α value of 21.3, corresponding to a tube diameter of 3 mm. Even this temperature ratio is being conservative in its α designation as it does not use the integrated average of the hot side temperature. As the actual ξ is 3 (the total length of the SCU piping is 0.41 m), both of these estimates are further cautious in their minimum diameter calculation. (Note that the oscillations should not exist at a cold length of 0.16 m – the 60 K shield as indicated in FIGURE 2.22 – because the temperature ratio, α, must be a minimum of 5.5 for ξ = 1. If a cold length of 0.16 m is assumed, the recommended diameter size to ensure avoidance of TAOs is 19.3 mm.)

If, for some reason, TAOs do occur, several solutions are available. If possible, the best solution is to change the pipe's diameter to avoid the "unstable" region. Assuming that no adjustments can be made, several common solutions can be implemented:

- Heat sink the tube to a different location, adjusting the hot to cold length ratio to avoid the TAO region.
- Insert an additional tube in order to make an annular channel, reducing the hydraulic diameter. Although it will result in an additional conduction path and increase the heat load somewhat, the increase will be smaller by orders of magnitude than that associated with TAOs.

- Place restrictions, such as baffles or bends, near the cold end.
- If possible (not in the case of the SCU, drill holes in the tube to increase wave losses.
- Roughen the tube walls in an attempt to increase the losses that are associated with turbulence.
- As a last resort, install mechanical damping boxes/encasements as outlined by Luck and Trepp [29].

2.6 References

1. Colebrook, C.F. "Turbulent Flow in Pipes with Particular Reference to the Transitional Region between the Smooth and Rough Pipe Lengths," *J. Inst. Civil Eng.*, Volume 11, pp. 133-156, 1939.
2. Petukhov, B.S. "Heat Transfer and Friction in Turbulent Pipe Flow with Variable Physical Properties," *Advances in Heat Transfer*, Volume 6, pp. 503-564, 1970.
3. Huang, X., *Hydrodynamic Study of One Dimensional Two-Phase Helium Flow*, Ph.D. Dissertation, University of Wisconsin-Madison, 1994.
4. Khalil, A.K., *Cryogenic Two-Phase Flow Characteristics of Helium 1 in Vertical Tubes*, Ph.D. Dissertation, University of Wisconsin-Madison, 1978.
5. De la Harpe, A. et al., "Boiling Heat Transfer and Pressure Drop of Liquid Helium I Under Forced Circulation in a Helically Coiled Tube," *Advances in Cryogenic Engineering*, Volume 14, pp. 170-177, 1969.
6. Nakagawa, S. et al., "Pressure Drop and Heat Transfer in Helium Two-Phase Flow," *Proceedings of the ICEC*, Volume 10, Butterworth, Guilford, UK, pp. 570-573, 1984.
7. Katheder, H., and Suβer, M., "Results of Flow Experiments with Two-Phase Helium for Cooling Superconductors," *Proceedings of the ICEC*, Volume 12, Butterworth, Guilford, UK, pp. 207-211, 1988.
8. Nellis, G.F., and Klein, S.A., *Heat Transfer*, Cambridge University Press, New York, pp. 655, 2009.
9. White, F.M., *Fluid Mechanics: Fifth Edition*, McGraw-Hill, Chapters 6.7-6.12, 2005.
10. "Flow of Fluids through Valves, Fittings, and Pipes," *Crane Company Technical Paper 410*, Chicago, 1979.
11. Bean, H.S. (ed.), *Fluid Meters: Their Theory and Application – Sixth Edition*, American Society of Mechanical Engineers, New York, 1971.
12. Theilacker, J.C., and Rode, C.H., "An Investigation into Flow Regimes for Two-Phase Helium Flow," Cryogenic Engineering Conference/International Cyrogenic Materials Conference, St. Charles, Illinois, 1987.
13. Memedov, I.S., et al., "Hydrodynamic Characteristics of a Horizontal Channel with the Motion of Two-Phase Helium Flow," *Journal of Engineering Physics*, Volume 44, Number 5, pp. 483-486, May 1983.
14. Filippov, Y.P., "Characteristics of Horizontal Two-Phase Helium Flows: Part 1 – Flow Patterns and Void Fraction," *Cryogenics*, Volume 39, pp. 59-68, 1999.
15. Alexeyev, A.I., Filippov, Y.P., Mamedov, I.S., "Flow Patterns of Two-Phase Helium in Horizontal Channels," *Cryogenics*, Volume 31, pp. 330-337, 1991.
16. Taitel, Y., and Dukler, A.E., "A Model for Predicting Flow Regime Transitions in Horizontal and Near Horizontal Gas-Liquid Flow," *AlChE Journal*, Voluume 22, pp. 47-55, 1976.
17. Thome, J.R., and Hajal, J.E., "Two-Phase Flow Pattern Map for Evaporation in Horizontal Tubes: Latest Verision," *Heat Transfer Engineering*, Volume 24(6), pp.3-10, 2003.
18. Kuber, J., "The presence of slug flow in horizontal two-phase flow," *Internation Journal of Multiphase Flow*, Volume 5(5), pp. 327-339, 1979.
19. Baudouy, B., "Heat and Mass Transfer in Two-Phase Helium I Thermosiphon Flow," *AIP Conference Proceedings*, Volume 613, pp. 1514-1524, May 2002.

20. Jeng, H.R., and Pan, C., "Analysis of Two-Phase Flow Characteristics in a Natural Circulation Using the Drift-Flux Model Taking Flow Pattern Change and Sub-Cooled Boiling into Consideration," *Annals of Nuclear Energy*, Volume 26, Issue 14, pp. 1227-1251, September 1999.
21. Hands, B.A. (ed.) , *Cryogenic Engineering*, Acamdemic Press, London, 1986.
22. Kuncoro, et al. "Experimental Study on the Geysering Mechanism in a Closed Two-Phase System," *Memoirs of the Faculty of Engineering*, Kyushu University, Volume 55, Number 3, pp. 333-348, September 1995.
23. Rott, N., "Damped and Thermally Driven Acoustic Oscillations in Wide and Narrow Tubes," *ZAMP*, Volume 20, pp. 230-243, 1969.
24. Rott, N., "Thermally Driven Acoustic Oscillations. Part II: Stability Limit for Helium," *ZAMP*, Volume 24, pp. 54-73, 1973.
25. Rott, N., "Thermally Driven Acoustic Oscillations. Part III: Second Order Heat Flux," *ZAMP*, Volume 26, pp. 43-49, 1975.
26. Lienert, U., van Hoffman, T., and Quack, H., "Experiments on Thermally Driven Gas Oscillations," *Cryogenics*, Volume 13, pp. 490, 1973.
27. Yazaki, T., Tominaga, A., and Narahar, Y., "Stability Limit for Thermally Driven Acoustic Oscillations," *Cryogenics*, Volume 19, pp. 393, 1979.
28. Fuerst, J., "An Investigation of Thermally Driven Acoustical Oscillations in Helium Systems," *Low Temperature Engineering and Cryogenics Conference and Exhibition*, July 17-19, 1990.
29. Luck, H., and Trepp, Ch., "Thermoacoustic Oscillations in Cryogenics. Part 3: Avoiding and Damping of Oscillations," *Cryogenics*, Volume 32, pp. 703-706, 1992.
30. Mann, D. (ed.), *LNG Materials and Fluids*, National Bureau of Standards, Cryogenics Division, First Edition, 1977.
31. Touloukian, Y.S., and Ho, C.Y. (eds.), *Thermophysical Properties of Selected Aerospace Materials – Part II: Thermophysical Properties of Seven Materials*, 1976.
32. Rayleigh, J.W.S., *The Theory of Sound*, Volume II, MacMillan, 1940.
33. Taconis, K.W., et al, "Measurements Concerning the Vapour-Liquid Equlibrium of Solutions of He^3 in He^4 below 2.19 K," *Physica*, Volume 15, pp. 733, 1949.

3 Experimental Apparatus

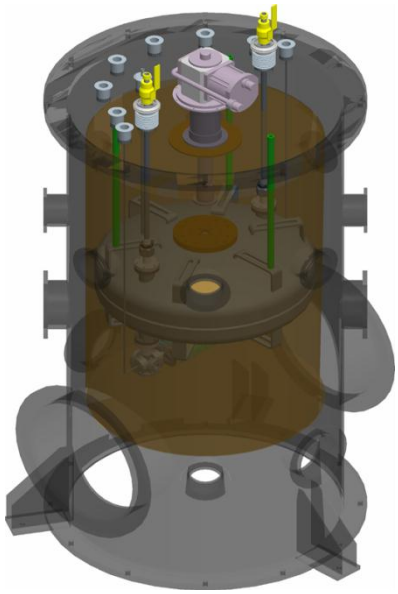

Figure 3.1. Three dimensional, transparent representation of experimental assembly.

3.1 Experiment Description

The experimental test rig to verify the thermodynamic model is assembled on-site at Argonne National Lab (ANL) and consists of four principle components (discussed further in sections 3.1.1-3.1.4): a vacuum chamber, a helium vessel, horizontal piping/test sections, and a Venturi flow element. Two different horizontal flow networks are used in the experiment – a single channel assembly and a three-channel assembly modeled after the SCU core design. Both verify mass flow induced by heat application from a differential pressure measurement located at an upstream Venturi. As the SCU cooling system is based on internal convection, the two test geometries are studied to protect against the possibility of poor dimensioning in the SCU flow network significantly hindering the flow rate. The three-channel assembly's side channels are offset by 6.35 mm and will ideally show a difference in operation whether oriented above or below the center channel, indicating the presence of stratified flow (see FIGURE 3.6). Electrical elements are described in greater detail in sections 3.2.1-3.2.5 and include: temperature sensors,

heaters, a pressure transducer, and a liquid level probe. A complete piping and instrumentation diagram follows the component's introductions and is seen in FIGURE 3.8. To maintain consistent saturation conditions, the test is ran as an open loop venting to the environment, but the experiment has the ability to operate in a closed loop mode to mimic the actual superconducting undulator (SCU) cooling cycle.

3.1.1 Vacuum Chamber

The vacuum chamber is modified from a previous experiment performed at the Intense Pulse Neutron Source (IPNS) at ANL. A new top plate was manufactured with the necessary port holes and feed throughs, as well as a mounting pattern for the Sumitomo 415D cryocooler that cools the radiation shielding and will eventually provide recondensing capacity when operated in a closed loop mode. The chamber's diameter is 0.76 m and its height is 1.46 m. It is set up to can contain the geometries mimicking 42-pole SCUs when oriented vertically and can hold 144 pole test geometries when laid on its side.

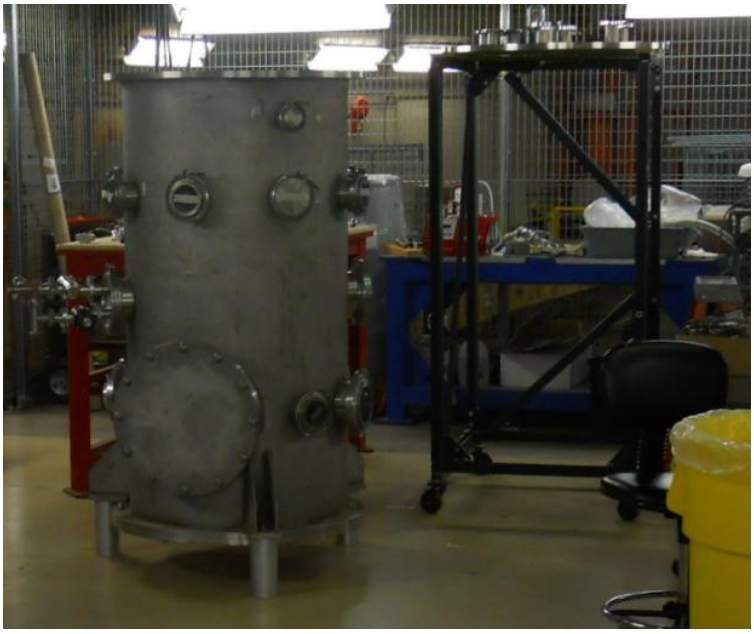

Figure 3.2. Vacuum chamber used in experimental assembly.

3.1.2 Helium Vessel

Figure 3.3. Helium vessel and support structure.

The helium vessel is constructed of two 0.6 m (inner diameter) flanged and dished (F&D) heads welded together made from 304L stainless steel. A copper plate, welded to the top of the upper F&D head will connect the 2nd stage of the cryocooler to the helium vessel when recondensing is required. CF flanges are used to attach all piping from the helium vessel to the top and bottom ports of the vacuum vessel, and a carbon burst disk rated at 15 psi is combined with 2 psi and 7.5 psi relief valves to guard against pressure buildup in the helium reservoir. The vessel is designed and manufactured according to ASME Section IID – UG-32/33 and was fabricated by Meyer Tool in Chicago. The F&D helium vessel maintains a consistent liquid level over a prolonged period of time, resulting in a relatively constant hydrostatic head. The time required for the liquid level to drop 25 mm (8%), calculated from equation (3.1) is 3.3 hours assuming a continuous heat load of 1.5 W.

$$\frac{\pi * d^2 * \Delta L}{4} * \rho_{liq} * \left(h_{vap} - h_{liq}\right) = \dot{Q} * time \tag{3.1}$$

3.1.3 Piping and Test Sections

In order to closely model the SCU0 cryostat, all piping and test sections are made out of 19 mm OD 304 Stainless Steel tubing with 1.65 mm walls. The inlet and outlet legs of the thermosiphon test section both have two 76.2 mm radii elbows to connect the vertical components to the horizontal test section, and a single flexible bellows to help with leveling and adjusting the fit. Tee flanges to align the test section are located at both the entrance and exit to the horizontal test section. The return line of the thermosiphon extends into the center height of the helium vessel. The vertical distance between the liquid level in the reservoir and the center plane of the horizontal test section defines a 0.31 m hydrostatic head. FIGURE 3.4 shows the three-channel test section assembled to the reservoir. The stainless steel return line appears in the right foreground and extends back while the stainless steel supply line appears on the left. The Venturi is located at the back at the back.

Figure 3.4. Three-channel test assembly installation.

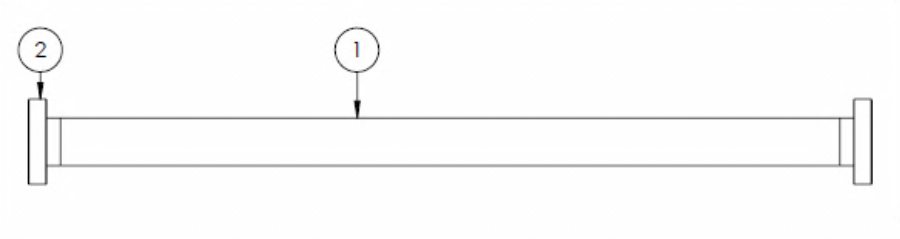

Figure 3.5. Single channel test assembly. 1 – single channel tube, 2 – ConFlat Flange.

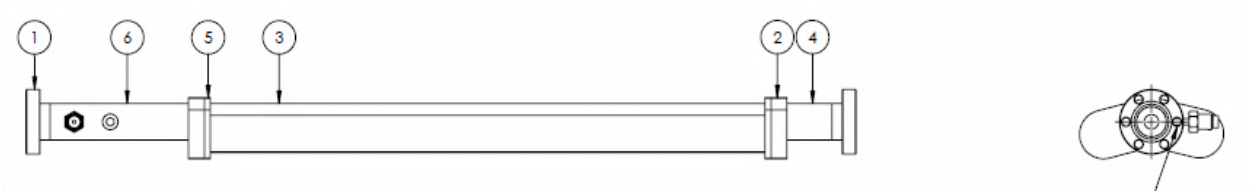

Figure 3.6. Three-channel test assembly. 1 – ConFlat flange, 2 – plenum, 3 – channel piping, 4 – piping extension, 5 – plenum plate, 6 – Venturi.

Two test sections were made: a single channel pipe and a three-channel weldment. The single channel, seen in FIGURE 3.5, has 33.8 mm mini ConFlat flanges welded to both ends and is installed with a separate Venturi (discussed in section 3.1.4). Its testing is to verify the concept of a thermosiphon and ensure that any lack of flow is not a problem of poor channel design. The three-channel assembly shown in FIGURE 3.6 has a Venturi welded in place and plenums located at the entrance and exit to expand and contract from one pipe to three. The two side channels are offset 6.35 mm to mimic the SCU core design and will ideally show a difference in operation whether oriented above or below the center channel, indicating the presence of stratified flow.

3.1.4 Venturi Flow Element

As the SCU cooling system is based on creating an effective flow rate, its quantification is the principle concern. The features that have been considered in the choice of the flow meter include robustness, the ability to act as a backup for quench detection when testing the superconducting undulator magnets, stability in cryogenic environments, and insensitivity to magnetic fields. Several measurement options are available, but all have disadvantages

compared to a Venturi. Turbine flow elements have a low pressure drop but have significant errors at low flow rates and are sensitive to magnetic fields. Coriolis meters require magnetic shielding and have had limited success in cryogenic environments. Ultrasonic and correlation flow meters send either wave patterns or turbulent oscillations down and upstream on the horizontal test section and relate time delays to flow rate, but require sensitive instrumentation and work best under well-mixed flow [1]. In contrast, Venturis have been successfully used in cryogenic environments, are not impacted by strong magnetic fields, are somewhat inexpensive, and have modest pressure losses.

A Venturi is governed by Bernoulli's principle. Simply put, a reduction in area requires acceleration because of mass continuity, and the acceleration causes a decrease in static pressure. By knowing the upstream and throat areas and measuring the pressure difference between the two locations, the flow rate for a single phase, inviscid system can be determined by equation (3.2)

$$\frac{1}{{A_{throat}}^2} - \frac{1}{{A_{inlet}}^2} = \Delta P * 2 * \frac{\rho_{liq}}{\dot{m}^2} \tag{3.2}$$

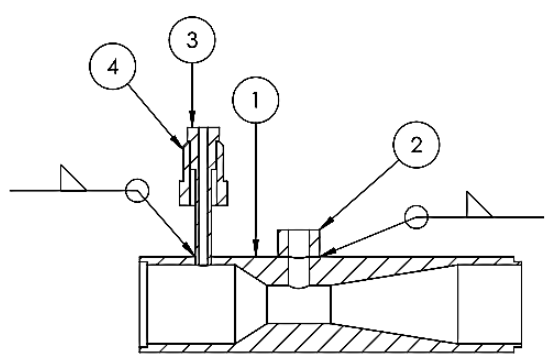

Figure 3.7. Venturi assembly section view. 1 – Venturi body, 2 – Venturi tap connection, 3 – Swagelok VCR fitting to connect reference side of transducer, 4 – male VCR nut.

In the design of the Venturi, the independent variable is the throat diameter. The piping for this test fixture provides an inlet area of 195 mm^2. For the head height of 0.31 m, the corresponding pressure head is 384 Pa. The density of liquid helium is 125 kg/m^3. The maximum anticipated flow rate is 13.5 g/s for an applied load of 3 W. In order to protect against entering the vapor dome and avoid the contraction-induced pressure drop exceeding the available pressure head, the throat diameter is determined to be 0.3 inches. The Venturi, manufactured at the University of Wisconsin-Madison College of Engineering shop, is shown in FIGURE 3.7. The angle of convergence is relatively steep, ~60^0, but nozzled sections tend to have relatively small losses. The total divergence angle is ~18^0.

3.1.5 Other Principal Components

A Pfeiffer Vacuum HiCube Turbo pumping station (TSH 071) is connected to the cryostat with a KF-50 flange. The pressure inside the cryostat during operation settles at ~1E-7 mbar with pump down taking approximately 2 days. A Sumitomo 415D cryocooler provides cooling for the copper radiation shield by its connection to the first stage of the cold head. The shield temperature of 22-24 K limits the radiation load to the experimental assembly and reduces boil off. As previously mentioned, the second stage of the cryocooler is positioned to connect to the helium vessel with high purity copper brackets and function as a recondenser in future closed-loop tests.

3.2 Experiment Instrumentation

The piping and instrumentation diagram is shown in FIGURE 3.8. Eight temperature sensors, four heaters, one pressure transducer, and one liquid level probe are recorded. TABLE 3.1 defines the notation used in the piping and instrumentation diagram according to ANSI/ISA S5.1.

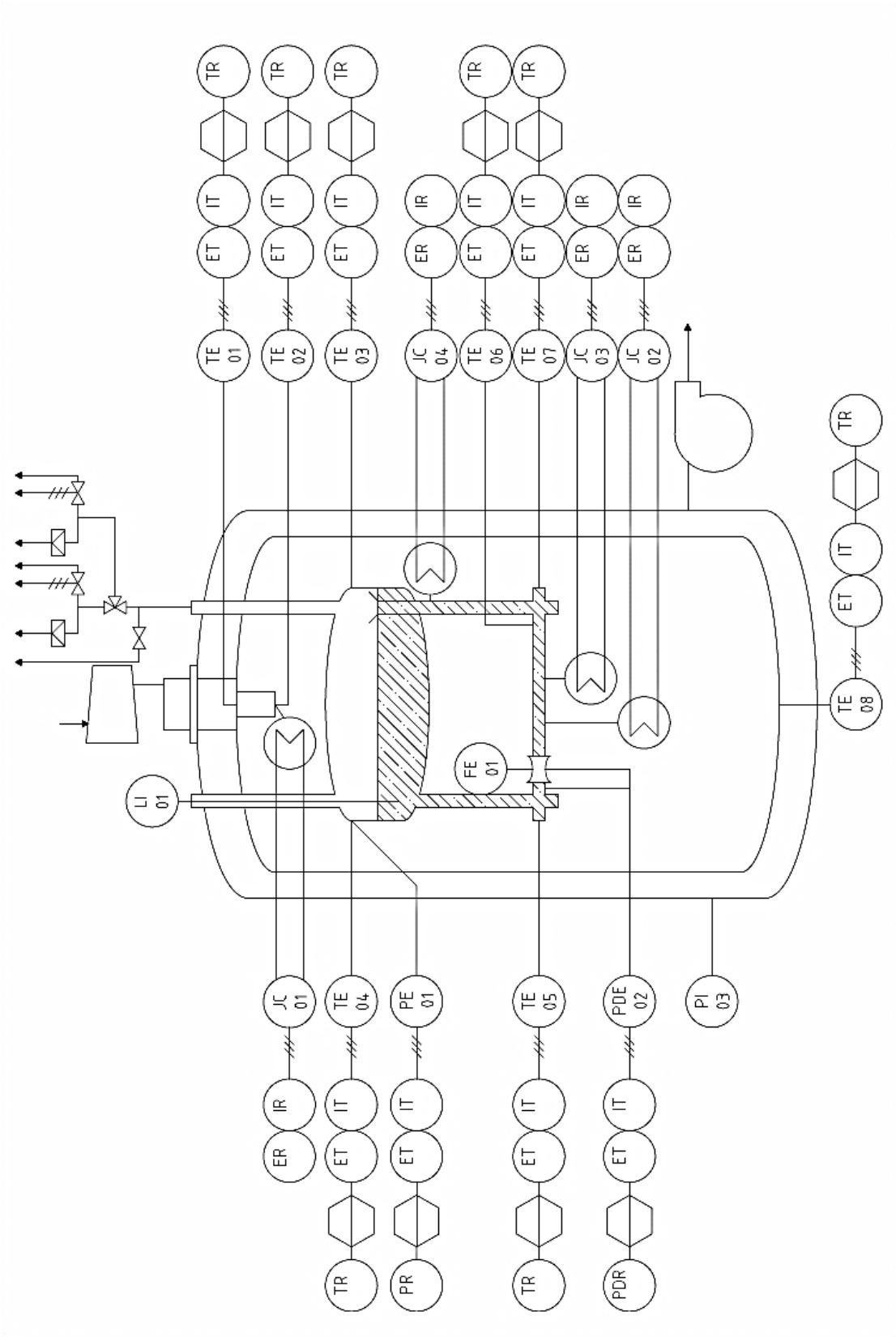

Figure 3.8. Piping and instrumentation diagram for thermosiphon test apparatus.

1st Letter	Represented Variable	2nd Letter	Represented Function
L	Level	D	Differential
J	Power	R	Recorder
T	Temperature	T	Transmitter
I	Current	I	Indicator
E	Voltage	E	Element
P	Pressure	C	Controller

Table 3.1. Instrumentation schematic notation.

3.2.1 Temperature Sensors

Lakeshore Cernox-SD sensors calibrated from 1.4-300 K are used for all temperature measurements. At 4.2K, the sensors have an accuracy of 5 mK for the first year of use and 25 mK long term stability. Lakeshore's 218 Cryogenic Temperature Monitor, which stores a 10th order polynomial to correlate the thin film resistance to a temperature, communicates with the data acquisition system. These sensors have high accuracy and low heat dissipation, and they are insensitive to magnetic fields. All temperature sensors are attached externally to the tubing or helium vessel rather than internally to avoid leak avenues. Good thermal contact between the sensor and the tubing is achieved through a coating of Apiezon N grease and they are shielded with several layers of multi-layer insulation (MLI) to limit radiation impact.

3.2.2 Heaters

Four Minco Kapton heaters are installed on the test apparatus – three to regulate the flow and one to regulate the cryocooler performance. Heater 1 (JC 01) is located on the second stage of the cryocooler and is unused. Heaters 2 and 3 (JC02 and JC03) are located on the horizontal leg of the thermosiphon loop – heater set 2 representing localized heating to the ends of the horizontal test section and heater set 3 representing distributed heat flux along the channels. Both heating sets consist of multiple heaters of the same resistance that are wired in series to provide uniform heat application. Heater 4 (JC04) is located on the vertical return leg and acts as a regulating mechanism. FIGURES 3.4 and 3.9 show the heaters as installed on the three-

channel test assembly. The horizontal assembly is covered in 20 layers of MLI to reduce interaction with the shield and the helium tank as shown in FIGURE 3.10.

To validate the heaters, a method similar to the hold-time calculation is used. First, the parasitic heat leak is determined by equation (3.1) by measuring the liquid level drop over the

Figure 3.9. Heaters installed on the three-channel assembly.

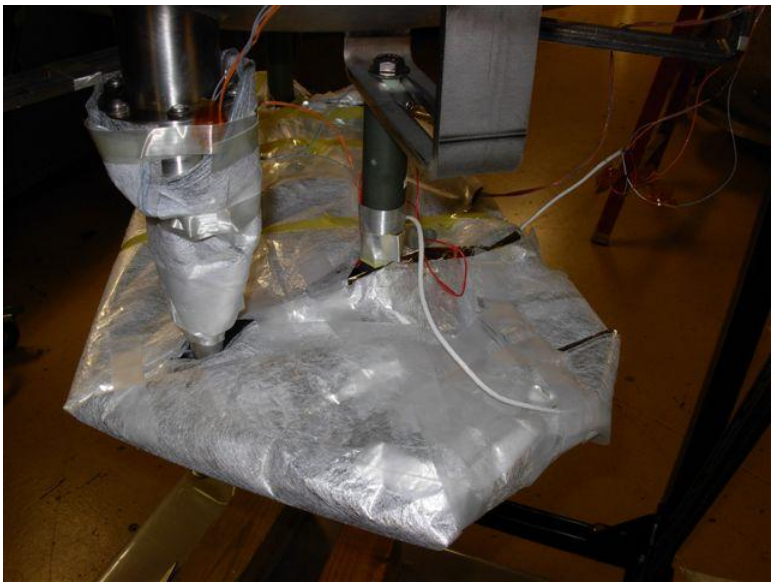

Figure 3.10. Horizontal test assembly covered in 20 layers of MLI.

course of a day or more. The load from each heater is individually confirmed over a number of hours and comparing the integrated average heat load to the observed level drop

$$\frac{\pi * d^2 * \Delta L}{4} * \rho_{liq} * \left(h_{vap} - h_{liq}\right) = \bar{\dot{Q}}_{observed} * time + \bar{\dot{Q}}_{parasitic} * time \tag{3.3}$$

The observed heat load is compared with the applied heat load, and their relationship reported

$$PF = \frac{\bar{\dot{Q}}_{observed}}{\bar{\dot{Q}}_{applied}} \tag{3.4}$$

As will be mentioned in section 3.2.3, the sensitivity of the liquid level probe is 1 mm. Consequently, the heater calibration uncertainty is entirely dependent on the allowed level drop. Reported power factors (PF), uncertainties, and baseline heat leaks for the three tests are shown in TABLE 3.2.

	Heat Source	Load (W)	Power Factor	+/- Uncertainty (%)
Single Channel Test	Parasitic	0.3059		
	Horizontal (JC 02)		0.9348	9.021
	Horizontal (JC 03)		0.837	8.8837
	Vertical (JC 04)		1.09	8.583
Three-channel Test	Parasitic	0.2499		
	Horizontal (JC 02)		0.9204	3.04
	Horizontal (JC 03)		0.9469	3.861
	Vertical (JC 04)		0.9798	2.251
Three-channel Test	Parasitic	0.2564		
	Horizontal (JC 02)		0.9125	6.155
	Horizontal (JC 03)		1.004	6.664
	Vertical (JC 04)		0.9913	1.837

Table 3.2. Heater characterization for three test runs.

3.2.3 Liquid Level Indicator

The helium level probe is a 305 mm, 4-wire AMI sensor that is connected to an AMI model 316 controller that is interfaced to the data acquisition system. It has a resolution of 1 mm, is updated every 3 seconds, and is interfaced through an RS-232 port.

3.2.4 Differential Pressure Transducer

A modified Kulite CT-190 (100 mV, 5 psi full scale) cryogenic wind tunnel transducer is mounted on the Venturi flow meter, providing the differential pressure measurements. The sensor has a silicon-packed housing with a Pyrex diaphragm. Certain glasses, like Pyrex, are penetrable to helium at room temperature, making leak-checking procedures somewhat problematic. However, as the glass gets colder and thermally contracts, helium no longer diffuses through the glass and the leak goes away. Kulite reports the expected leak rate in these sensors to be ~1E-10 mbar-L/s at room temperature, but the observed rate for the sensor used is on the order of 2E-8 mbar-L/s [2]. The difference is likely due to deformations/inconsistencies in the installed Pyrex plate.

That the CT-190 is a self-confined and entirely electrical transducer is particularly advantageous for pressure measurements in cryogenic environments. External measurements gathered via small diameter transfer lines extending out of the cryostat prevent an alternative approach. However, these create a direct conduction path to the Venturi. Aside from possible instabilities due to thermoacoustic oscillations (as discussed in section 2.5), the long capillary tubes compound uncertainties in the pressure measurement due to the possibility of condensation in the piping, and that possibility in turn depending on a number of ill-defined parameters [3].

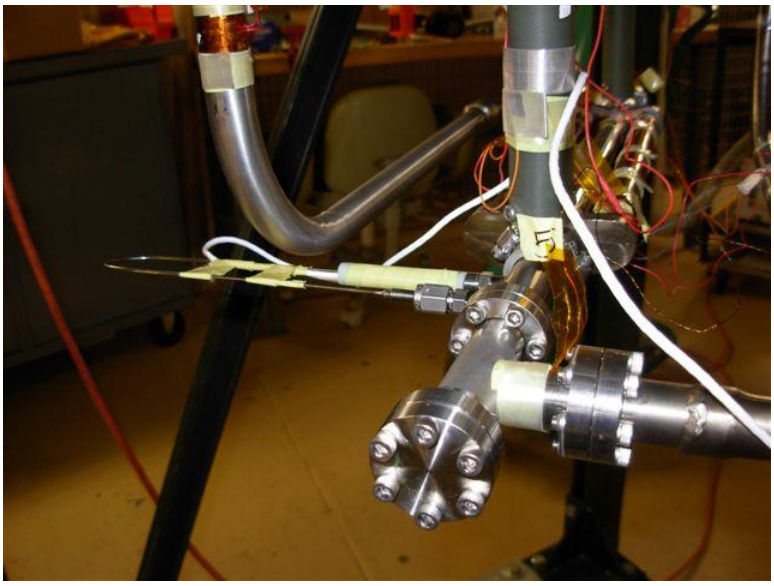

Figure 3.11. Kulite CT-190 installed with reference port extension.

The pressure transducer was mounted to the Venturi in a differential mode by silver-brazing an extension to the reference port of the transducer and connecting this to the upstream area of the Venturi, as shown in FIGURE 3.11. The CT-190's reported response is 16.512 mV/psi in the operating range of 77 K to 300 K. Because this experiment occurs at much colder temperatures, the transducer is not NIST traceable, and its stability over such a large temperature range is uncertain, a separate calibration of the CT-190 has been performed, as described in section 3.3.

3.2.5 Other Principle Electrical Equipment

Other principle electrical equipment includes two TENMA 3-phase power supplies (models 72-6856 and 72-2080) to control the Minco heaters and an Agilent E3615A 10 VDC power supply for the Kulite pressure sensor.

3.3 Pressure Transducer Calibration

The schematic for the pressure calibration apparatus is shown in FIGURE 3.12. The reference transducer is a temperature compensated Dwyer High Accuracy Differential Pressure

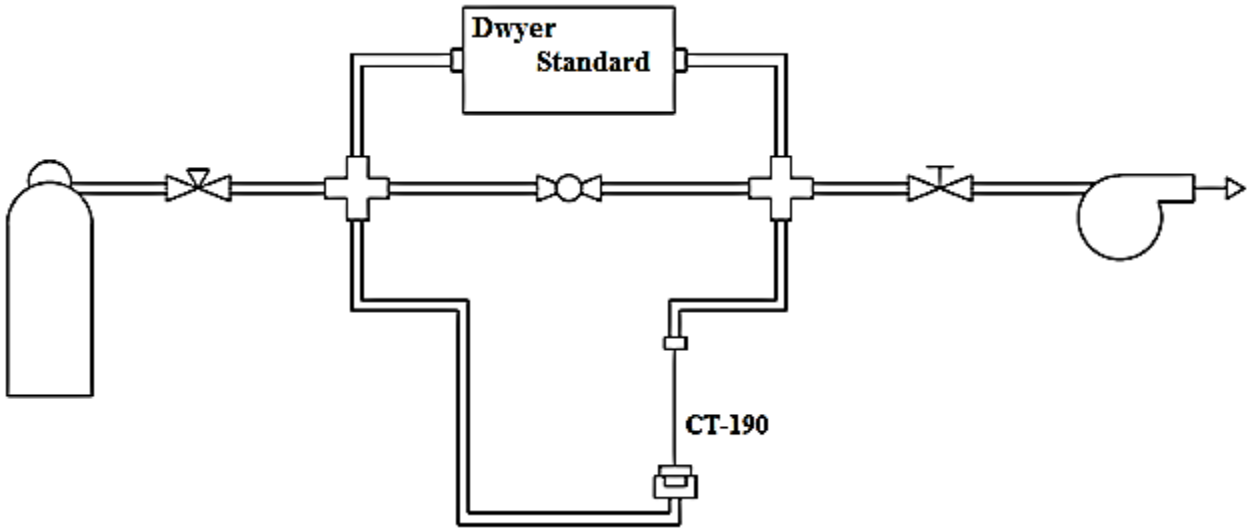

Figure 3.12. Pressure transducer calibration schematic.

Transmitter that comes with NIST traceable certification. Full scale response is 5 VDC over 625 Pa with an accuracy of +/- 0.14% (0.875 Pa). The Kulite transducer is connected to the Dwyer pressure transducer and lowered into a helium bath with the valves, Dwyer transducer, and other piping remaining outside the Dewar. With the needle valve closed and ball valve open, the entire system is evacuated. The vacuum-side valve is closed and helium is charged into the system near atmospheric pressure. The ball valve is then closed, and the helium supply's pressure is slightly increased and bled in through the needle valve, creating differential pressures. FIGURE 3.13 reports the output of the calibration process. The response at 4.2 K is 2.37445 μV/Pa with an RMS error of 16.709 μV/Pa. Uncertainty in each data point due to signal noise is less than +/- 10-15 μV, resulting in a pressure measurement error on the order of 5 Pa or 0.5 g/s (per results discussed in Chapter 4). It should be noted that the zero offset drifts considerably between runs from day to day and the data must be adjusted appropriately to compensate.

Interestingly, if the calibration procedure is done referencing vacuum and not a reasonably-charged pressure, the response seen in FIGURE 3.14 occurs. On the surface, differential pressures created with reference to vacuum would be ideal, with a stable reference

signal and minimum helium in the system to skew the calibration due to condensation or thermoacoustic oscillations. Based on the response, however, either helium is diffusing through the sensing medium of Dwyer transducer at low differential pressures because of the vacuum and limiting its response, or the vacuum side is causing uneven strain in the fully active Wheatstone bridge of the Kulite transducer.

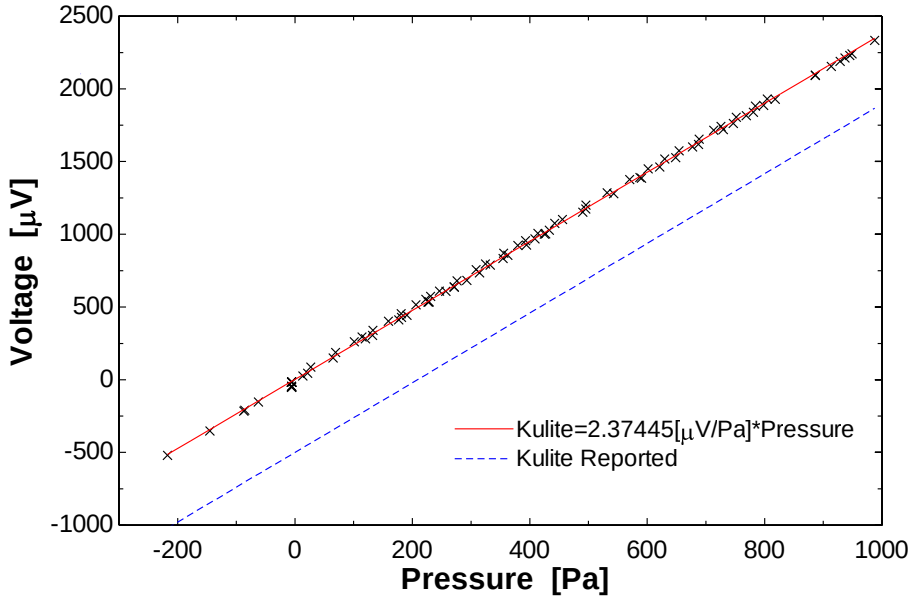

Figure 3.13. Kulite CT-190 pressure transducer response at 4.2 K.

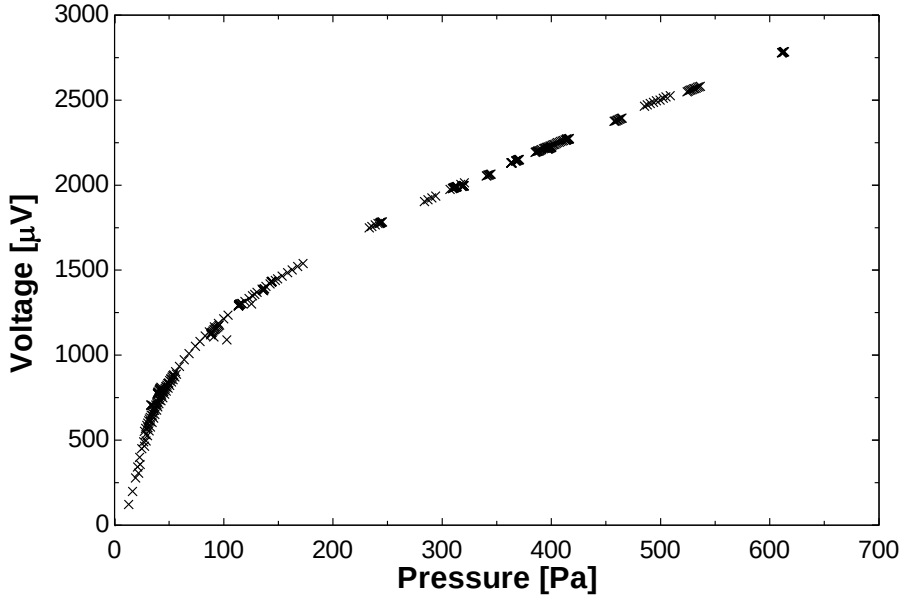

Figure 3.14. Kulite CT-190 pressure transducer response at 4.2 K referencing vacuum.

3.4 Data Acquisition System

Data acquisition is interfaced through a National Instruments PXI chassis and LabVIEW vi. The chassis, with 24-bit discretization, directly reads the Kulite pressure transducer to create the cleanest signal possible. The voltage reading can be narrowed down to +/- 316 mV, resulting in 37.6 nV resolution (1.298 mPa) – well below the background noise. Two 22-bit Keithley 2700 data acquisition systems monitor the voltage and current measurements for the heaters and are linked to the PXI system. As discussed earlier, temperature and level measurements are gathered by self-subsistent equipment and then relayed to LabVIEW. 40 differential pressure measurements are sampled at a frequency of 100 Hz every 3 seconds to minimize the impacts of noise and aliasing. The clocking time of the data acquisition system requires a minimum of 2.4 seconds to record one set of all the measurements.

3.5 Experimental Procedure

After assembly and instrumentation, the helium vessel is checked for leaks prior to insertion into the vacuum vessel by evacuating the assembly and spraying helium around the joints and flanges of the assembly. The residual background reading for leak rates in the SCU staging area is 1.2-1.4E-10 mbar-L/s. The entire assembly outside of the pressure transducer (PDE 02) should not indicate any rise in the leak rate reading. As mentioned earlier, the Kulite CT-190 contains a Pyrex plate in the diaphragm and a slight leak from the measurement side should be seen at room temperature. The leak rate observed (2E-8 mbar-L/s) is equivalent to 1 cc of helium leaking out over the course of one year or one 3 mm bubble leaking out over 10 days. Even a small leak such as this can spoil the vacuum in a cryogenic experiment. As a result, the turbo vacuum pump continues to pump out the vacuum vessel during the entire experimental procedure.

Following the leak check of the helium storage tank and a final check of the instrumentation, the helium vessel and top plate are lowered into position on the vacuum chamber. The vacuum chamber is then sealed, evacuated and checked for leaks in the same manner as the helium tank/test apparatus. The helium tank is then re-evacuated and back filled with helium gas, which acts as a secondary indicator if the helium tank or test assembly develops a leak during the evacuation of the vacuum chamber. The process avoids the use of nitrogen gas due to the possibility that it could become trapped in the pressure transducer's capillary tube and subsequently freeze when the system is filled with liquid helium. The helium vessel is then pumped down again and refilled with helium gas another time.

If the system is confirmed to be leak tight, the GM cryocooler is turned on to pre-cool the radiation shield. The shield, connected to the first stage of the cryocooler, cools down over a period of 5-8 hours. Following this, gaseous helium from a liquid helium Dewar is vented into the helium vessel as a means to pre-cool the helium storage tank and experimental assembly. After the system is pre-charged and reasonably cool (indicated by temperature elements #3-7), in order to avoid large and rapid amounts of liquid boil-off, liquid helium is slowly transferred into the storage vessel. The reservoir is sufficiently full when the helium level indicator reads between 147 and 157 mm from its sensing location on the edge of one of the bottom ports of the dished surface. The test measurements are initiated after the system has equilibrated, as indicated by steady state readings from all temperature and pressure sensors.

The testing procedure progresses as follows:

1. Heat is incrementally applied to the horizontal section via JC02, with values ranging from ~0.25 W to ~3.5 W. The system is allowed to stabilize before

increasing the heat load. As mentioned in section 3.2.2, JC02 mimics localized heating to the ends of the horizontal section.

2. Heat is incrementally applied to the horizontal section via JC03 with values ranging from ~0.25 W to ~3.5 W. Again the system is allowed to stabilize between steps.

3. Heat is applied to the vertical leg, JC04, to simulate the regulating heater that will be in place on the actual core. JC04 is varied from ~0.25 W to ~3.5 W as in the other cases.

4. Finally, as time and helium supply permits, ~3.5 W are applied at JC04, and decreased incrementally while equivalently increasing the horizontal load, JC02, in order to simulate the actual regulating operation of the undulator core.

Care is taken during the entire procedure to maintain the helium level as stable as reasonably allowable, recharging when necessary.

3.6 References

1. Konstantinov, A., "A Review of the Liquid Helium Flow Rate Measurement Techniques at Some Operating Facilities with Superconducting Magnets," *Plasma Devices and Operations*, Volume 8, pp. 201-213, 2000.
2. VanDeWeert, J. and Kochman, B., "Hydrogen and Helium Transducers," Kulite Technical Note, pp. 1-6, November 2006.
3. Riovetti, A., Martini, G., Birello, G., "LHe Venturi Flowmeters: Practical Design Criteria and Calibration Method," *Cryogenics*, Volume 34, pp. 449-452, 1994.

4 Results

4.1 Raw Data Discussion

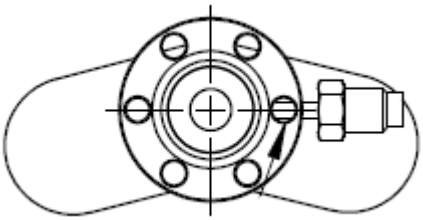

Figure 4.1a. Top core geometry orientation.

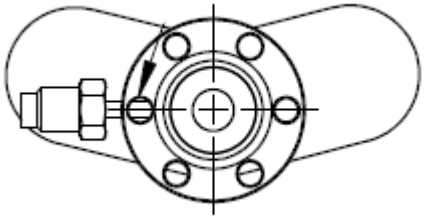

Figure 4.1b. Bottom core geometry orientation.

Data analyses for the thermosiphon test focus on the differential pressure measured at the Venturi and the subsequent flow rate calculation. The temperature sensors installed in the test rig provide a safeguard by ensuring that the test assemblies see a uniform temperature and monitoring for excessive heat loads.

Using the procedure outlined in section 3.5, three tests were performed. The first test focused on the single channel assembly and was used to verify the operating principles of the thermosiphon. The second test mimicked the orientation of the top core of the superconducting undulator magnet, as shown in FIGURE 4.1a's end view. The configuration used in the final test, shown in FIGURE 4.1b, is intended to characterize the cooling arrangement for the bottom core of the superconducting undulator.

The data sets for each test displayed large fluctuations depending on the location of heat application. The data gathered when power was supplied to the horizontal heaters included a widely varying signal while the data collected when heat was applied to the vertical return pipe was much more stable. The raw data files from the second test showing the signal from the differential pressure transducer vs. the heat load for the horizontal heating mode can be seen in FIGURE 4.2. The same type of data for vertical heating is shown in FIGURE 4.3. Based on the

observations from all three runs, there is no discernable difference between the two types of horizontal heat applications (localized vs. distributed). As a result, the analyses of the data from the two types of horizontal loads are combined in the presented results.

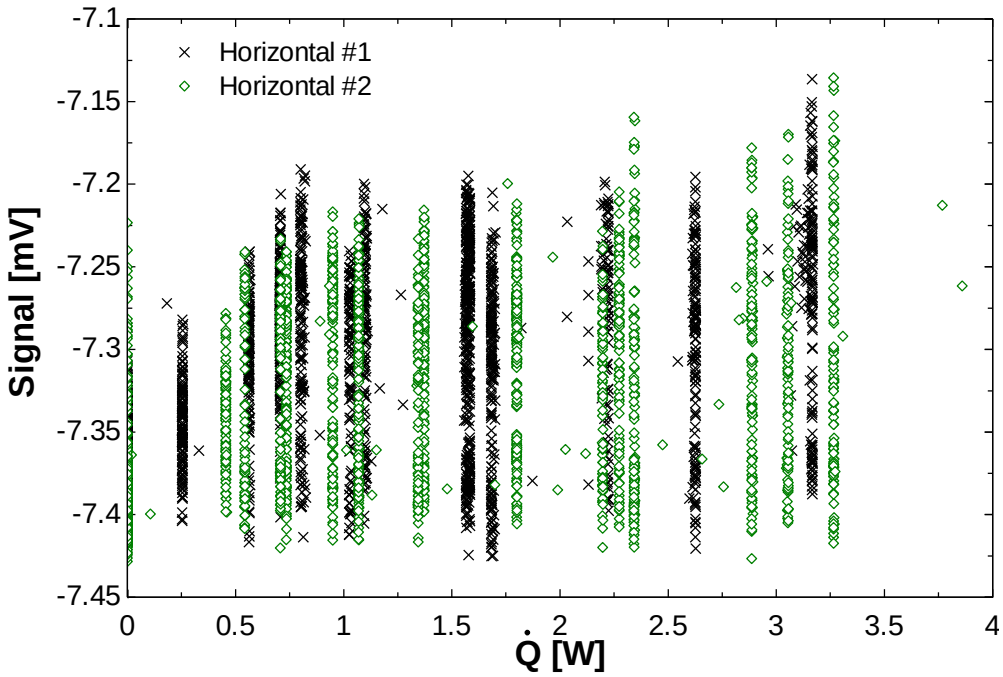

Figure 4.2. Transducer signal vs. horizontal heat load for top core geometry test. .

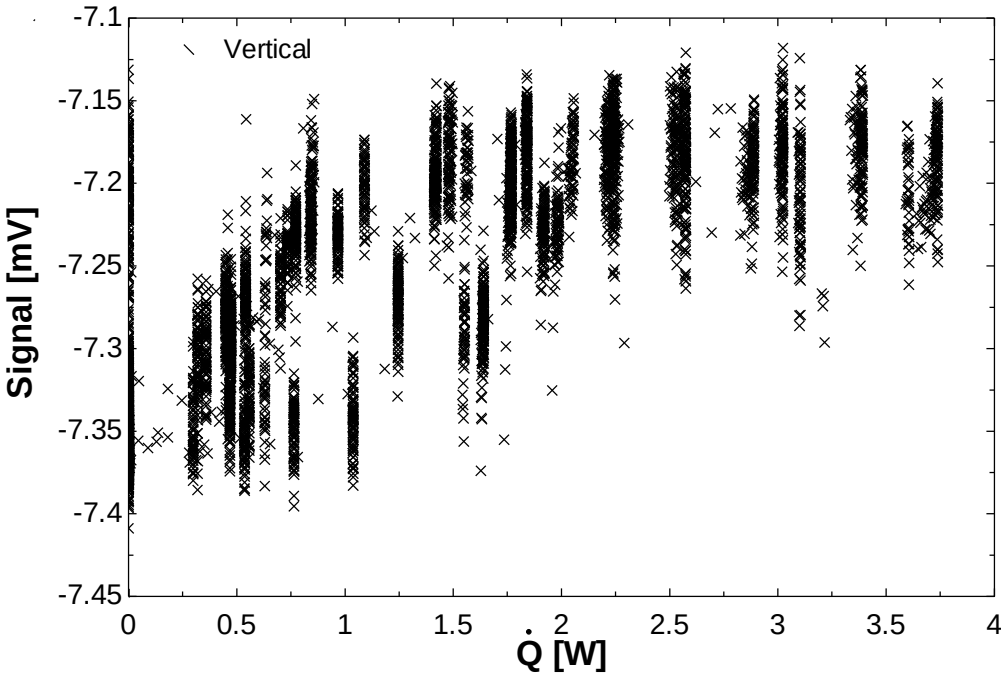

Figure 4.3. Transducer signal vs. vertical heat load for top core geometry test.

4.2 Single Channel Results

The single channel test was performed in order to validate the operating principles of the thermosiphon loop. The liquid level in the reservoir was maintained below the outlet of the return pipe in an effort to more closely mimic the operation on the superconducting undulator cryostat. The results from both the horizontal and vertical heating modes are similar.

FIGURE 4.4a presents the calculated mass flow rates from the single channel test as a function of the horizontal heat load. The error bars represent the standard deviation associated with the fluctuations of the mass flow rate, rather than the uncertainty in the transducer signal. In contrast, FIGURE 4.4b displays the same average mass flow rate but with the error bars representing the uncertainty of the transducer signal.

Parameter	Value
A_{inlet}	195 mm^2
A_{throat}	45.6 mm^2
ρ_{liq}	125.3 kg/m^3
Slope	2.37445 µV/Pa
Signal	Time-averaged signal
Standard Deviation	Standard deviation of time-averaged signal
Signal Uncertainty	~12 µV

Table 4.1. Listing of parameters used in mass flow and uncertainty calculations.

$$\frac{1}{A_{throat}} - \frac{1}{A_{inlet}} = \frac{2 * \rho_{liq} * Signal}{Slope * \dot{m}^2} \tag{4.1}$$

$$\frac{1}{A_{throat}} - \frac{1}{A_{inlet}} = \frac{2 * \rho_{liq} * (Signal +/- Standard\ Deviation)}{Slope * \dot{m}_{upper/lower}{}^2} \tag{4.2}$$

$$\frac{1}{A_{throat}} - \frac{1}{A_{inlet}} = \frac{2 * \rho_{liq} * (Signal +/- Signal\ Uncertainty)}{Slope * \dot{m}_{upper/lower}{}^2} \tag{4.3}$$

$$Mass\ Error_{upper} = \dot{m}_{upper} - \dot{m} \tag{4.4}$$

$$Mass\ Error_{lower} = \dot{m} - \dot{m}_{lower} \tag{4.5}$$

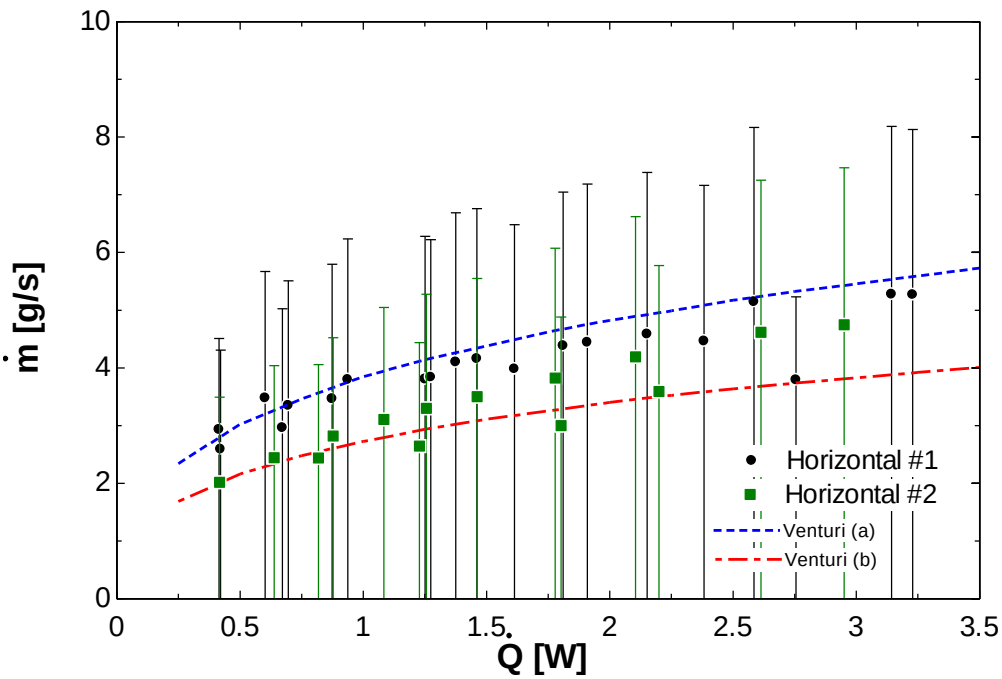

Figure 4.4a. Average mass flow rate as a function of horizontal heat load for single channel test. Error bars are derived from equation (4.2).

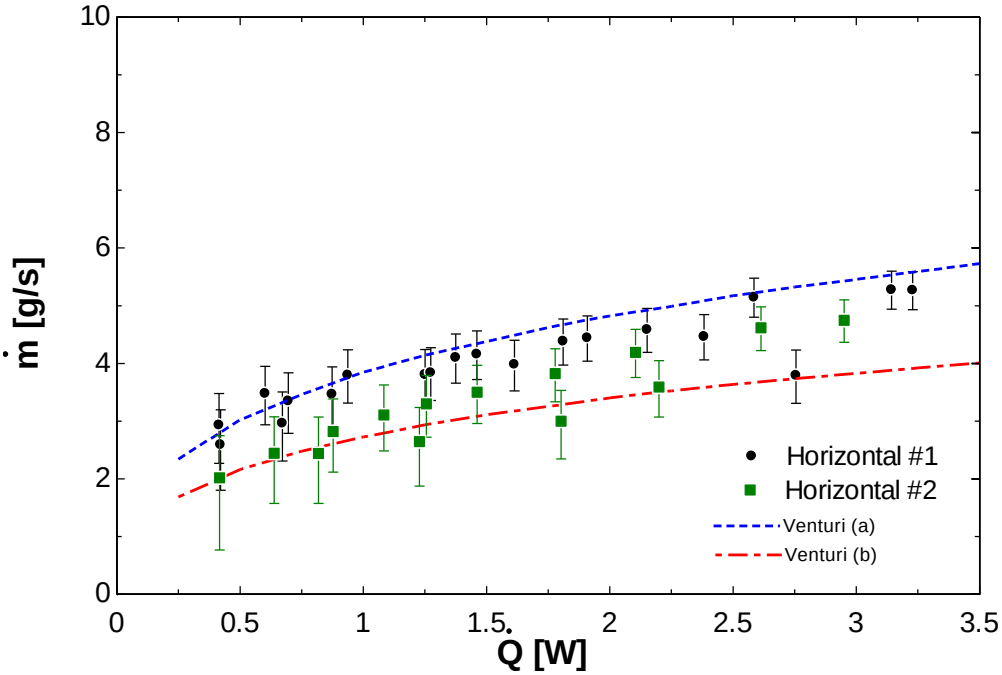

Figure 4.4b. Average mass flow rate as a function of horizontal heat load for single channel test. Error bars are derived from equation (4.3).

On the average, the observed mass flow rates agree with the modeled predictions that include the minor losses and the losses associated with the Venturi. The signal fluctuations, however, are significantly larger than expected. A comparison between the data gathered from the tests using the horizontal heater with that collected from the tests using the vertical heater are illuminating. As shown in FIGURES 4.5a and 4.5b, the data gathered when the vertical heater was used agree with those from the horizontal heating in terms of the average mass flow rate. Note however, that the signal fluctuations are significantly reduced. As a result, the fluctuations associated with the data in FIGURE 4.4a are attributed to a density wave-like instability and not a measurement error. The same feature is evident in the direct comparison of FIGURES 4.2 and 4.3.

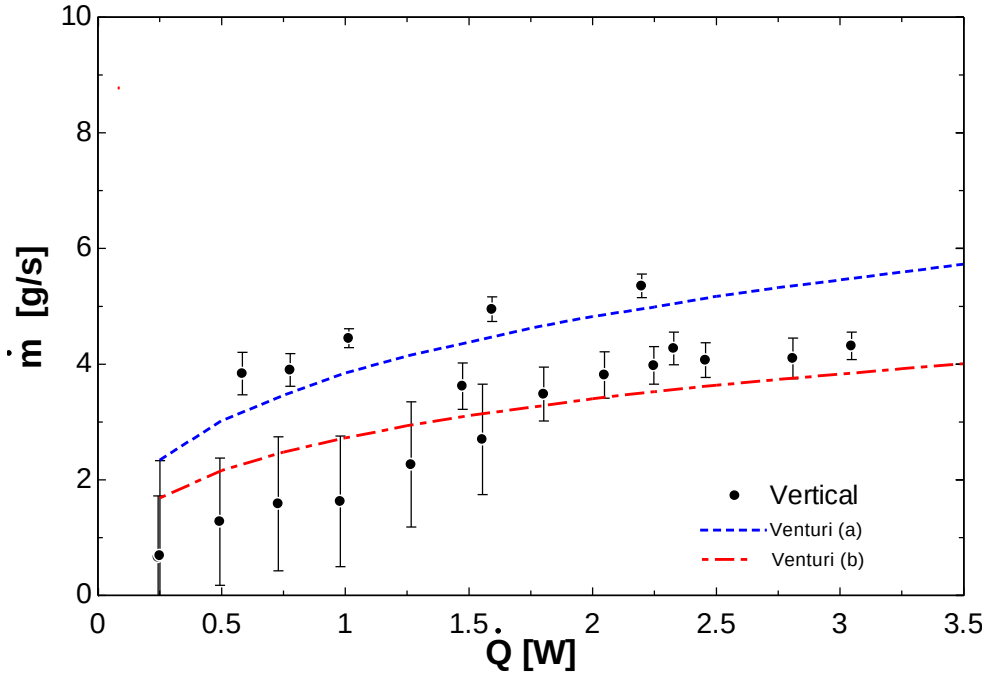

Figure 4.5a. Average mass flow rate as a function of vertical heat load for single channel test. Error bars are derived from equation (4.2).

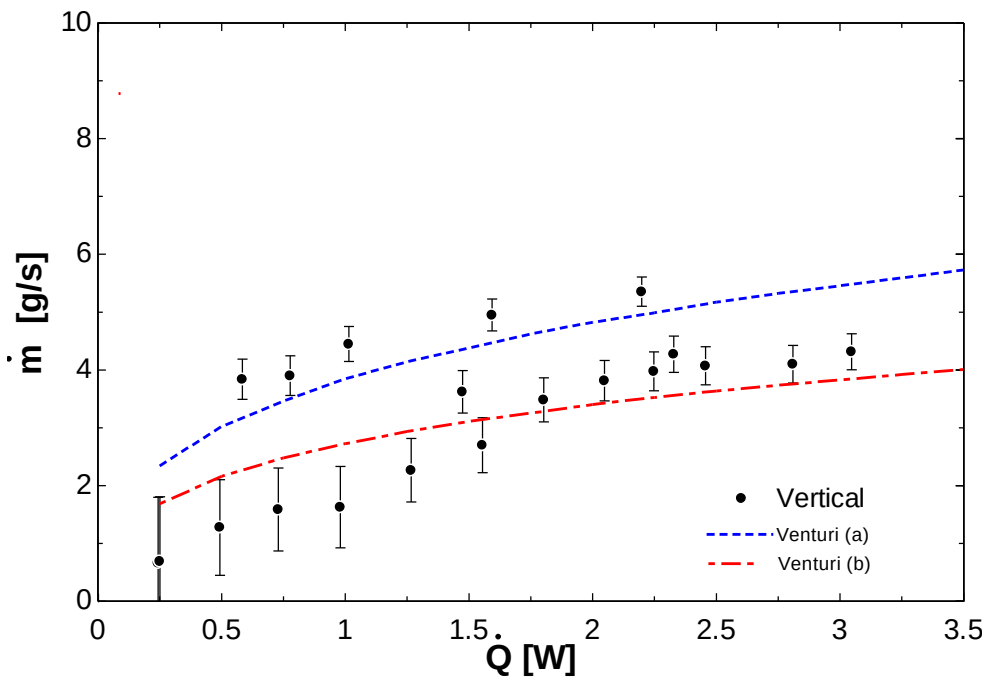

Figure 4.5b. Average mass flow rate as a function of vertical heat load for single channel test. Error bars are derived from equation (4.3).

To further characterize the transient fluctuations in the mass flow rate, a weighted standard deviation variable is introduced called the coefficient of variation (COV)

$$Coefficient\ of\ Variation = 100 * \frac{Standard\ Deviation}{Signal} \tag{4.4}$$

The primary importance of the COV is in the comparison of magnitudes among different heating applications. Because the signal increases as a function of heat load, the expected response of the COV should behave like an inverse power law and decay as more heat is applied given a consistent signal deviation. FIGURES 4.6 and 4.7 display the COV as a function of applied heat load and reveal the significant difference in mass flow behavior horizontal and vertical heating. . The several data points of vertical heating in FIGURE 4.7 that are inconsistently large can be attributed to the outlying average mass flow rates observed in those runs, driving up the COV.

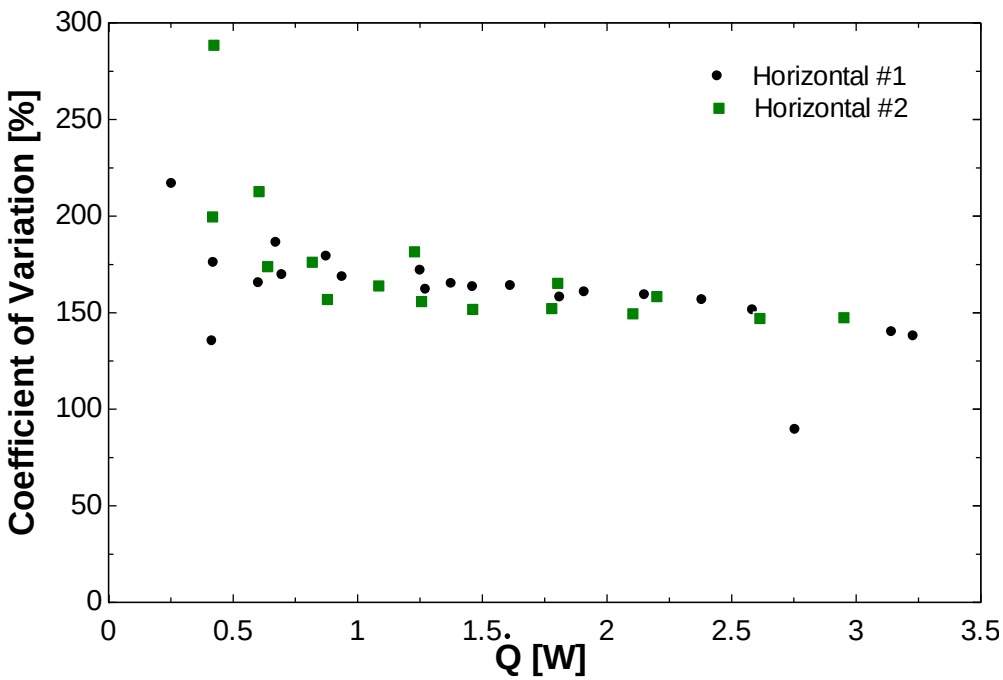

Figure 4.6. Coefficient of variation as a function of horizontal heat load for the single channel test.

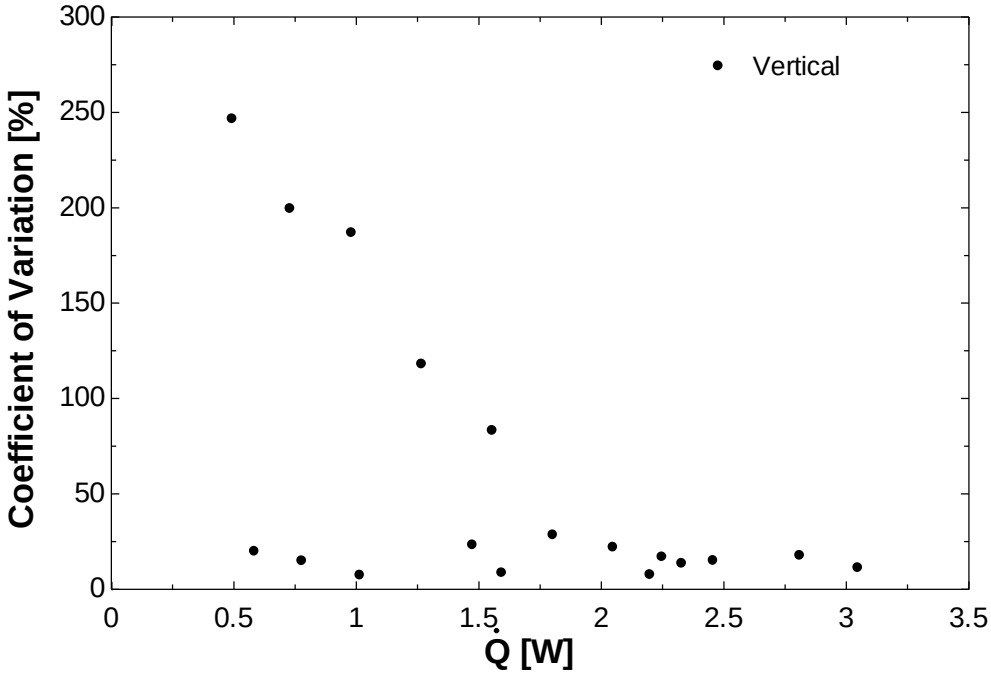

Figure 4.7. Coefficient of variation as a function of vertical heat load for the single channel test.

4.3 Core Geometry Orientation 1 Results

After confirming that the thermosiphon operates as predicted using the single channel configuration, the three-channel geometry anticipated for the superconducting undulator core was tested. The first orientation mimics the top magnet as shown in FIGURE 4.1a. To determine the potential impact of the return stand pipe, tests were run with the reservoir's liquid level both above and below it.

FIGURE 4.8 displays the average mass flow rate as a function of horizontal heat load, with the error bars displaying the variation of the flow rate characterized by equation (4.2). Shown in FIGURE 4.9 is the coefficient of variation. As in the single channel test, the average flow rate follows the thermodynamic model but the rate varies widely in time. The behavior is interpreted as a result of vapor formed in the horizontal channel that stratifies to the top of the channels and coalesces. As the resulting plugs of vapor are released and reformed, the liquid rapidly accelerates and stagnates intermittently.

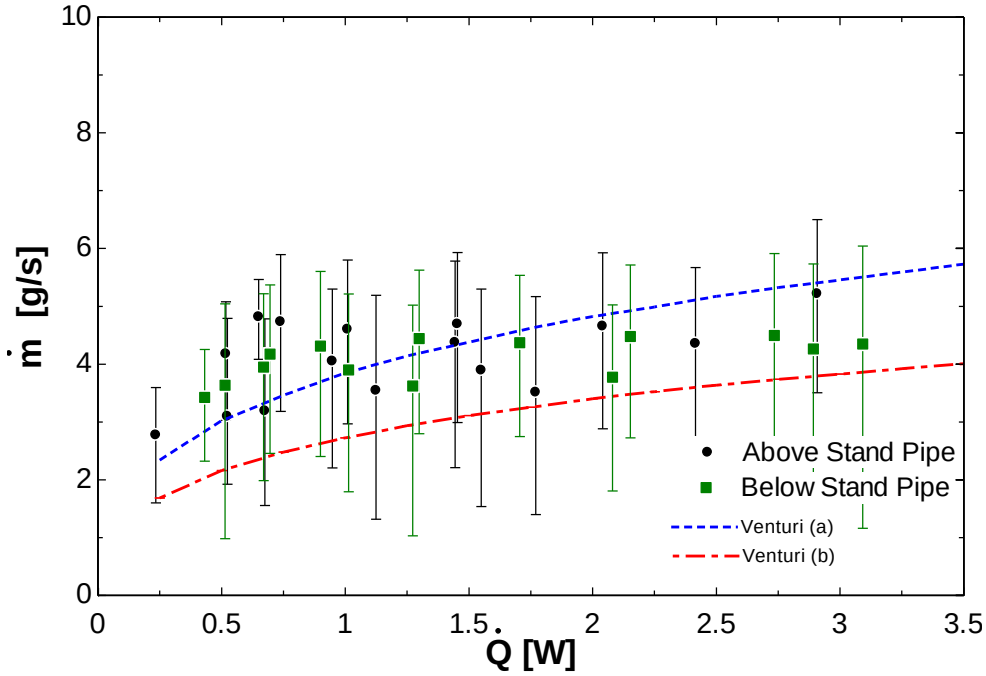

Figure 4.8. Average mass flow rate as a function of horizontal heat load for three-channel test #1. Error bars are derived from equation (4.2).

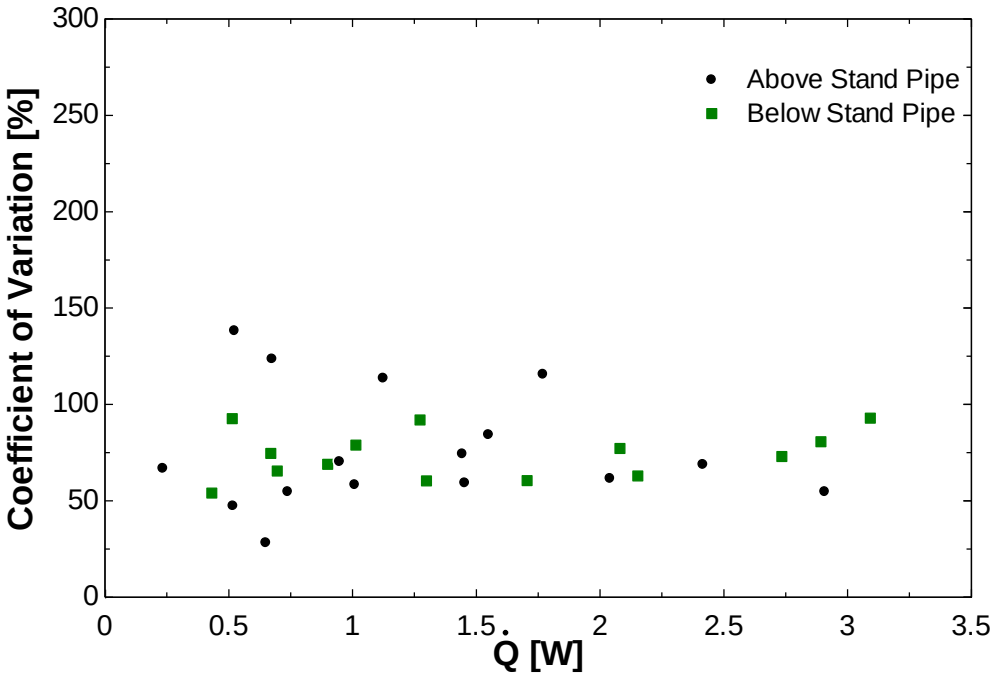

Figure 4.9. Coefficient of variation as a function of horizontal heat load for three-channel test #1.

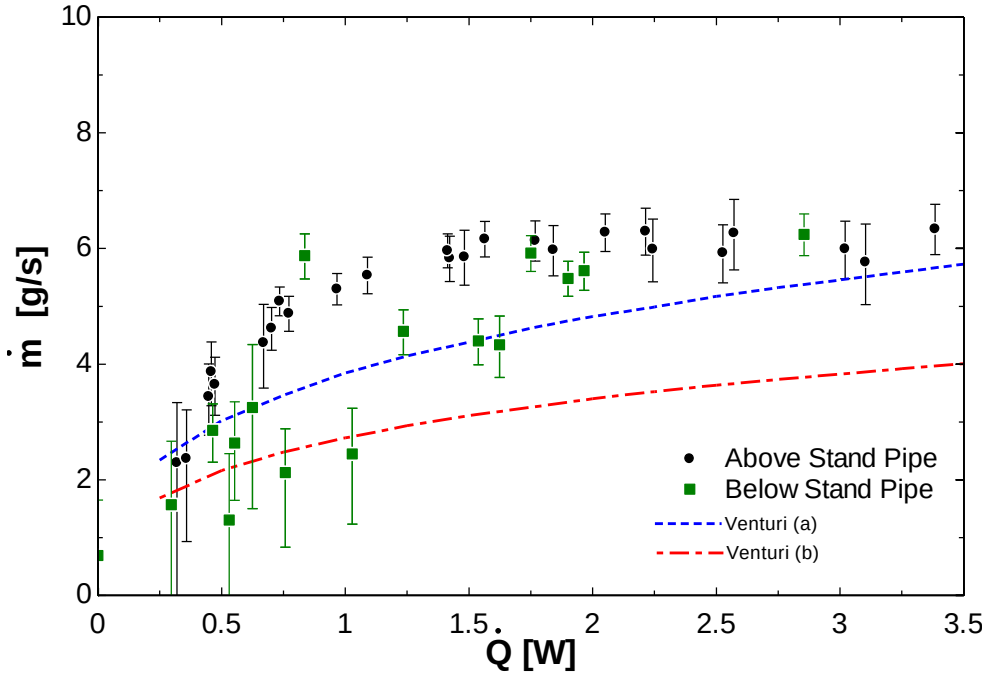

Figure 4.10. Average mass flow rate as a function of vertical heat load for three-channel test #1. Error bars are derived from equation (4.2).

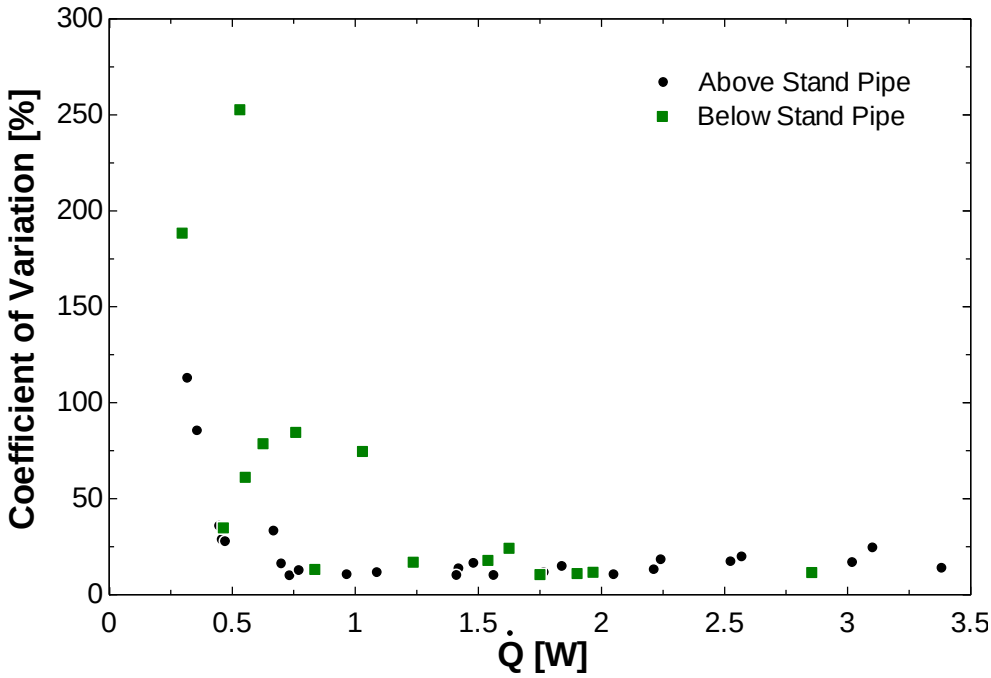

Figure 4.11. Coefficient of variation as a function of vertical heat load for three-channel test #1.

As before, the data from the vertical heating mode compare quite favorably with the predicted flow rate and display a reduced transient variation, as seen in FIGURES 4.10 and 4.11. A key observation from this test is that the liquid level height relative to the stand pipe has a significant impact. When the liquid level is above the stand pipe, the flow rates above 0.5 W are stable and the relationship follows a smooth trend. If the liquid level is below the stand pipe, the response is more variable.

Recognizing that "clean" flow rates result from vertical heating and "unstable" flow rates from horizontal heating, measurements were then taken to determine how well a horizontally heated system could be regulated with a vertical heater. FIGURE 4.12 shows the results as a function of the total heat load and include the observed signal variations (as defined by equation (4.3)). FIGURE 4.13 displays the COV as a function of the total heat load. These data also confirm that the stand pipe location impacts the stability of the signal. FIGURE 4.14 presents the same COV data, but with respect to the power ratio (vertical to horizontal). Note the small amount of heat required on the vertical leg in order to produce stable flow even with the liquid level above the stand pipe.

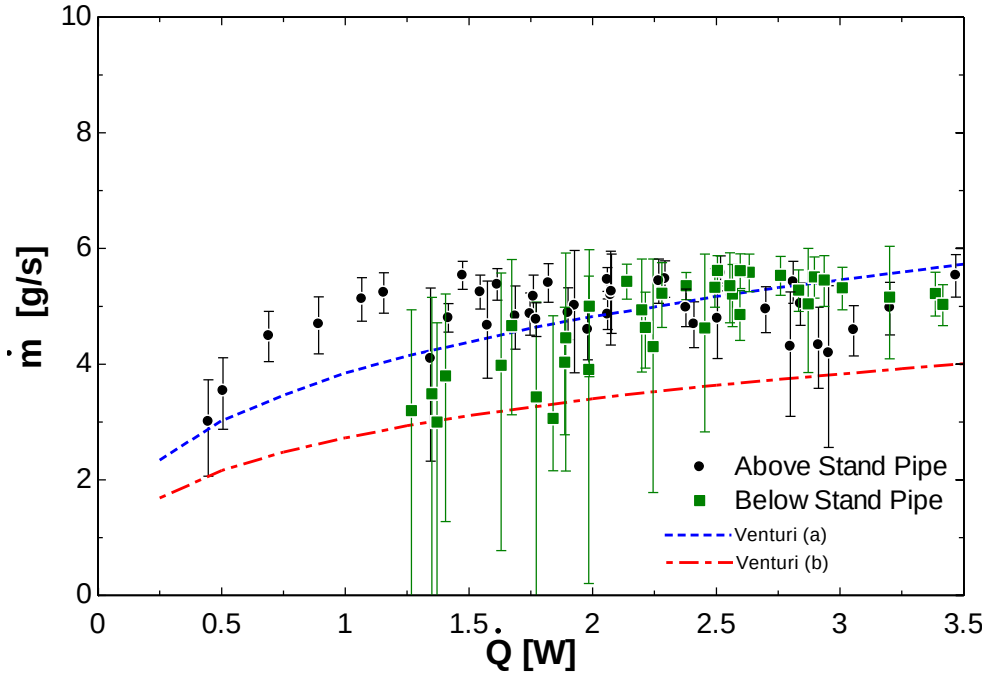

Figure 4.12. Average mass flow rate as a function of combined heat load for three-channel test #1. Error bars are derived from equation (4.2).

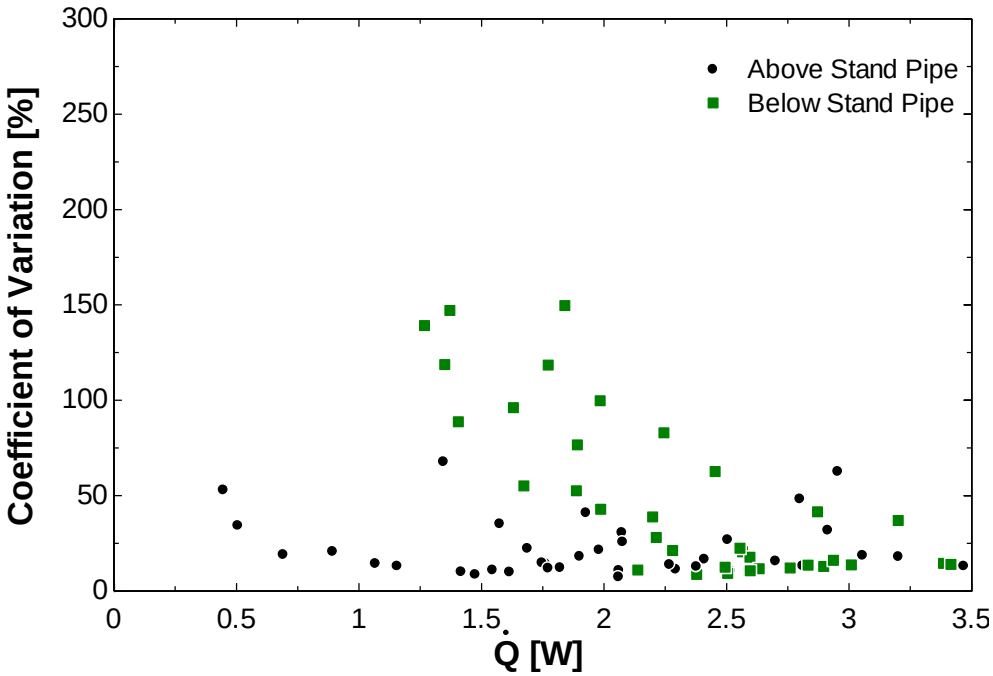

Figure 4.13. Coefficient of variation as a function of combined heat load for three-channel test #1.

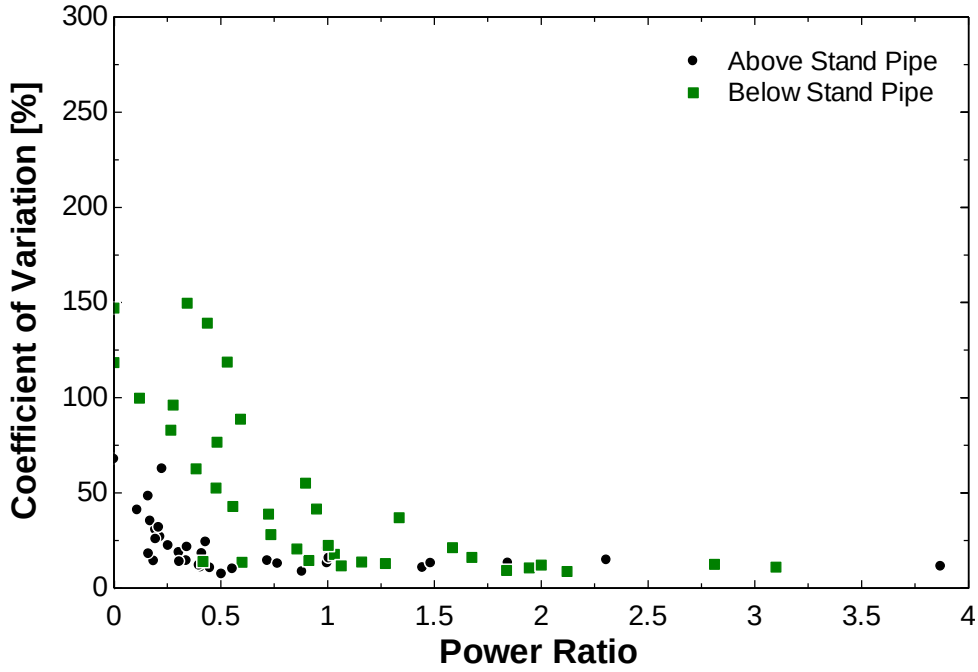

Figure 4.14. Coefficient of variation as a function of power ratio (vertical/horizontal) for three-channel test #1.

4.4 Core Geometry Orientation 2 Results

The cooling geometry associated with the lower superconducting undulator core was then tested in the same manner as the upper core geometry (see FIGURE 4.1b). The results from the horizontal heating mode shown in FIGURES 4.15 and 4.16 compare quite favorably with the other horizontal heating tests. The large increase in the COV from FIGURE 4.9 to 4.16 may be attributed to additional vapor accumulation in the raised side channels.

Data gathered from the vertical heating mode and shown in FIGURE 4.17 follow the same trend shown in FIGURES 4.5a and 4.10. When the liquid level is above the stand pipe, the flow rates reach a stable operating condition for relatively low values of applied heat. The coefficient of variation is shown in FIGURE 4.18 is very similar to that shown in FIGURE 4.1, especially in terms of relative reservoir liquid level with respect to the stand pipe.

A combined heating test was also conducted for this three-channel configuration. As in FIGURES 4.13 and 4.14, FIGURES 4.20 and 4.21 show that the flow variation can be regulated by vertical heating.

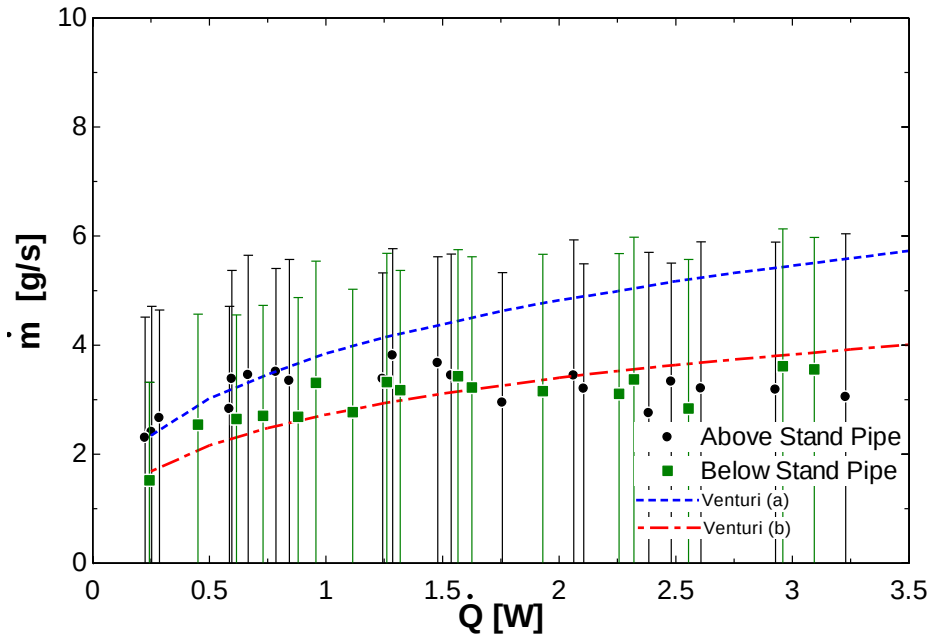

Figure 4.15. Average mass flow rate as a function of horizontal heat load for three-channel test #2. Error bars are derived from equation (4.2).

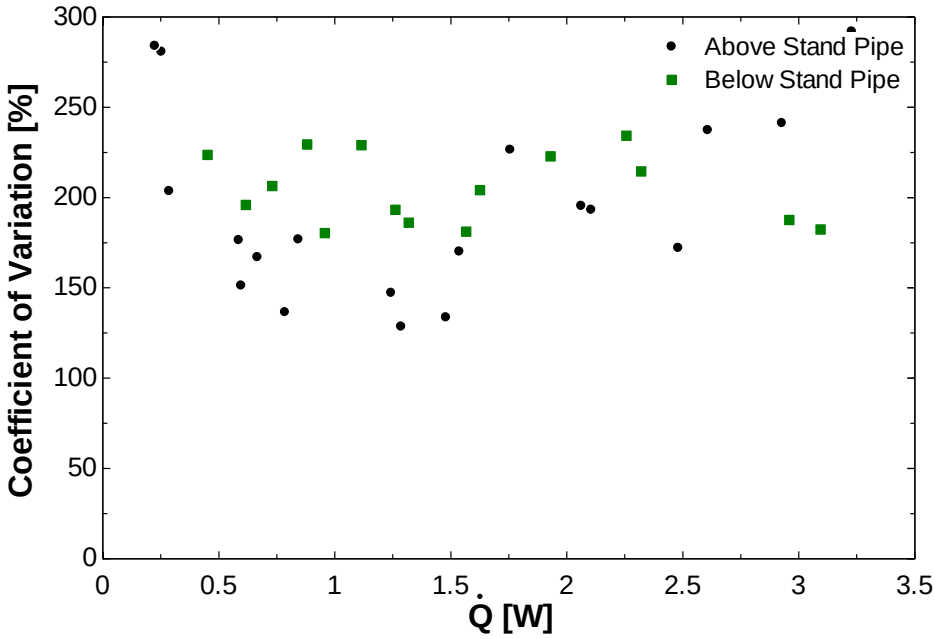

Figure 4.16. Coefficient of variation as a function of horizontal heat load for three-channel test #2.

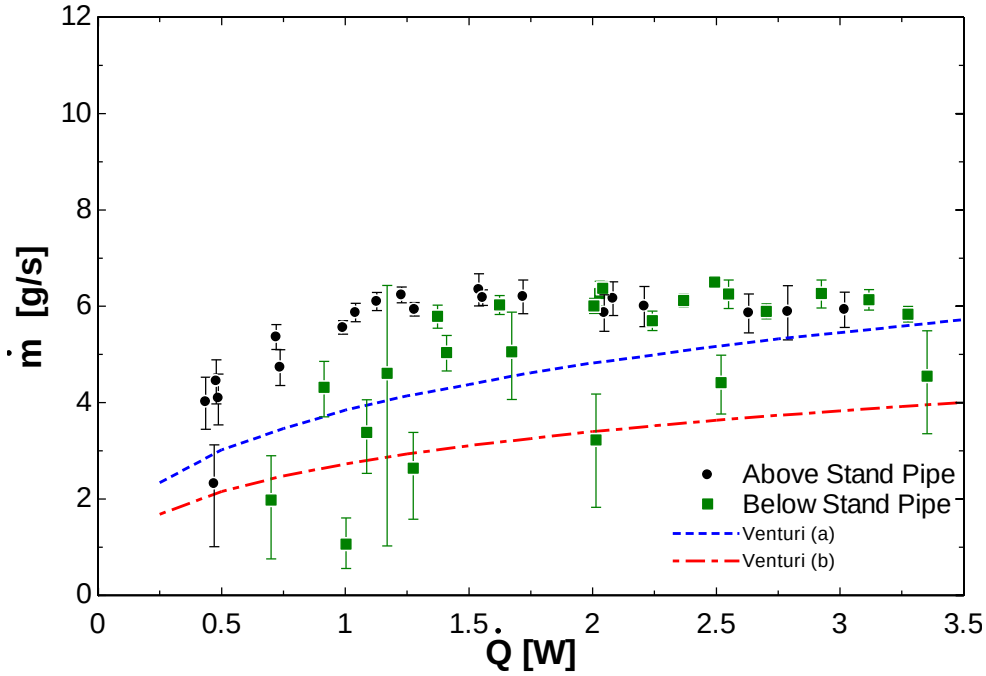

Figure 4.17. Average mass flow rate as a function of vertical heat load for three-channel test #2. Error bars are derived from equation (4.2).

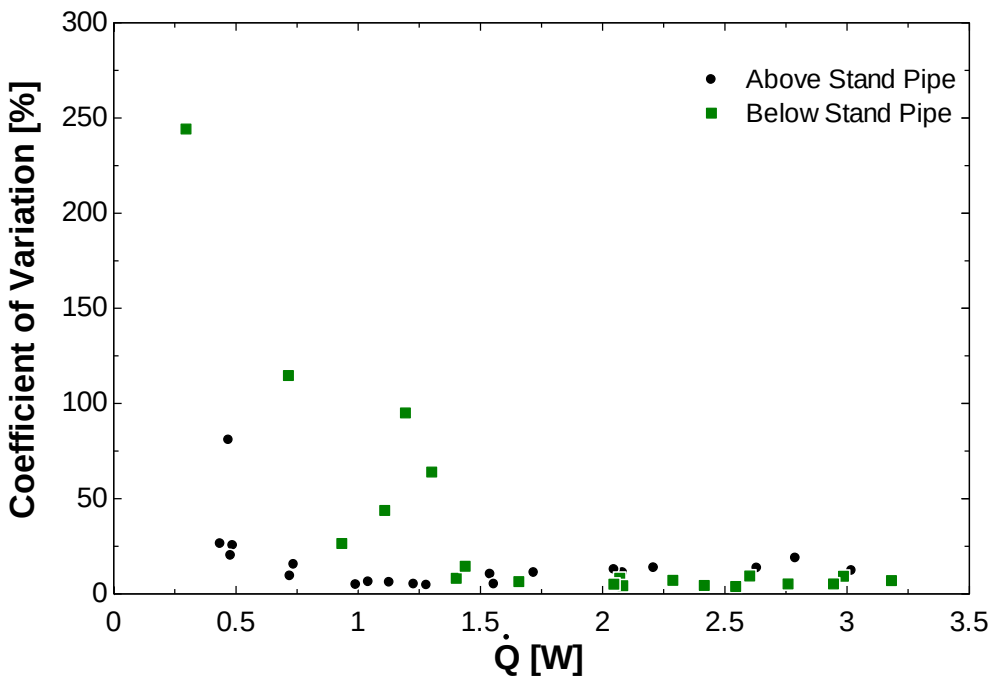

Figure 4.18. Coefficient of variation as a function of vertical heat load for three-channel test #2.

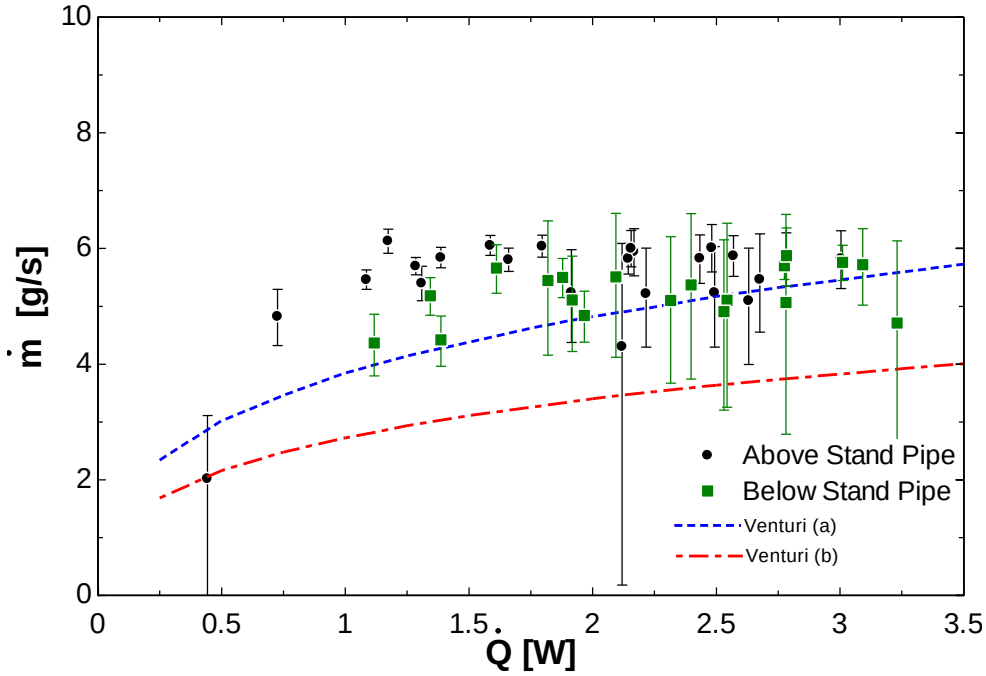

Figure 4.19. Average mass flow rate as a function of combined heat load for three-channel test #2. Error bars are derived from equation (4.2).

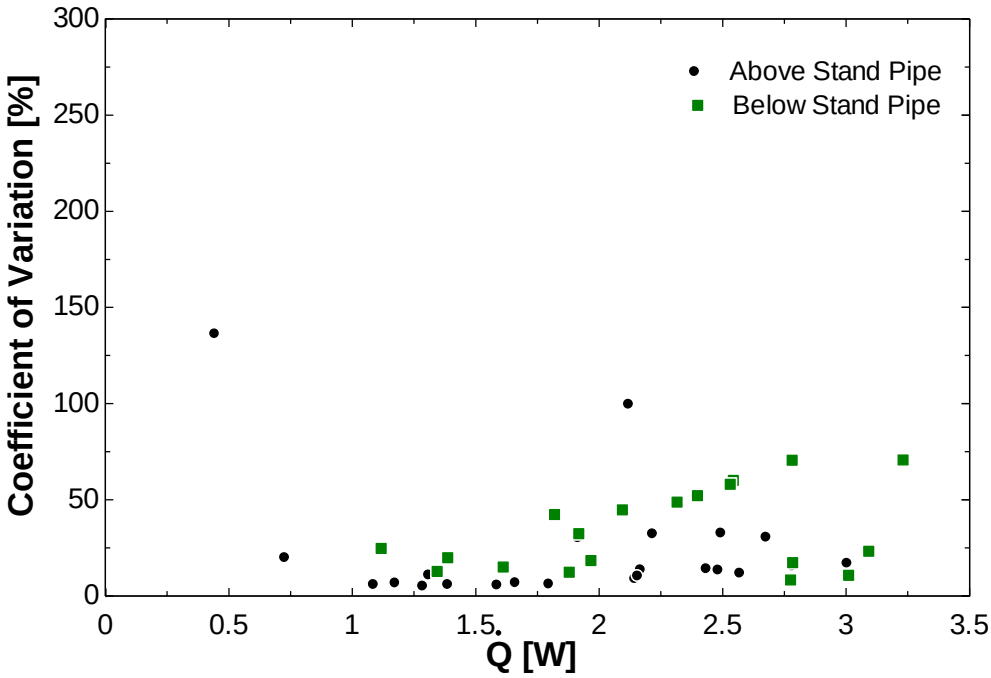

Figure 4.20. Coefficient of variation as a function of combined heat load for three-channel test #2.

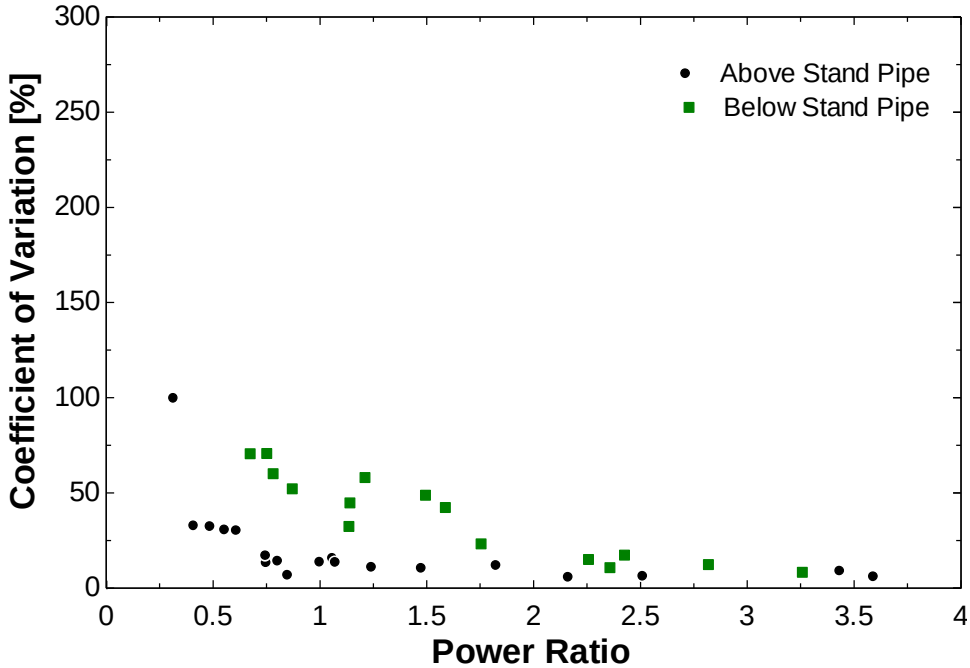

Figure 4.21. Coefficient of variation as a function of power ratio (vertical/horizontal) for three-channel test #2.

4.5 Discussion and Recommendations

On the average, the horizontal and vertical heating results behave as expected. The confirmed behavior is particularly important given the low quality (<5%) that provides the driving force. The data confirm operation of a thermosiphon on a scale not presented in other studies. However, all three tests exhibit an irregular release of vapor when heat is applied along the horizontal section. Beyond identifying that the behavior is likely a result of stratified flow, it is significant to note that the intermittent flow may result in similarly transient heat transfer characteristics. The fact that the signal variation is quite a bit larger for the bottom core's geometry than the top core's suggests a larger accumulation of vapor layer because of the different piping arrangement (see FIGURE 4.16 vs. FIGURE 4.9). In and of itself this is not too grave of a concern for the SCU cores due to the parallel heat conduction paths that the steel core offers as an alternative to the gas layer, but it does increase the density-wave instability. Adding heat along the vertical return section almost entirely eliminates the unstable flow, with only a

slight geyser-like instability observed, and that depending on the liquid level in the reservoir relative to the exit of the stand pipe. The most important observations, however, come from the combined loading tests described in sections 4.3 and 4.4. These provide two key design considerations for the superconducting undulator cryostat:

1. Flow can be regulated by applying heat to the vertical return piping.
2. The flow rates are more stable when the liquid level in the reservoir is maintained above the stand pipe. The same stable flow rates could be expected in the absence of a stand pipe.

The impact of the stand pipe on flow stability is somewhat surprising. The data suggest that the heat applied along the horizontal section still causes a density wave instability from coalesced vapor, but its exit from the horizontal section does not amplify its impact – instead its presence in the vertical section does. A plausible scenario for the observed behavior is as follows: when the liquid level is above the stand pipe, the slugs of vapor break the surface of the entire helium reservoir and their impact is distributed and minimal. However, when the liquid level is below the stand pipe, the density wave presents itself as a geyser instability, and the large segment of vapor breaking the surface of the restricted tube area causes a back-pressure during the time that the vapor breaks the surface. The instability, then, is a coupled instability – not quite a density wave and not quite a geyser – since it is generated in the horizontal section but shows itself in the vertical piping. The flow behaves like a percolating coffee maker with heat coming from the horizontally orientated hot plate and intermittently sending plugs of liquid up to the coffee grounds when the vapor tries to breaks the surface.

Although the anticipated horizontal heat load for the superconducting undulator, taking into account radiation and conduction, is only ~0.75 W, heat generation from the beam is not

well characterized [1]. Despite the fact that the system design will provide up to 3 W of available recondensing power, the associated efficiency of re-liquefying the vapor is not well known and is currently under investigation. Nevertheless, by maintaining the liquid level above the return stand pipe or placing holes in the piping to limit the "percolation" effects, a thermosiphon operating in the tested configuration with only a single 1.5 W cryocooler for recondensing would be sufficient to provide a stable mass flow rate, assuming a power ratio of as little as 0.25. If the re-liquefaction process is effective, it is possible that the SCU cryostat will have a safety margin greater than 2.

4.6 References

1. Petra, M. and Kustom, B., "Sources of Dynamic Heat Load for the Superconducting Undulator," internal APS note, November 2004.
2. Potratz, D., "Updated FEA Model for SCU0," APS-MD presenation, March 8, 2011.

5 SCU Operation and Considerations

5.1 Anticipated SCU Flow Rate

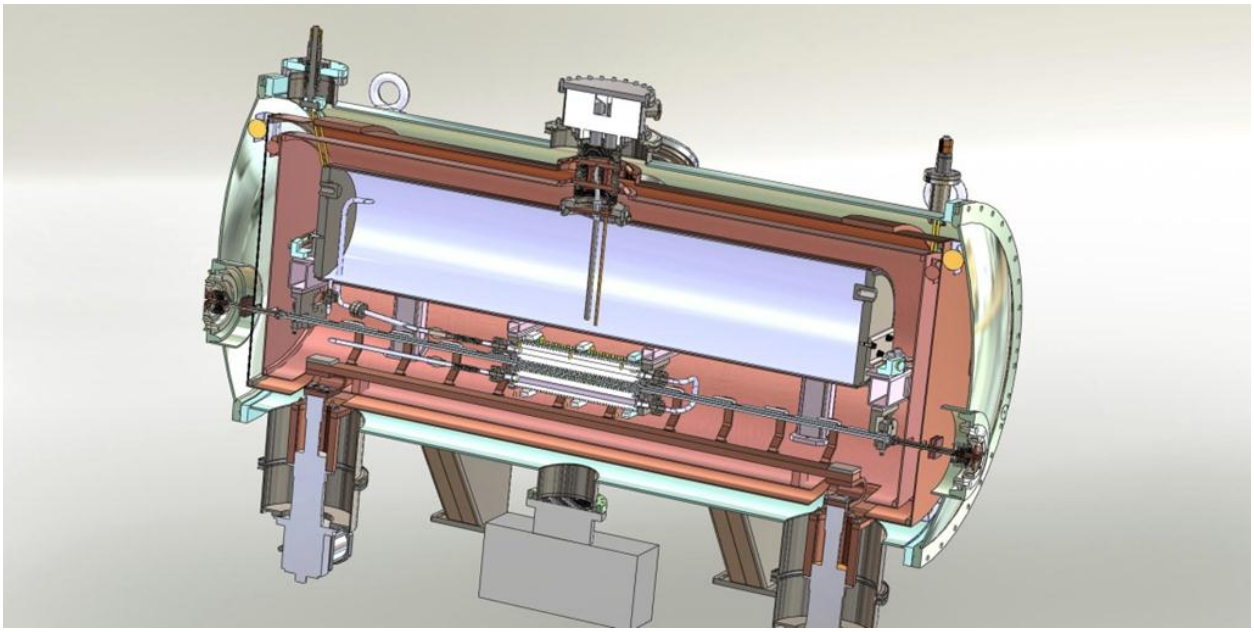

Figure 5.1. Superconducting undulator cryostat with 42-pole cores.

It is possible to predict the mass flow rate for the superconducting undulator now that the thermosiphon model developed in chapter 2 has been confirmed by the results in chapter 4. As shown in FIGURE 5.1, the SCU cooling loop comes down from the helium vessel, travels through the bottom magnet core, bends around the beam chamber, goes through the top magnet core, and then returns to the reservoir. The mass flow rate of the helium inside the magnets is presented in FIGURE 5.2 as a function of total heat load to both cores. Minor losses from the bends going around the beam chamber and due to the expansion and contraction of the plenums dominate the flow as expected, but it nevertheless remains turbulent. The anticipated heat transfer coefficient varies from 71 to 77 W/m^2-K over a range of 1.5 to 2.5 W (see FIGURE 5.3) and results in a conservative and consistent estimate that can be used for sub-modeling studies.

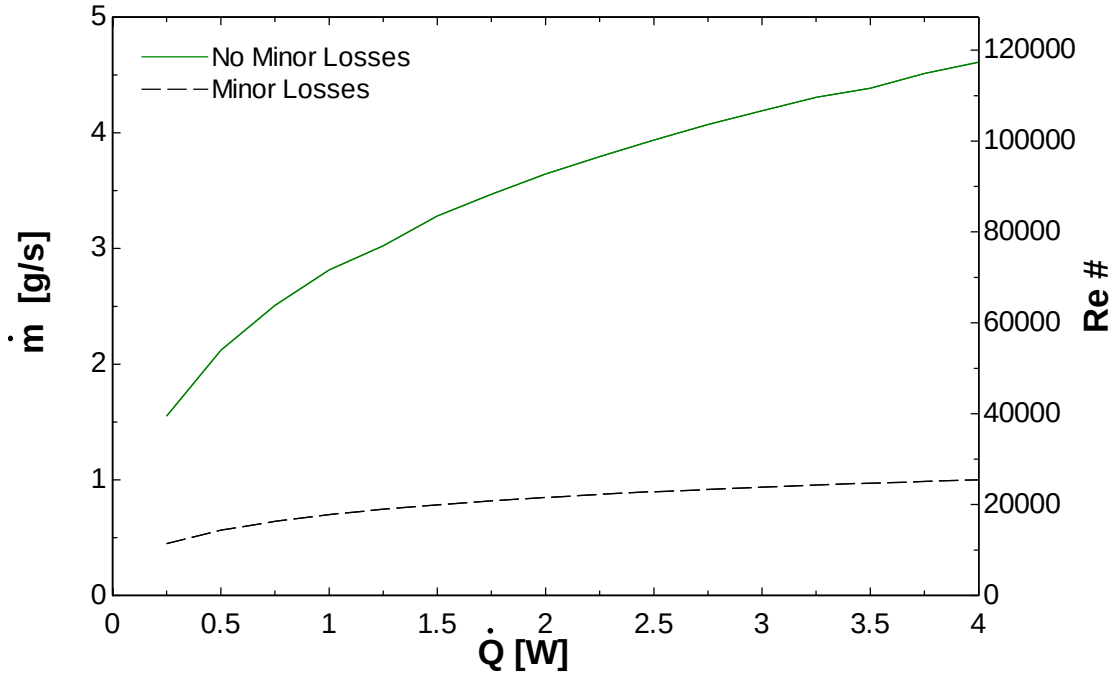

Figure 5.2. Anticipated flow rate inside the undulator cores as a function of total thermosiphon heat load.

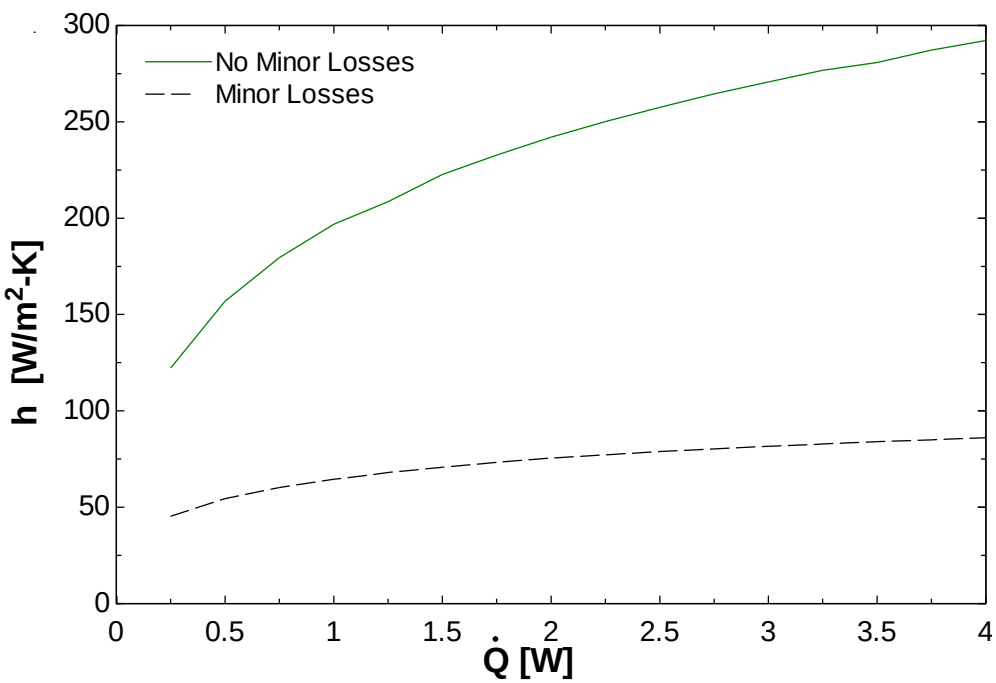

Figure 5.3. Anticipated heat transfer coefficient as a function of total thermosiphon heat load.

The minor losses severely impede additional heat application from increasing the heat transfer characteristics of the thermosiphon loop. Size constraints from the APS tunnel limit the height of the hydrostatic head, but as was shown earlier in FIGURE 2.7 an optimized system performs better with a lower head height. Outside of eliminating as many minor losses as possible (by limiting bends and rounding all sharp edged inlets and exits), the channel diameter remains the final independent variable in increasing the flow rate. Since the convective heat transfer is dependent on the area over which it occurs (equation (5.1)), simply decreasing the diameter of the channels would limit the effectiveness of the heat transfer. However, reducing the hydraulic diameter of the flow channel by inserting a rod in the channels in order to create an annular flow path would maintain the same wetted perimeter while increasing the flow rate and heat transfer coefficient inside of the cores. FIGURE 5.4 displays a suggested method to insert a rod into the core. This approach would only be limited in manufacturability when the plenums are welded into place. FIGURE 5.5 shows the anticipated mass flow rate inside the cores as a function of hydraulic diameter and FIGURE 5.6 displays the anticipated heat transfer coefficient using the method developed in section 2.3 (the quality remains below 6%).

$$\dot{Q} = h * A_s * \Delta T \tag{5.1}$$

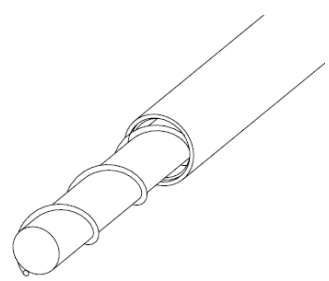

Figure 5.4. Method to create annular channels using a wound coil as a spacer.

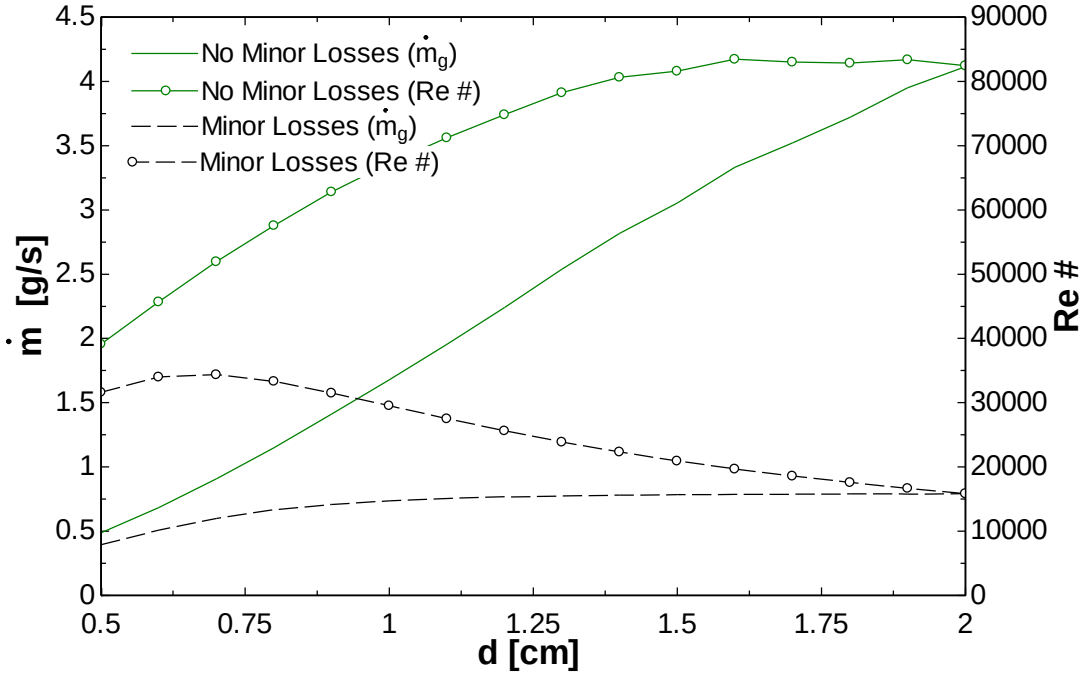

Figure 5.5. Anticipated mass flow rate in the undulator cores as a function of hydraulic diameter for a constant heat load of 1.5 W.

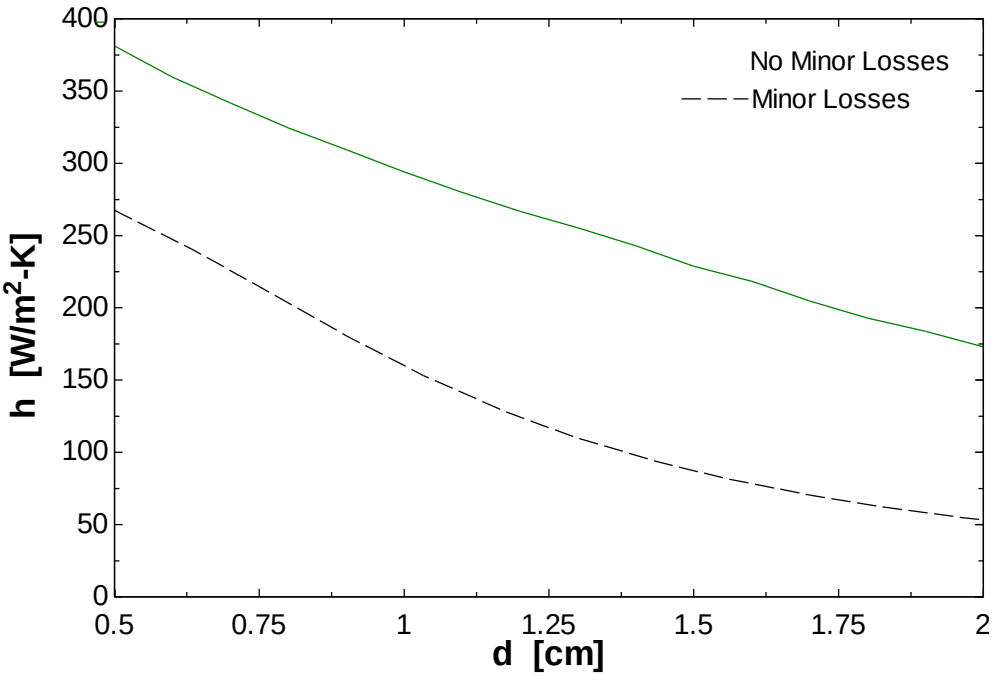

Figure 5.6. Anticipated heat transfer coefficient in the undulator cores as a function of hydraulic diameter for a constant heat load of 1.5 W.

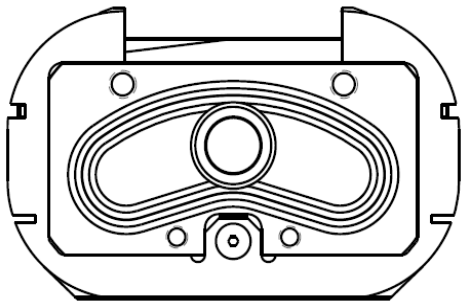

Figure 5.7a. Top core end-view.

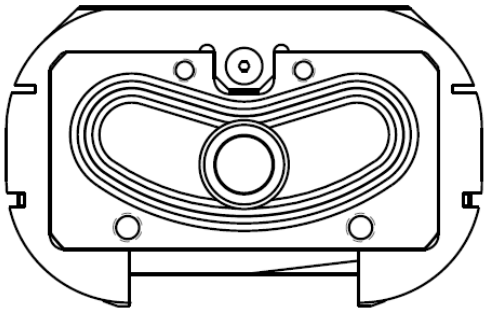

Figure 5.7b. Bottom core end-view.

If the annular channel method is developed, it would be beneficial to adjust the inlet and exit piping location on the bottom cores plenum to eliminate the elevated side channels (see FIGURES 5.7a and 5.7b). With a reduced hydraulic diameter the instability observed with horizontal heating would likely be amplified and the behavior harder to predict.

An additional design suggestion identifies a benefit of producing a preferential flow in the thermosiphon. In the existing designs, the flow channels have to be perfectly horizontal from a manufacturing perspective. However, if the channels could be machined at a 5° incline, the horizontal instability would be greatly reduced by the preferential flow.

5.2 Thermal Conductivity of the Core

The thermal conductivity of the 1006-1008 low carbon steel used for the SCU core also impacts the operating temperature of the superconducting windings. Carbon steel is not often used at cryogenic temperatures due to carbon embrittlement. However, it has been selected in this case as the core material for its slight flux contribution to the magnetic field. There are no studies available to predict the thermal conductivity of the steel at liquid helium temperatures, so a thermal conductivity test was performed at the University of Wisconsin-Madison cryogenics lab.

5.2.1 Experimental Description and Test Procedure

The thermal conductivity test rig consists of four primary components: a Janis ST refrigerator, a heater block attached to one end of the test sample, two temperature sensors, and the data acquisition system. A schematic presenting the assembly wiring and sample position is seen in FIGURE 5.8 with a picture provided in FIGURE 5.9.

The Janis ST refrigerator operates by circulating liquid helium through a cold finger inside a vacuum vessel. A copper shield screws into the top of the cold head where the instrumentation lines are fed through and surrounds the test sample. The shield is covered in ~15 layers of MLI. The cold finger of the Janis refrigerator reaches ~4.2 K in approximately 20 minutes. The cylindrical sample (OD = 12.7 mm, ID = 10.16 mm, length = 63.5 mm) is mounted to the cold finger by placing a small amount of Apiezon N grease on its top end and sliding it over a threaded G10 mounting post (diameter = 5.1 mm). Care is taking to make sure the sample does not contact the G10 post, and the heater block, followed by a washer-spring-nut assembly, is threaded onto the bottom end of the test fixture and tightened until the spring is fully compressed.

The copper heater block is placed on the bottom of the sample with its power supplied by a TENMA 72-2005 power supply (18 V/3 A output). A 10 Ω wire heater is wrapped and secured into place with GE varnish around its outside. Both voltage and current measurements are gathered using four wire measurements for increased accuracy.

Two Cernox temperature sensors (+/- 60 mK observed agreement) are mounted 57.15 mm apart on the cylindrical test sample. They are attached directly to the test sample with Apiezon N grease and thin G10 brackets that make point contact with both the sensor and the sample. The temperature of the top sensor (TE 01 in FIGURE 5.8) is measured by a Lakeshore

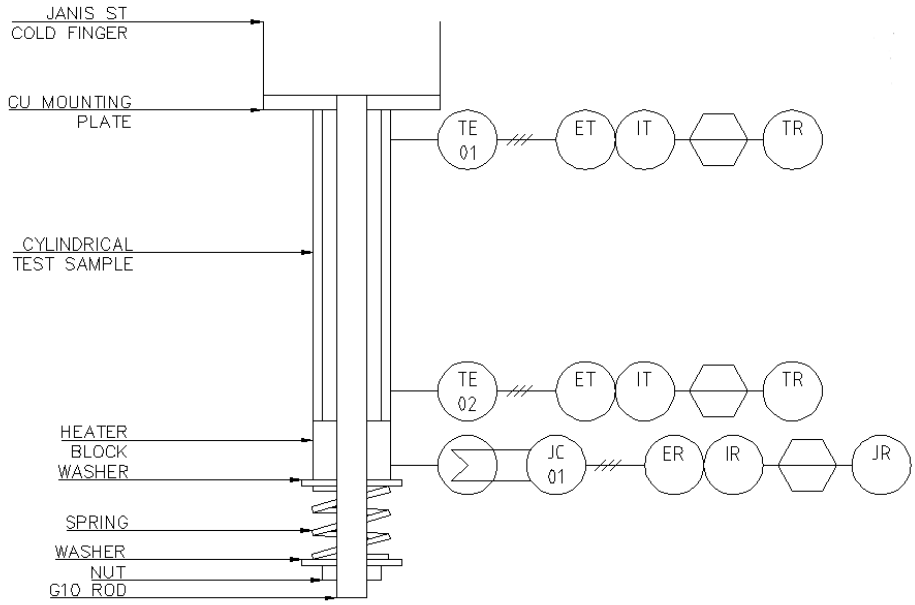

Figure 5.8. Thermal conductivity test schematic.

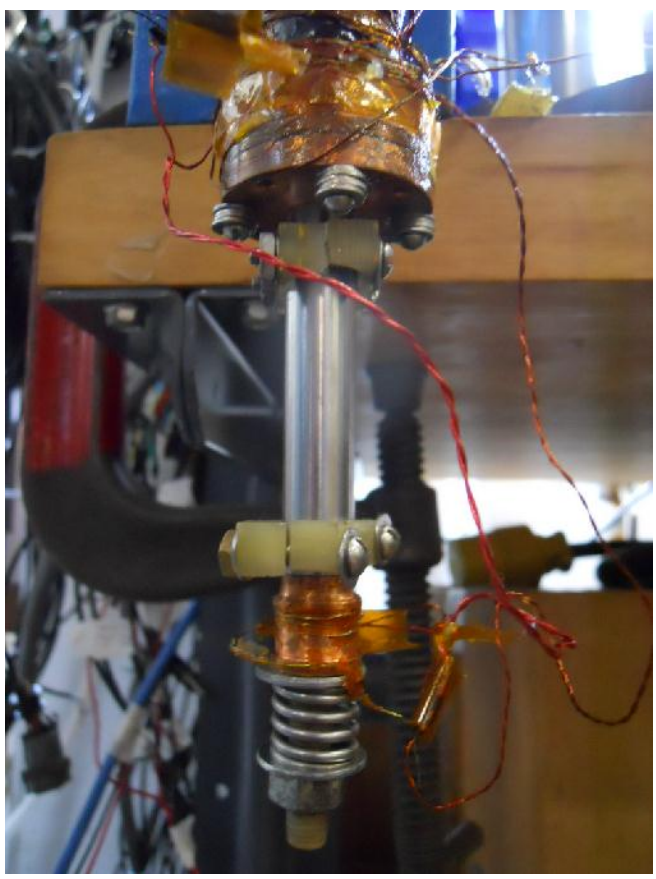

Figure 5.9. Thermal conductivity test rig assembled.

Temperature Controller – Model 332. The bottom temperature sensor (TE 02 in FIGURE 5.8) is connected directly into the data acquisition system using a four wire configuration (two for voltage, two for current). A variable current source (Lakeshore Model 120) provides a precision DC current to the temperature element. Knowing this current value and measuring the voltage, the resistivity of the Cernox sensor can be calculated and corresponded to a temperature. To determine the combined uncertainty due to this method of measurement, equation 5.2 is solved

$$U_T = \sqrt{(U_V * T)^2 + (U_I * T)^2 + U_A^2} \tag{5.2}$$

where U_T is the total temperature uncertainty, U_V is the voltage measurement uncertainty (~0.01%), U_I is the current measurement uncertainty (~0.1%), T is the temperature being measured (nominally 10 K for this calculation) and U_A is the accuracy based off of the observed agreement of the Cernox sensors. The total temperature measurement uncertainty is then 67 mK.

The data acquisition system consists of a Dell laptop computer and a NI USB-6009 14-bit DAQ. As TE 01 is read directly off of the Lakeshore 332 controller and the current source to TE 02 is known, the DAQ system records three variables – the sample heater's voltage and current and TE 02's voltage. Narrowing the measurement band to +/- 1 Volt and +/- 1 Amp for the power results in an uncertainty for each measurement of ~0.01%. Using the root sum of the squares, these uncertainties combine to produce an uncertainty in the power measurement of 0.017%. Samples are taken at a rate of 1000 samples/s at a frequency of 100 Hz. Each sample set is averaged together and then recorded.

There are two sources of parasitic heat flow that can affect the thermal conductivity test results: the conduction heat leak through the parallel G10 support post, and external heat loads

from radiation and wiring to the test fixture heating the sample. The conduction heat flow through the G10 will bias the conduction results toward slightly larger values if it is not taken into account. To estimate the effects of the G10 path, perfect contact between the heater, washer, spring, nut and rod is assumed, resulting in a conduction path parallel to that of the test sample. To characterize the possible leak as a percentage of the total applied heat, a comparison of the thermal resistance networks can be made

$$\%Leak = 100 * \frac{R_{steel}}{R_{G10}} \tag{5.3}$$

with

$$R = \frac{L}{k * A_c} \tag{5.4}$$

Both lengths, L, are 63.5 mm. The cross sectional area (A_c) of the G10 piece is 20.3 mm^2 and the cross sectional area of the steel sample is 45.6 mm^2. The conductivity of G10 at 4.2 K is ~0.075 W/m-K. The thermal conductivity of 304 stainless steel at 4.2 K (0.3 W/m-K) is used for an estimate of the sample's conductivity. Then the maximum heat leak through the G10 support rod at 4.2 K is estimated at 11.1% of that flowing through the sample. After collecting the data presented in section 5.2.2 and using the thermal conductivities calculated in the test, the heat leak from the G10 path is less than 5%.

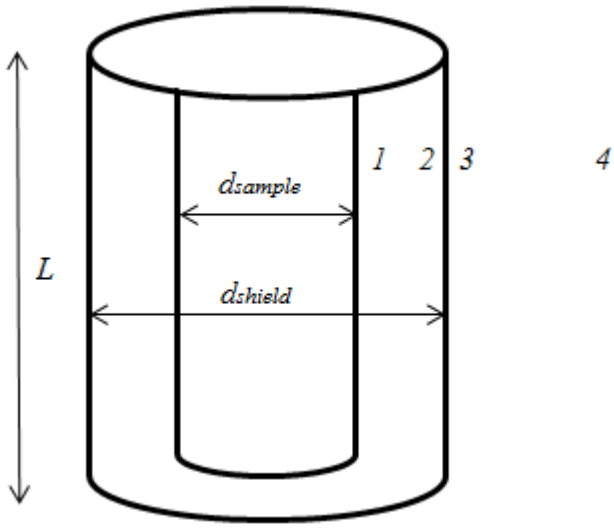

T_1 = 4.2 K, T_4 = 300 K

ε_1 =1, ε_2 =1, ε_3 =0.015[6], ε_4 =1

L = 0.355 m

d_{sample} = 25.4 mm

d_{shield} = 58.4 mm

σ = 5.67E-08 W/m^2-K^4

Figure 5.10. Conductivity test rig radiation model. 1 – cold finger and test sample, 2 – inner radiation shield surface, 3 – MLI surface, 4 – ambient environment.

A simple model has been developed to characterize the impact of thermal radiation on the test rig and the heat load from the shield to the sample temperature. As shown in FIGURE 5.10, the simplified model assumes that the length of the cold finger and test sample at 4.2 K is the same as that of the radiation shield, 0.2 m. Surface 1 only has a view of surface 2 ($F_{1\text{-}2}$ = 1), and by reciprocity surface 2 has a view factor, $F_{2\text{-}1}$, with surface 1 of 0.43.

$$F_{2-1} = F_{1-2} * \frac{A_1}{A_2} \tag{5.5}$$

As surface 2 cannot see surface 3 or 4, its view factor with itself is 0.57. Surface 3 only sees the ambient environment, resulting in $F_{3\text{-}4}$ = 1. The environment, assumed to have a large area, only sees itself, thus – $F_{4\text{-}4}$ = 1. All other view factors are 0. To determine the temperature difference between location 2 and 3 (the outside and inside of the MLI), an energy balance is performed

$$\dot{Q}_3 = \frac{k * A_c}{w}(T_2 - T_3) \tag{5.6}$$

where A_c is the cross sectional area of the shield, 0.065 m^2, w is the width of the MLI blanket, 3.2 mm, and k is the effective conductivity of an MLI blanket under 13 mPa, ~100μW/m-K [7]. The heat coming to surface 3 must equal the heat leaving surface 2

$$-\dot{Q}_2 = \dot{Q}_3 \tag{5.7}$$

Four boundary conditions define the blackbody emissive power

$$E_{b,i} = \sigma * T_i^4 \qquad \text{for } i = 1\ldots4 \tag{5.8}$$

Finally, two concurrently solved radiosity equations are solved

$$\dot{Q}_i = \frac{\varepsilon_i * A_i * (E_{b,i} - J_i)}{1 - \varepsilon_i} \qquad \text{for } i = 1\ldots4 \tag{5.9}$$

$$\dot{Q}_i = A_i * \sum_{j=1}^{4} F_{i,j} * (J_i - J_j) \qquad \text{for } i = 1\ldots4 \tag{5.10}$$

Based on the above equations, the radiation shield temperature calculated at 113 K. Using this shield temperature and assuming two different sample temperatures of 4.2 K and 20 K (the high and low temperatures expected on the sample in this test), and a sample surface area of 2544 mm^2, the total distributed heat load due to radiation can be calculated according to

$$\dot{Q} = A_s * \sigma * (T_{shield}^4 - T_{sample}^4) \tag{5.11}$$

For a sample temperature of 4.2 K, the heating due to radiation on the sample is 23.42 mW. For 20 K the heating is 23.40 mW. The radiation load is relatively small, but more importantly it is the same value (within 0.08%) for both the minimum and maximum anticipated sample temperatures. Thus, it is also essentially constant along the entire length of the sample, given the gradients being explored. With the distributed heat load from thermal radiation being constant and imparting the same heat load (and resultant temperature gradient) throughout the test, its effects can be removed from the test measurements by subtracting the baseline temperature gradients, ΔT_o, on the sample when no heat is applied. Self-heating from the 100 μA power supply to each Cernox sensor is less than 3 μW.

To minimize the parasitic heat load associated with the wires for the two temperature elements and the sample heater, all wires diameters were less than that of a 30 gauge wire, and they all were wrapped numerous times around the cold finger to heat sink any conduction load from ambient.

The cool-down process of the experiment occurs by connecting a liquid helium Dewar to the Janis ST refrigerator transfer line and opening the valve 2-3 turns. The cold finger will reach its steady state operating temperature in ~20 minutes, and the rest of the sample space cools down in ~4.5 hours. To confirm that the test sample is at its steady state condition, the temperature sensor nearest to the heater (TE 02) should remain unchanged for 15 minutes. It is common that TE 01 will read a lower temperature than TE 02 – this is due to radiation (constant as discussed earlier). This heat load is subtracted off of the temperature differences measured

when the test is run to not include its effect. Heat is then applied to the bottom of the sample while the top remains exposed to the ~4.2 K cold finger. After the data reaches steady state (by the temperature sensors reading the same values for 5 minutes) a new heat load is applied.

At low temperatures (4 – 20 K), the thermal conductivity of alloyed metals tend to be linearly dependent on the temperature due to the presence of impurities and overall grain structure [8]. When investigating small temperature differences, a constant value is assumed and thermal conductivities are calculated according to Fourier's Law

$$\dot{Q} = \frac{k * A_c}{\Delta x}(\Delta T - \Delta T_O) \tag{5.12}$$

For this test, the temperature differences being measured are relatively small but still larger than would be accurately defined according to Fourier's Law. The measurements of heat flux vs. temperature difference characterize the average thermal conductivity over the finite temperature difference spanned by the sample length rather than the differential value associated with $\partial Q/\partial T$. As a result, the steel's average thermal conductivity as a function of the average test temperature has been calculated using three different thermal conductivity temperature dependencies – $k = c*T^{0.9}$, $k = c*T^{1}$, and $k = c*T^{1.1}$, as well as assuming it is constant in the range of interest – $k = c*T^{0}$. Test results, displayed in terms of the applied heat to the sample as a function of the temperature difference, are shown in FIGURE 5.11. The steel's average thermal conductivity as a function of the average test temperature is seen in FIGURE 5.12. All three temperature dependent thermal conductivity relationships converge at the low temperature ranges of interest for the SCU cores. For the 1006-1008 carbon steel being tested in this experiment, an approximately linear response is confirmed by FIGURE 5.13, which presents the

temperatures at both locations as each heat load is applied. While the response loses linearity at high end temperatures, at the low temperatures needed to characterize the SCU core operation it is relatively straight.

5.2.2 Conductivity Discussion

At 4.2 K, the measured conductivity is ~0.5 W/m-K, which is slightly better but comparable to the conductivity of 304 stainless steel (~0.3 W/m-K). Preliminary estimates of the conductivity were between 3 and 13 W/m-K (based on data for 1020 carbon steel) [1-3]. The reduced value could be the result of a number of possibilities, including:

1. Higher levels of impurities are present in the steel, decreasing its conductivity.
2. Residual stresses from machining (cold working) or carbon embrittlement at cryogenic temperatures cause dislocations and micro-fractures in the steel, reducing the conductivity. An annealing process following manufacturing could be used to mitigate the effects of cold working.
3. The preliminary estimates were simply wrong. There is a limited amount of thermal conductivity data available for carbon steels in cryogenic environments, and while 1008 carbon steel should have lower impurity scattering than 1020, they are not manufactured in the same way. In fact, 1020 carbon steel is annealed at 870°C while 1008 carbon steel is cold rolled, leading to an increased likelihood that the reduced conductivity is due to cold working rather than impurities.

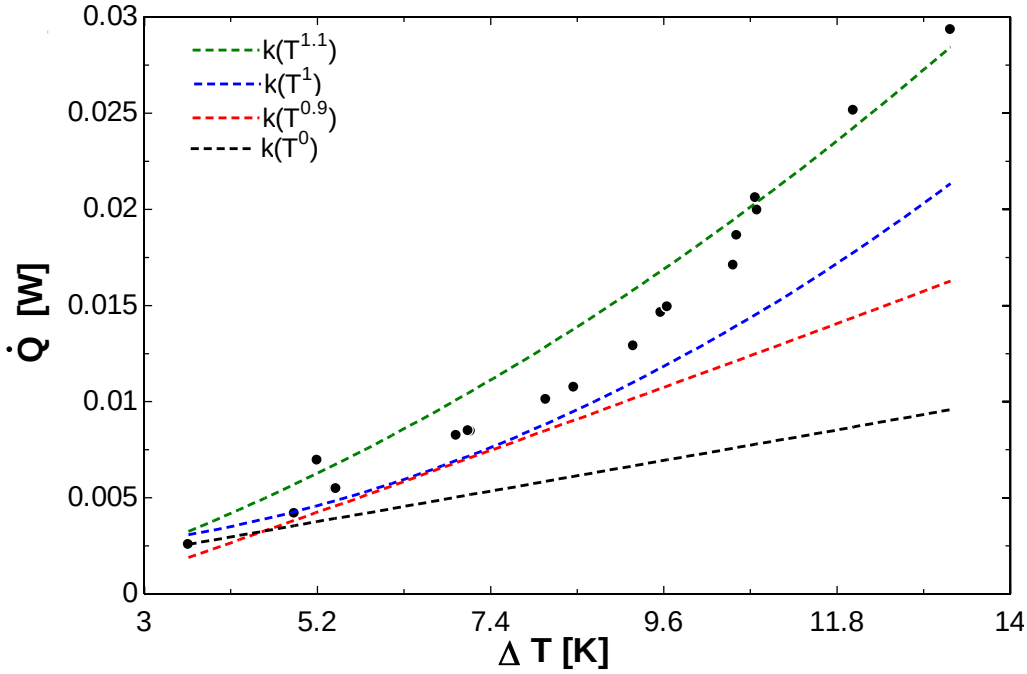

Figure 5.11. Thermal conductivity test results.

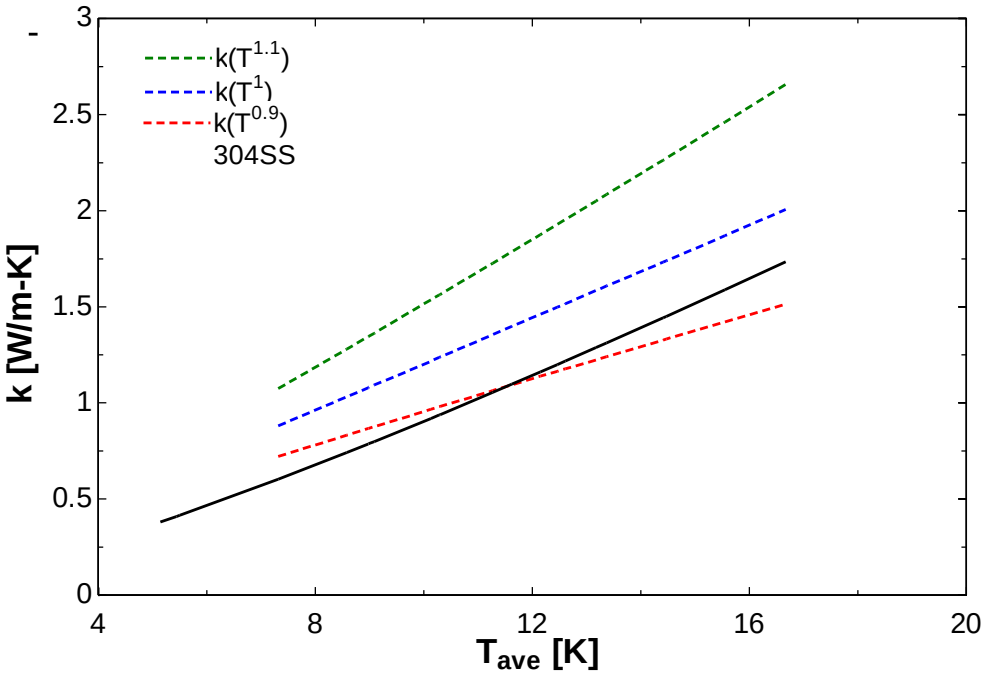

Figure 5.12. Thermal conductivity of 1006-1008 carbon steel as a function of average test temperature.

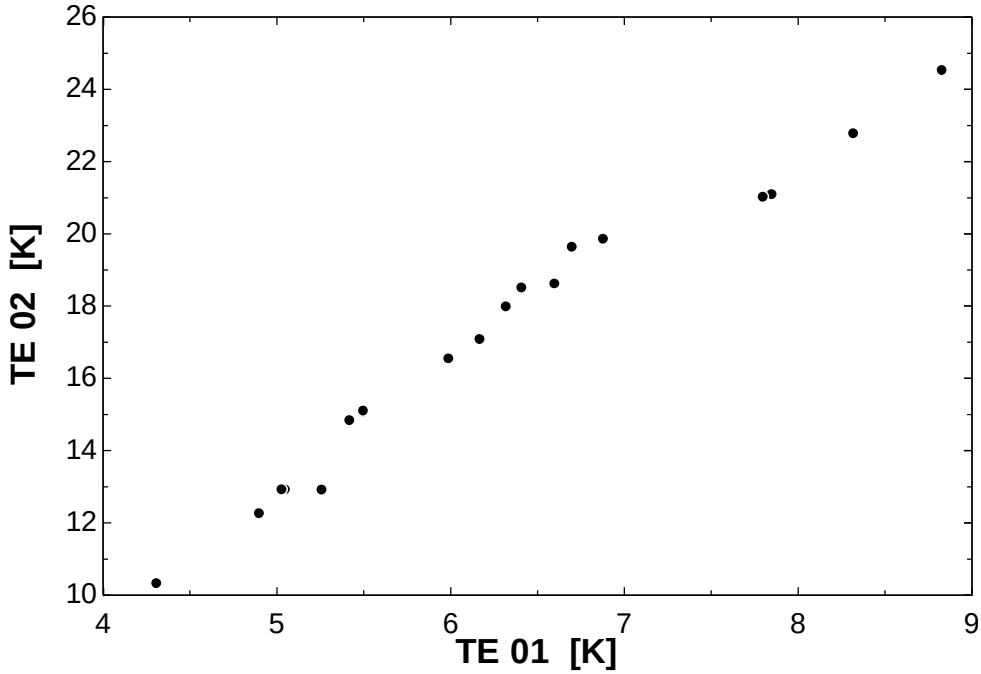

Figure 5.13. Temperature response of thermal conductivity test.

The poor conductivity of the steel core is not ideal, but it is not expected to pose a serious problem during normal operation because of the low heat loads anticipated. If the conductivity of the steel shows itself to be an issue, an adjustment in the material should be made for future cores (discussed further in section 5.4). Presently, the middle section of the core is machined separately from the poles. The poles (1 in FIGURE 5.14) need to be steel or iron for their ~50% flux contribution, but the center body (2 in FIGURE 5.14) provides a minimal contribution to the magnetic field. The updated bracketing structure between the core and the beam chamber (seen in FIGURE 5.15) only connects to the center body but results in face contact with the poles. There is a thin G10 spacer between the bracket and the end face of the core that mainly serves for electrical isolation and the only contact with the beam chamber is due to point contact with alumina ceramic spheres. If the connection were changed to place a spacer or other thermal break between the bracket and the end of the core, eliminating face contact with the poles while maintaining good thermal contact between the body and the bracket/beam chamber, the center

core material to could change without impacting the magnetic field (as modeled in section 5.4). Instead of a center made of steel, the core could be machined from 1100 aluminum (conductivity of ~50W/m-K at 4.2 K) or 6063 aluminum (conductivity of ~30 W/m-K at 4.2 K). With the poles isolated from the conduction load from the beam chamber, the only significant load the windings would NbTi windings would experience is radiation. Thermal contraction of the aluminum away from the poles would likely be mitigated by the epoxy used to pot the windings, creating numerous parallel conduction paths from the core body to the superconducting wire.

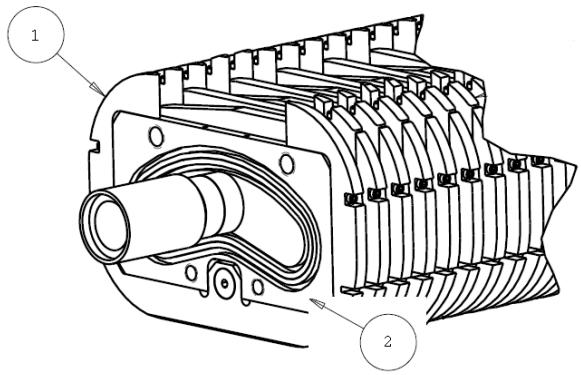

Figure 5.14. Superconducting undulator core.

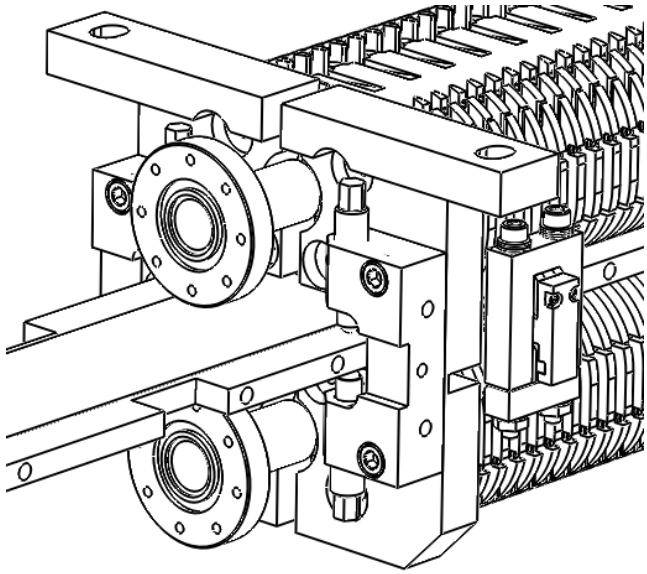

Figure 5.15. Bracket connection to SCU core from beam chamber.

5.3 Lack of Flow/Stagnation

Based on the experiment performed in chapter 4, the anticipated heat loads will induce flow in the thermosiphon. It is instructive to compare the available cooling without flow to that when flow is generated. There will always be some minimal heat load present on the SCU cores, whether it is from radiation or conduction, and vapor will form. If helium is stagnant and not flowing, the primary path for heat to flow away from the core will be conduction through the 304 stainless steel piping and the stagnant helium.

Assuming perfect thermal contact and ignoring any contact resistance through the flange fittings or bellows, the thermal resistance of the steel is defined by

$$R_{cond} = \frac{L}{k * A_c} \tag{5.13}$$

In the case of the SCU, L is ~ 0.508 m, the conductivity k is ~0.3 W/m-K, and the cross sectional area A_c is ~90.3 mm^2. The thermal resistance of the steel is then 11,258 K/W. The parallel conduction path through with the same length as before, a conductivity of k= 0.0186 W/m-K, and a cross sectional area A_c of ~193.5 mm^2 has an associated thermal resistance of 140,344 K/W. These two resistances combined result in an overall conduction resistance of 10,422 K/W. This is in stark comparison with the convection cooling from the flowing thermosiphon. The thermal resistance from convection is defined by

$$R_{conv} = \frac{1}{h * A_s} \tag{5.14}$$

with h being the heat transfer coefficient (~75 W/m^2-K) and A_s being the surface area of the channels in the core (~104.5 in^2) . The convective thermal resistance is 0.395 K/W. This is significantly lower than the idealized conduction path and indicates how important the convective heat transfer is.

5.4 Finite Element Analysis and Design Modifications

Using the heat transfer coefficient predicted in section 5.1 and the conductivity of the 1008 steel, a finite element analysis (performed in ANSYS 12.1) of the core has been conducted to predict the maximum pole temperature. The geometry was simplified to eliminate the cuts, holes, and bolts present in the actual assembly. To model for worst-case conditions, perfect thermal contact between all the faces was allowed and the alumina ceramic bearings that space the brackets around the beam chamber have represented as cylinders to allow for better contact and elemental modeling. The boundary condition inside the helium channel is a heat transfer coefficient of 75 W/m-K to 4.2 K. The surfaces of the ceramic bearings were set to 10 K to simulate the anticipated operating beam chamber temperature and 30 K to simulate a beam injection accident [4-5]. The model also included radiation to 30 K from the surrounding shield

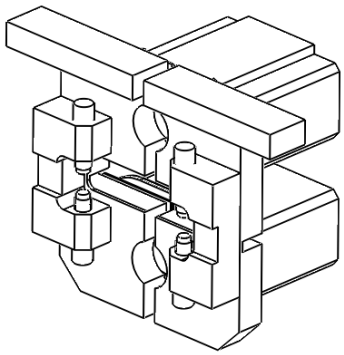

Figure 5.16a. Simplified bracket geometry used in FEA.

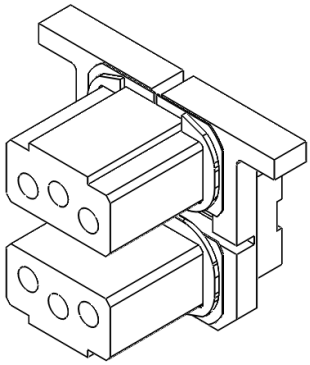

Figure 5.16b. Simplified core geometry used in FEA.

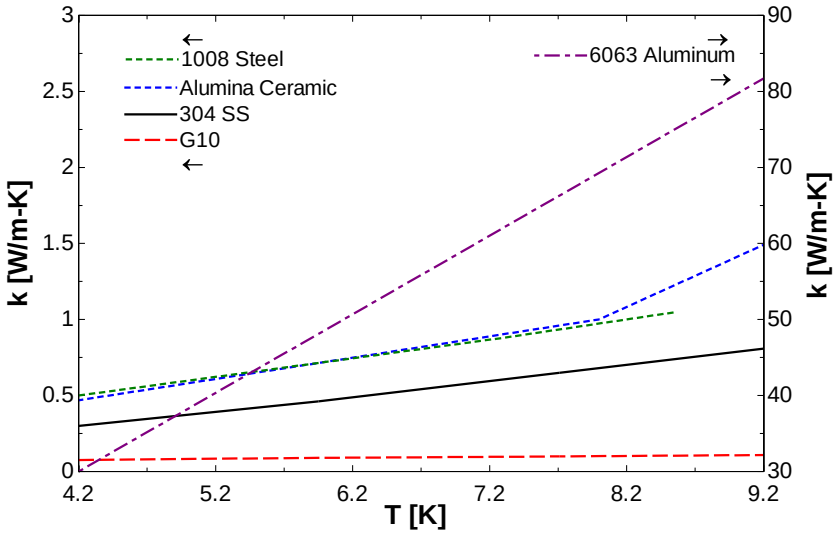

Figure 5.17. Temperature dependent thermal conductivities used in FEA. 6063 Aluminum uses right axis, all other materials use left.

and assumed an emissivity of 1; however this load has a negligible effect. The temperature dependent thermal conductivity data can be seen in FIGURE 5.17.

Since the end-most pole is the one most likely to quench from conductive heat transfer, maintaining this location below 6 K (the current sharing temperature of the NbTi coils on the SCU) should prevent the magnet from going normal. For a beam chamber temperature of 10K, the maximum temperature on the first SCU pole is 4.6 K. The resulting temperature profile can

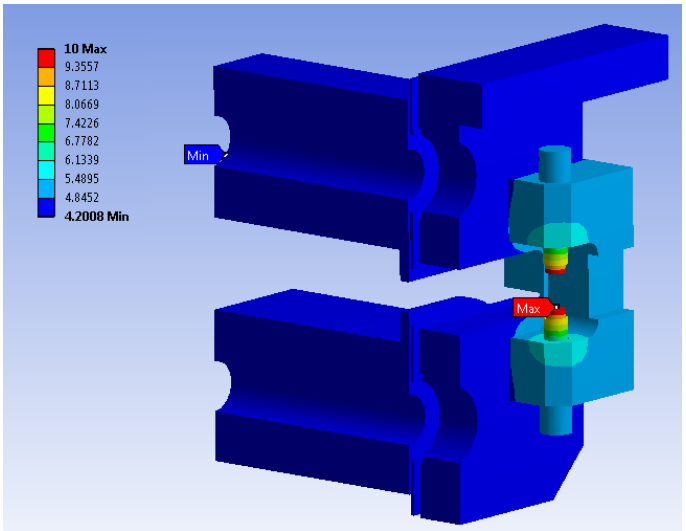

Figure 5.18. Temperature profile of SCU core and bracket with a beam chamber temperature of 10 K.

be seen in FIGURE 5.18. If a beam injection accident occurs, however, the maximum pole temperature is 8.5 K.

One option for reducing the pole temperature is to use an alternative material with a higher thermal conductivity. The poles themselves have to be steel or iron, but as discussed earlier the body has minimal contribution to the magnetic field and could be changed. At 4.2 K, 6063-T5 Aluminum has a thermal conductivity near 30 W/m-K. Using aluminum as the core materials in the model reduced the maximum pole temperature slightly to 4.4 K and 7.6 K at beam chamber temperatures of 10 K and 30 K, respectively.

In an effort to prevent quenching even in the case of a beam injection accident, three additional design modifications were explored. In the first, the core was extended further than the first pole before connecting to the bracket, creating a space between the pole and the G10 sheet used for electrical isolation on the bracket (see FIGURE 5.19). The adjustment was modeled with the extension protruding 3.18 mm and 12.7 mm from the end pole. The second modification incorporated an extension on the mounting bracket that only meets with the core and not the pole. The G10 isolation sheet is trimmed as well, effectively creating distance between the face of the pole and the face of the bracket (see FIGURE 5.20). The final modification increased the width of the G10 isolation sheet to 12.7 mm. Results are presented in TABLE 5.1. Creating space between the end-pole and the bracket clearly has performance advantages, as does using an aluminum core.

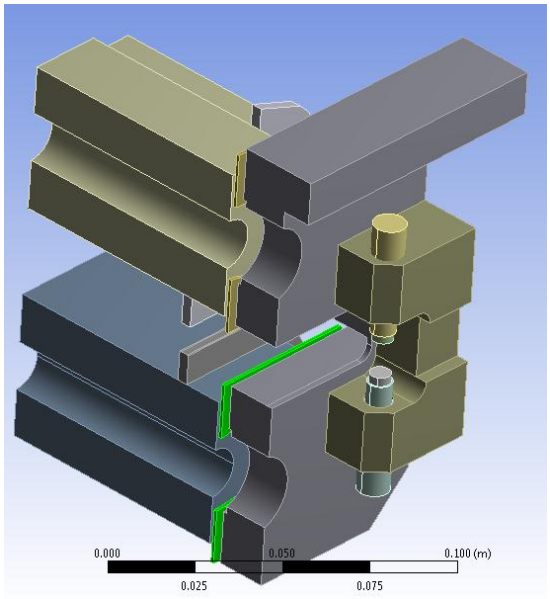

Figure 5.18. Design modification extending the core past the first pole.

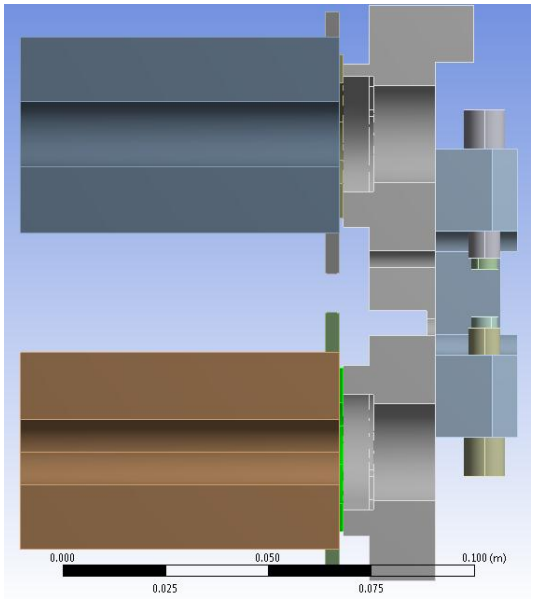

Figure 5.19. Design modification extending the bracket and trimming any face contact with the end poles.

Core Material	Modification	Beam Chamber Temperature (K)	Maximum Pole Temperature (K)	Horizontal Heat Load to Magnet (W)*
1008 Steel	None	10	4.6	0.198
1008 Steel	None	30	8.5	1.57
6063 – Al	None	10	4.4	0.205
6063 – Al	None	30	7.6	1.65
1008 Steel	3.18 mm Core Extension	10	4.4	0.195
1008 Steel	3.18 mm Core Extension	30	7.6	1.50
6063 – Al	3.18 mm Core Extension	10	4.25	0.203
6063 – Al	3.18 mm Core Extension	30	4.85	1.60
1008 Steel	12.7 mm Core Extension	10	4.3	0.195
1008 Steel	12.7 mm Core Extension	30	6.35	1.48
6063 – Al	12.7 mm Core Extension	10	4.21	0.203
6063 – Al	12.7 mm Core Extension	30	4.75	1.60
1008 Steel	6.3 mm Bracket Extension	10	4.4	0.182
1008 Steel	6.3 mm Bracket Extension	30	7.6	1.27
6063 – Al	6.3 mm Bracket Extension	10	4.22	0.19
6063 – Al	6.3 mm Bracket Extension	30	4.75	1.32
1008 Steel	12.7 mm G10 Spacer	10	4.4	0.17
1008 Steel	12.7 mm G10 Spacer	30	6.8	0.9
6063 – Al	12.7 mm G10 Spacer	10	4.22	0.17
6063 – Al	12.7 mm G10 Spacer	30	4.6	0.94

Table 5.1. Finite element analysis results table. *Note: horizontal heat load to magnet result is for conduction load of the entire magnet assembly and not just the quarter symmetry model. The radiation heat load is not included. Assuming a shield temperature of 30 K results in 16 mW distributed over the entire magnet assembly.

5.5 References

1. Flynn, T., *Cryogenic Engineering: Second Edition, Revised and Expanded*, CRC Press, 2004.
2. Powell, R.L., and Childs, G.E., in *American Institute of Physics Handbook: Third Edition*, Gray, D.E., ed., McGraw-Hill, New York, 1972.
3. Ho, C.Y., et al, *Journal of Physics and Chemical Reference Data*, Volume 7, 1978.
4. Petra, M. and Kustom, B., "Sources of Dynamic Heat Load for the Superconducting Undulator," internal APS note, November 2004.
5. "RDK-408S 10K Cryocooler Capacity Map," Sumitomo Heavy Industries.
6. "Multi-layer Insulation (MLI)," thermalengineer.com, http://www.thermalengineer.com/library/effective_emittance.htm, accessed July 29, 2011.
7. "Using MLI blankets under poor vacuum conditions," Meyer Tool and Manufacturing, http://www.mtm-inc.com/reduce_project_risk/using_mli_blankets_under_poor_vacuum_conditions/, accessed July 29, 2011.
8. Reed, R.P., and Clark, A.F., *Materials at Low Temperatures*, American Society for Metals, Metals Park, Ohio, 1992, pp. 140.

6 Summary and Conclusions

6.1 Thermosiphon Design and Experiment

The thermosiphon cooling loop has been developed and experimentally verified to provide a good approach for maintaining the superconducting undulator windings below their current sharing temperature despite the large impact of minor losses on the system's effectiveness or the low quality flow conditions that will be generated. On the average, the flow rates generated from both horizontal and vertical heat application agree well with model predictions. When heating is applied only along the horizontal channels of the assembly, significant flow variations occur due to vapor intermittently being released from the exit of the test section. This hydrodynamic instability could have unwanted thermal effects in the SCU's core and windings. Improved flow stability can be achieved by applying heat at a low power ratio to the vertical return leg of the thermosiphon network, but depending on the liquid level location relative to the return standpipe in the helium reservoir, a percolation-like instability present may still exist. This coupled instability, generated in the horizontal leg but witnessed in the vertical return tubing, can be eliminated by maintaining the helium level in the reservoir above the vertical return pipe.

It should be noted that there is a notable lack of two-phase heat transfer correlations in saturated liquid helium above the lambda point. The low qualities anticipated have allowed for predictions based on the Dittus-Boelter correlation by adjusting the heat transfer coefficient to only include a contribution from the liquid flowing in the channels. Past studies of vertical thermosiphons have suggested that such methods tend to under-predict natural circulation by up to a factor of 2 because they do not take into account the flow being hydrodynamically and thermally developing along the entire path [1] nor the contributions from nucleate boiling [2]. In

any event, the method used for the horizontal design of the SCU insertion device is both valid and conservative, which is important given the experimental nature of the design.

6.2 SCU Considerations

Beyond verifying the operation of the thermosiphon loop, several other results relating to the superconducting undulator's operation can be reported. First, the thermal conductivity of 1006-1008 low carbon steel at 4.2 K is significantly lower than anticipated. This is likely due to the cold rolling process during manufacture. 1020 steel, that also has a relatively low carbon percentage but is annealed after being formed, is predicted to have higher conductivity at cryogenic temperatures.

Even with the core's reduced thermal conductivity, under normal operating conditions the superconducting windings should not go normal. If a beam injection accident occurs, the likelihood increases but there are several design recommendations to mitigate the problem. First and foremost is to eliminate face contact between the end most pole and anything connected to the bracket. Leaving a space between the end-pole and the bracket will create the electrical isolation intended by the G10 spacer but eliminate any thermal pathway. Second, and having a greater impact, the core material could change to something with higher thermal conductivity like 1100 or 6063 aluminum. Finally, based on the finite element model that includes generous thermal contact between all surfaces, the anticipated horizontal heat load is reduced to ~0.2 W under normal operating conditions and ~1.5 W in the case of an injection accident. The reduced horizontal load suggests that the vertical return heater will be very important for maintaining flow in the SCU cores.

6.3 References

1. Jeng, H.R., and Pan, C., "Analysis of Two-Phase Flow Characteristics in a Natural Circulation Using the Drift-Flux Model Taking Flow Pattern Change and Sub-Cooled Boiling into Consideration," *Annals of Nuclear Energy*, Volume 26, Issue 14, pp. 1227-1251, September 1999.
2. Baudouy, B., Benkheira, L., Souhar M., "Heat Transfer Characteristics of Two-Phase He-I (4.2 K) Thermosiphon Flow," *International Journal of Heat and Mass Transfer*, Volume 50, pp. 3534-3544, 2007.

7 Appendices

7.1 Drawings

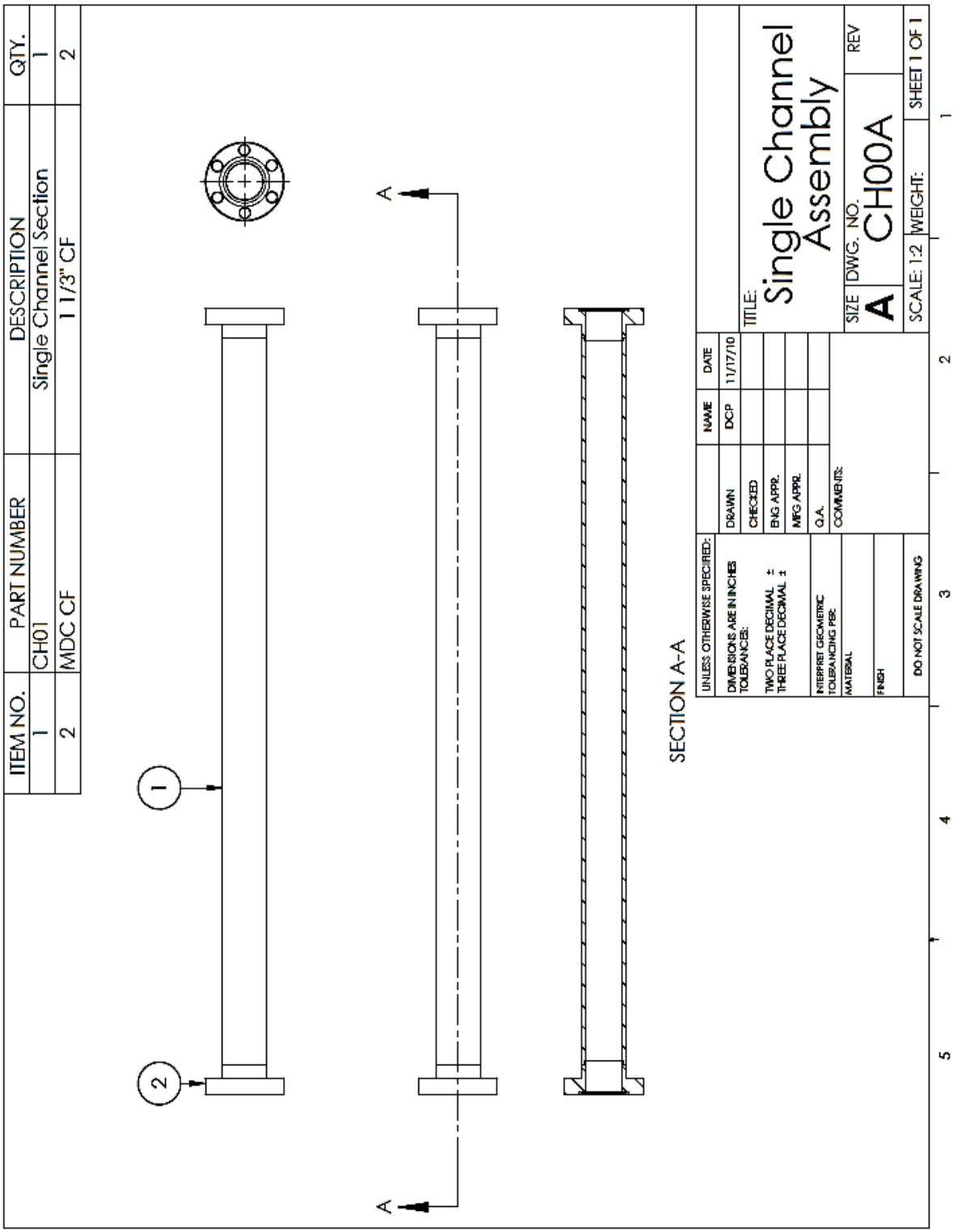

ITEM NO.	PART NUMBER	DESCRIPTION	QTY.
1	MDC CF	1 1/3" CF	2
2	CH05	Plenum Back	2
3	CH02	3 Channel Main	3
4	CH03	3 Channel End	1
5	CH04	Plenum Flat	2
6	FE00B	Venturi Assembly for 3 Channel	1

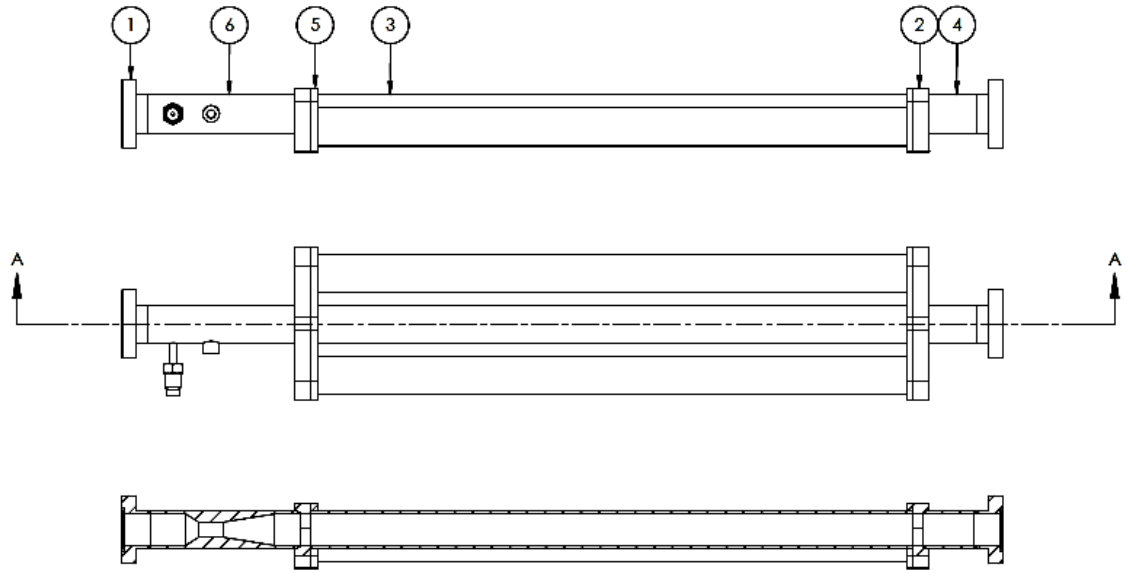

SECTION A-A

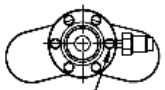

NOTE:
CF THRU-HOLES MUST BE CONCENTRIC AND ORIENTATED AS SHOWN WITH RESPECT TO TAP CONNECTIONS

UNLESS OTHERWISE SPECIFIED:		NAME	DATE
DIMENSIONS ARE IN INCHES TOLERANCES: TWO PLACE DECIMAL ± THREE PLACE DECIMAL ±	DRAWN	DCP	11/6/10
	CHECKED		
	ENG APPR.		
	MFG APPR.		
INTERPRET GEOMETRIC TOLERANCING PER:	Q.A.		
MATERIAL 304 SS	COMMENTS:		
FINISH			
DO NOT SCALE DRAWING			

TITLE: 3 Channel Assembly

SIZE B | DWG. NO. CH00B | REV

SCALE: 1:2 | WEIGHT: | SHEET 1 OF 1

USED ON	PART NUMBER	DESCRIPTION	QTY.
CH00A	CH01	Single Channel Section	1

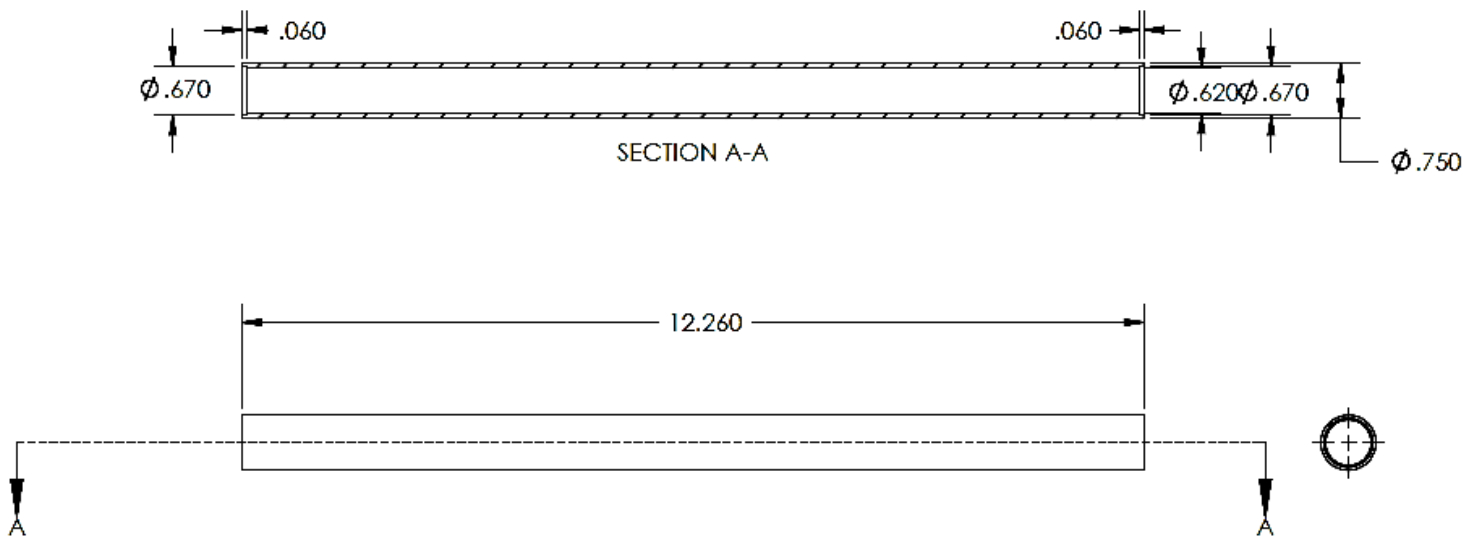

UNLESS OTHERWISE SPECIFIED:		NAME	DATE
DIMENSIONS ARE IN INCHES TOLERANCES: TWO PLACE DECIMAL ±	DRAWN	DCP	11/5/10
	CHECKED		
	ENG APPR.		
	MFG APPR.		
INTERPRET GEOMETRIC TOLERANCING PER:	Q.A.		
MATERIAL 304 SS	COMMENTS:		
FINISH			
DO NOT SCALE DRAWING			

TITLE: Single Channel Section

SIZE	DWG. NO.	REV
A	CH01	
SCALE: 1:2	WEIGHT:	SHEET 1 OF 1

5 4 3 2 1

USED ON	PART NUMBER	DESCRIPTION	QTY.
CH00B	CH02	3 Channel Section	3

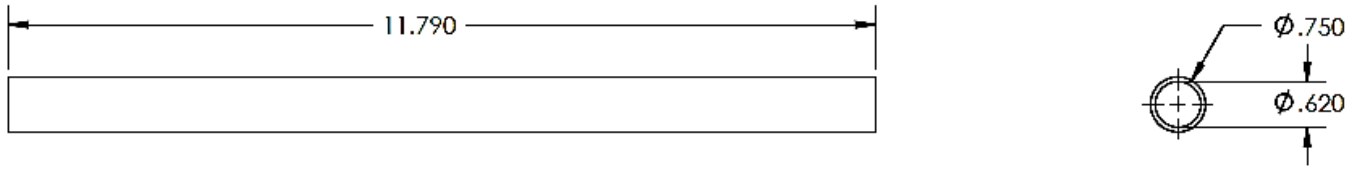

UNLESS OTHERWISE SPECIFIED:		NAME	DATE
DIMENSIONS ARE IN INCHES TOLERANCES: TWO PLACE DECIMAL ±	DRAWN	DCP	11/5/10
	CHECKED		
	ENG APPR.		
	MFG APPR.		
INTERPRET GEOMETRIC TOLERANCING PER:	Q.A.		
MATERIAL	COMMENTS:		
FINISH			
DO NOT SCALE DRAWING			

TITLE: 3 Channel Section

SIZE	DWG. NO.	REV
A	CH02	
SCALE: 1:2	WEIGHT:	SHEET 1 OF 1

5 4 3 2 1

USED ON	PART NUMBER	DESCRIPTION	QTY.
CH00B	CH03	3 Channel End	1

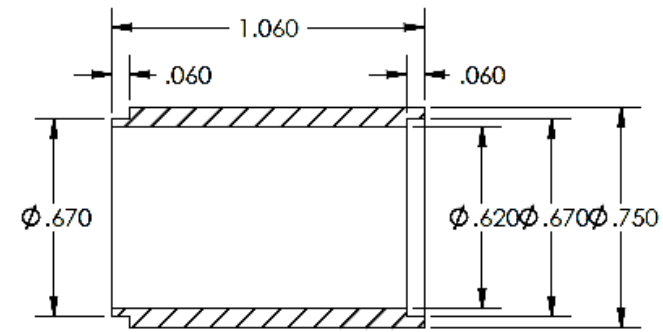

SECTION A-A

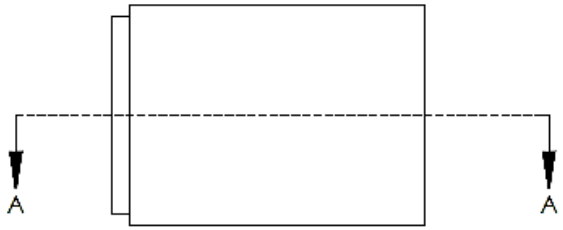

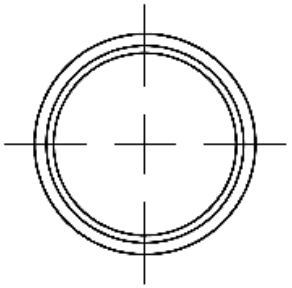

UNLESS OTHERWISE SPECIFIED:		NAME	DATE
DIMENSIONS ARE IN INCHES TOLERANCES: TWO PLACE DECIMAL ±	DRAWN	DCP	11/5/10
	CHECKED		
	ENG APPR.		
	MFG APPR.		
INTERPRET GEOMETRIC TOLERANCING PER:	Q.A.		
MATERIAL 304 SS	COMMENTS:		
FINISH			
DO NOT SCALE DRAWING			

TITLE:

3 Channel End

SIZE	DWG. NO.	REV
A	CH03	
SCALE: 2:1	WEIGHT:	SHEET 1 OF 1

5 4 3 2 1

USED ON	PART NUMBER	DESCRIPTION	QTY.
CH00B	CH04	Plenum Flat	2

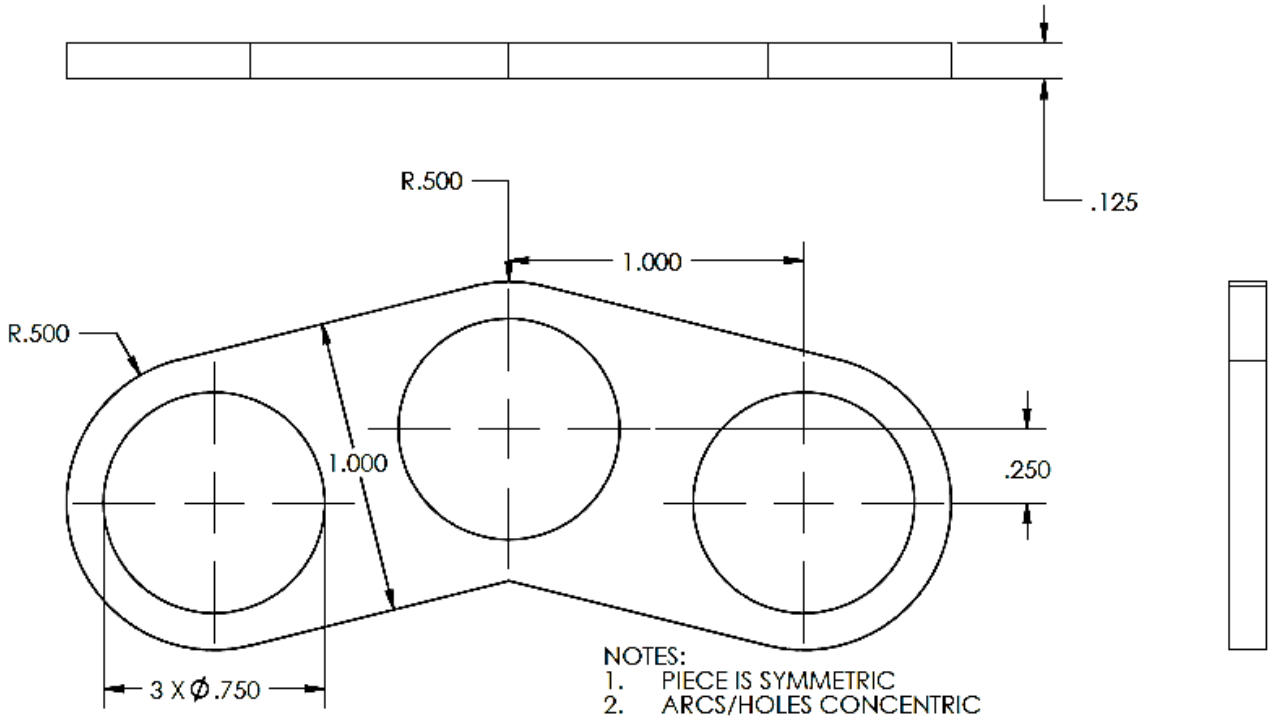

NOTES:
1. PIECE IS SYMMETRIC
2. ARCS/HOLES CONCENTRIC

UNLESS OTHERWISE SPECIFIED:		NAME	DATE
DIMENSIONS ARE IN INCHES TOLERANCES: TWO PLACE DECIMAL ± THREE PLACE DECIMAL ±	DRAWN	DCP	11/5/10
	CHECKED		
	ENG APPR.		
	MFG APPR.		
INTERPRET GEOMETRIC TOLERANCING PER:	Q.A.		
MATERIAL	COMMENTS:		
FINISH 304 SS			
DO NOT SCALE DRAWING			

TITLE: Plenum Flat

SIZE	DWG. NO.	REV
A	CH04	
SCALE: 2:1	WEIGHT:	SHEET 1 OF 1

5 4 3 2 1

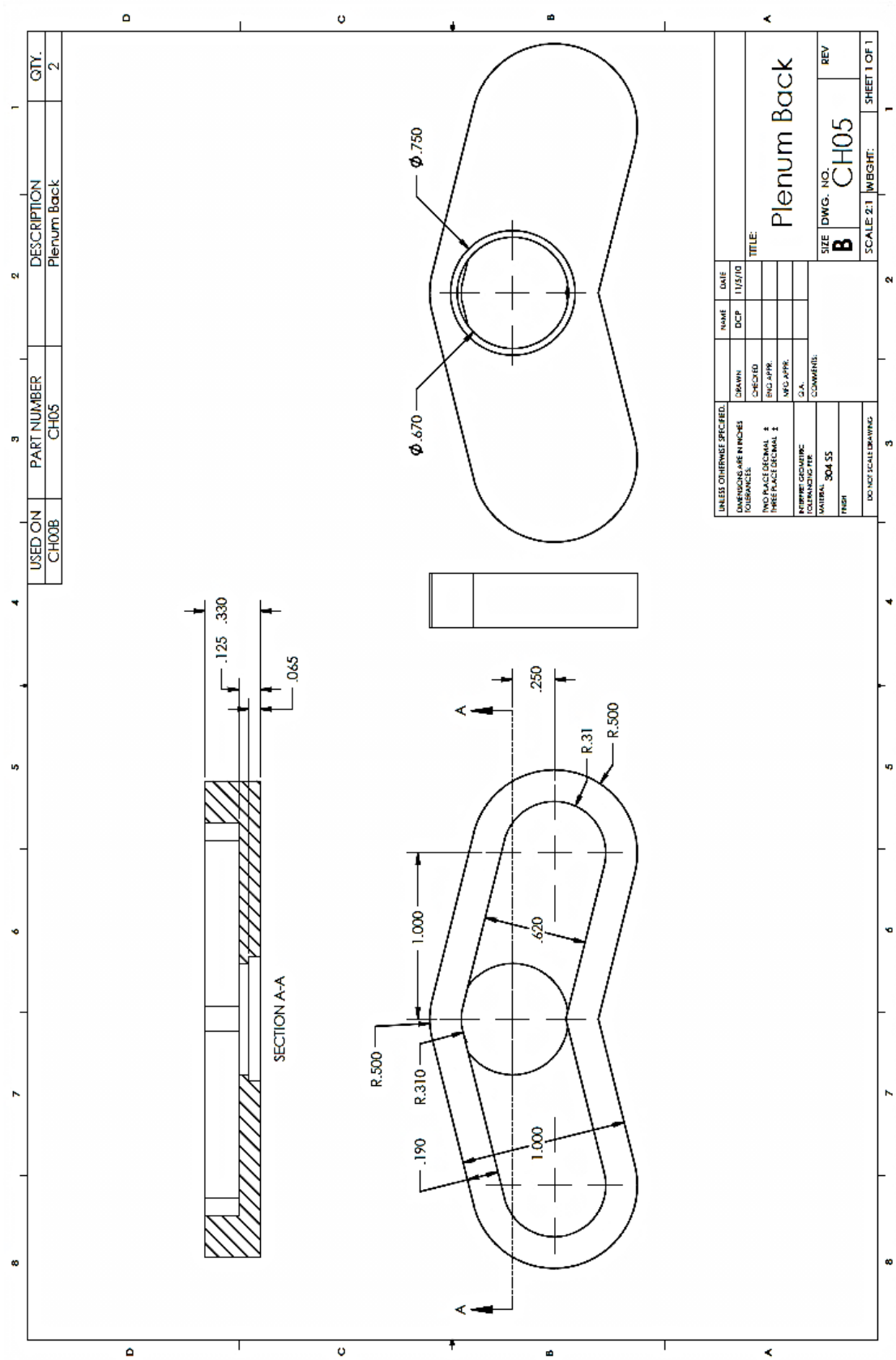
USED ON
CH00B
PART NUMBER
CH05
DESCRIPTION
Plenum Back
QTY.
2
Ø.750
Ø.670
.125
.330
.065
SECTION A-A
A
A
.250
R.31
R.500
1.000
.620
R.500
R.310
.190
1.000
UNLESS OTHERWISE SPECIFIED:
DIMENSIONS ARE IN INCHES
TOLERANCES:
TWO PLACE DECIMAL ±
THREE PLACE DECIMAL ±
INTERPRET GEOMETRIC
TOLERANCING PER:
MATERIAL
304 SS
FINISH
DO NOT SCALE DRAWING
NAME
DATE
DRAWN
DCP
11/5/10
CHECKED
ENG APPR.
MFG APPR.
Q.A.
COMMENTS:
TITLE:
Plenum Back
SIZE
B
DWG. NO.
CH05
REV
SCALE: 2:1
WEIGHT:
SHEET 1 OF 1

ITEM NO.	PART NUMBER	DESCRIPTION	QTY.
1	FE01A	Venturi Body with CF's	1
2	6LV-2-VCR-3S-2TB7	1/8" Long Tube Butt Weld Gland	1
3	FE02	Throat Tap Connection	1
4	MDC CF	1 1/3" CF	2
5	SS-2-VCR-4	1/8" Male Nut	1

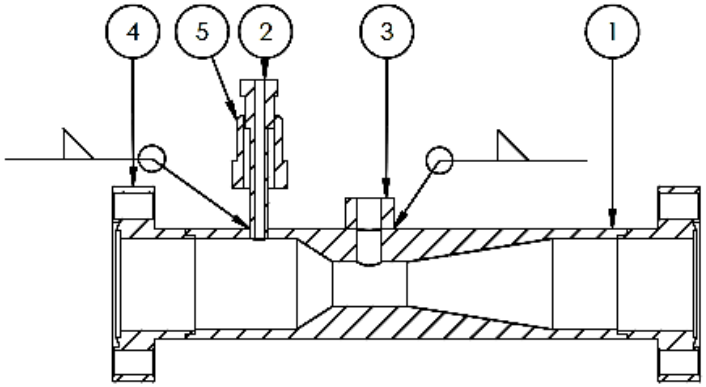

SECTION A-A
SCALE 1 : 1

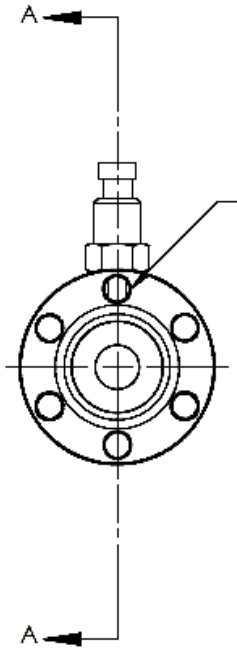

NOTE:
CF THRU-HOLES MUST BE CONCENTRIC AND ORIENTATED AS SHOWN WITH RESPECT TO TAP CONNECTIONS

UNLESS OTHERWISE SPECIFIED:		NAME	DATE
DIMENSIONS ARE IN INCHES TOLERANCES: TWO PLACE DECIMAL ± THREE PLACE DECIMAL ±	DRAWN	DCP	11/17/10
	CHECKED		
	ENG APPR.		
	MFG APPR.		
INTERPRET GEOMETRIC TOLERANCING PER:	Q.A.		
MATERIAL	COMMENTS:		
FINISH			
DO NOT SCALE DRAWING			

TITLE:
Venturi Assembly with CFs

SIZE	DWG. NO.	REV
A	FE00A	
SCALE: 1:2	WEIGHT:	SHEET 1 OF 1

5 4 3 2 1

USED ON	ITEM NO.	PART NUMBER	DESCRIPTION	QTY.
	1	FE01B	Venturi Body for 3 Channel	1
	2	FE02	Throat Tap Connection	1
	3	6LV-2-VCR-3S-2TB7	1/8" Long Tube Butt Weld Gland	1
	4	SS-2-VCR-4	1/8" Male Nut	1
CH00B	-	FE00B	Venturi Assembly for 3 Channel	1

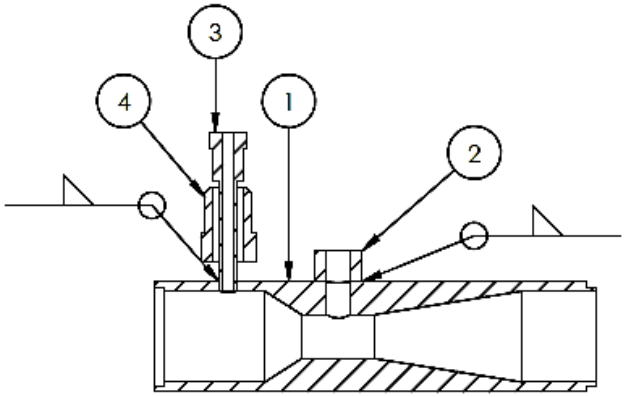

SECTION E-E
SCALE 1 : 1

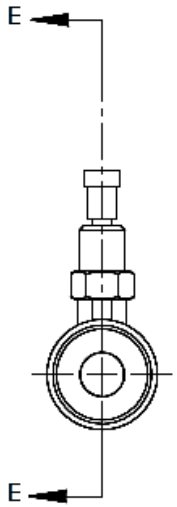

NOTES:
1. VENTURI THROAT TAP THREAD: M5 X .8

UNLESS OTHERWISE SPECIFIED:		NAME	DATE
DIMENSIONS ARE IN INCHES TOLERANCES: FRACTIONAL ± ANGULAR: MACH ± BEND ± TWO PLACE DECIMAL ± THREE PLACE DECIMAL ±	DRAWN	DCP	11/2/10
	CHECKED		
	ENG APPR.		
	MFG APPR.		
INTERPRET GEOMETRIC TOLERANCING PER:	Q.A.		
MATERIAL	COMMENTS:		
FINISH			
DO NOT SCALE DRAWING			

TITLE:
Venturi Assembly for 3 Channel

SIZE	DWG. NO.	REV
A	FE00B	
SCALE: 1:2	WEIGHT:	SHEET 1 OF 1

5 4 3 2 1

USED ON	PART NUMBER	DESCRIPTION	QTY.
FE00A	FE01A	Venturi Body for CF's	1

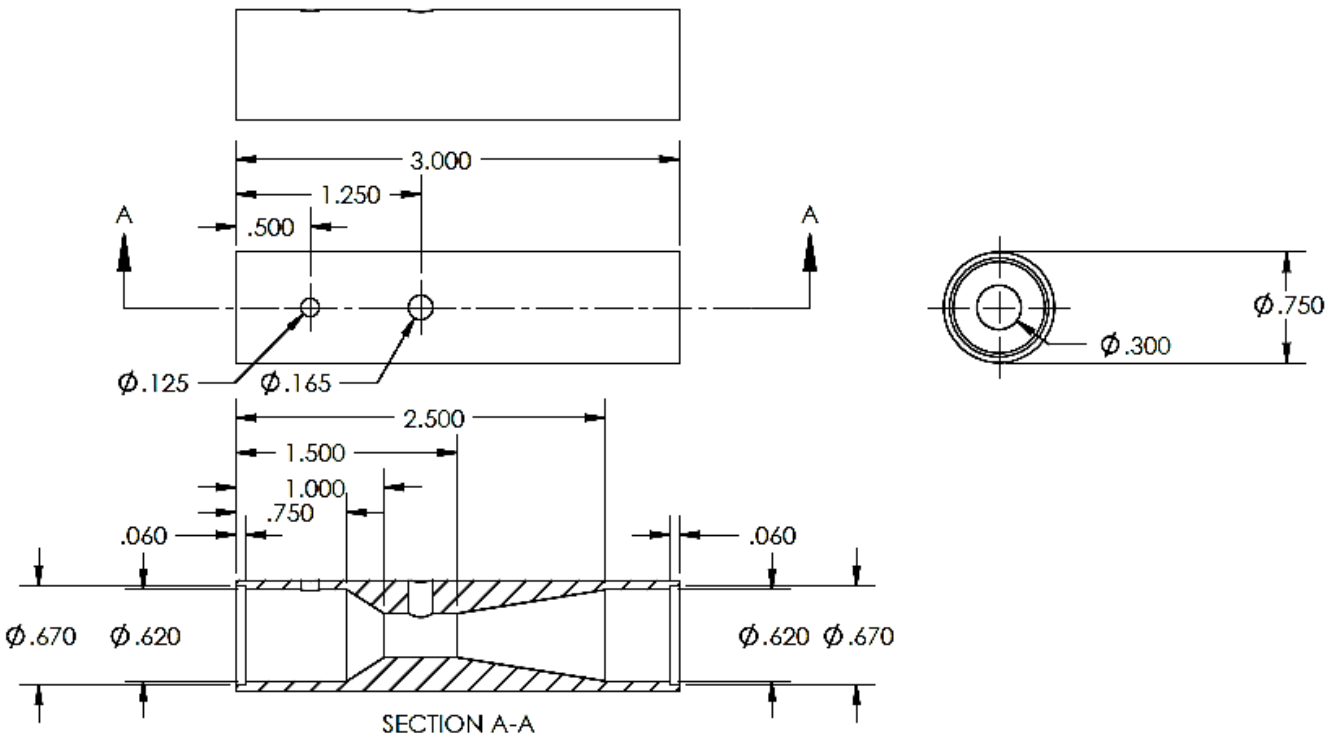

UNLESS OTHERWISE SPECIFIED:		NAME	DATE
DIMENSIONS ARE IN INCHES TOLERANCES: TWO PLACE DECIMAL ± THREE PLACE DECIMAL ±	DRAWN	DCP	11/17/10
	CHECKED		
	ENG APPR.		
	MFG APPR.		
INTERPRET GEOMETRIC TOLERANCING PER:	Q.A.		
MATERIAL 304 SS	COMMENTS:		
FINISH			
DO NOT SCALE DRAWING			

TITLE: Venturi Body for CF's

SIZE	DWG. NO.	REV
A	FE01A	

SCALE: 1:1 | WEIGHT: | SHEET 1 OF 1

5 4 3 2 1

USED ON	PART NUMBER	DESCRIPTION	QTY.
FE00B	FE01B	Venturi Body for 3 Channel	1

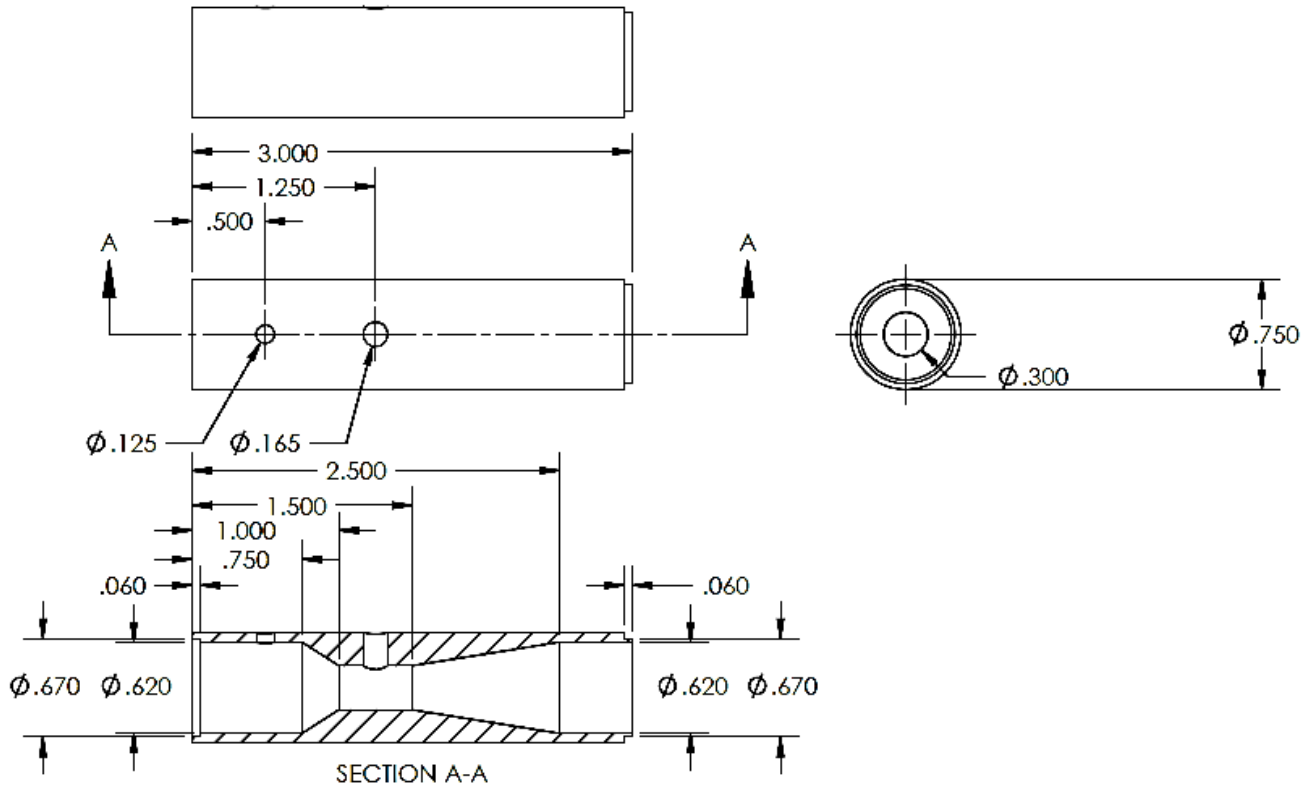

UNLESS OTHERWISE SPECIFIED:		NAME	DATE
DIMENSIONS ARE IN INCHES TOLERANCES: TWO PLACE DECIMAL ±.01	DRAWN	DCP	11/2/10
	CHECKED		
	ENG APPR.		
	MFG APPR.		
INTERPRET GEOMETRIC TOLERANCING PER:	Q.A.		
MATERIAL 304 SS	COMMENTS:		
FINISH			
DO NOT SCALE DRAWING			

TITLE: Venturi Body for 3 Channel

SIZE	DWG. NO.	REV
A	FE01B	

SCALE: 1:1 | WEIGHT: | SHEET 1 OF 1

5 4 3 2 1

USED ON	PART NUMBER	DESCRIPTION	QTY.
FE00A FE00B	FE02	Throat Tap	2

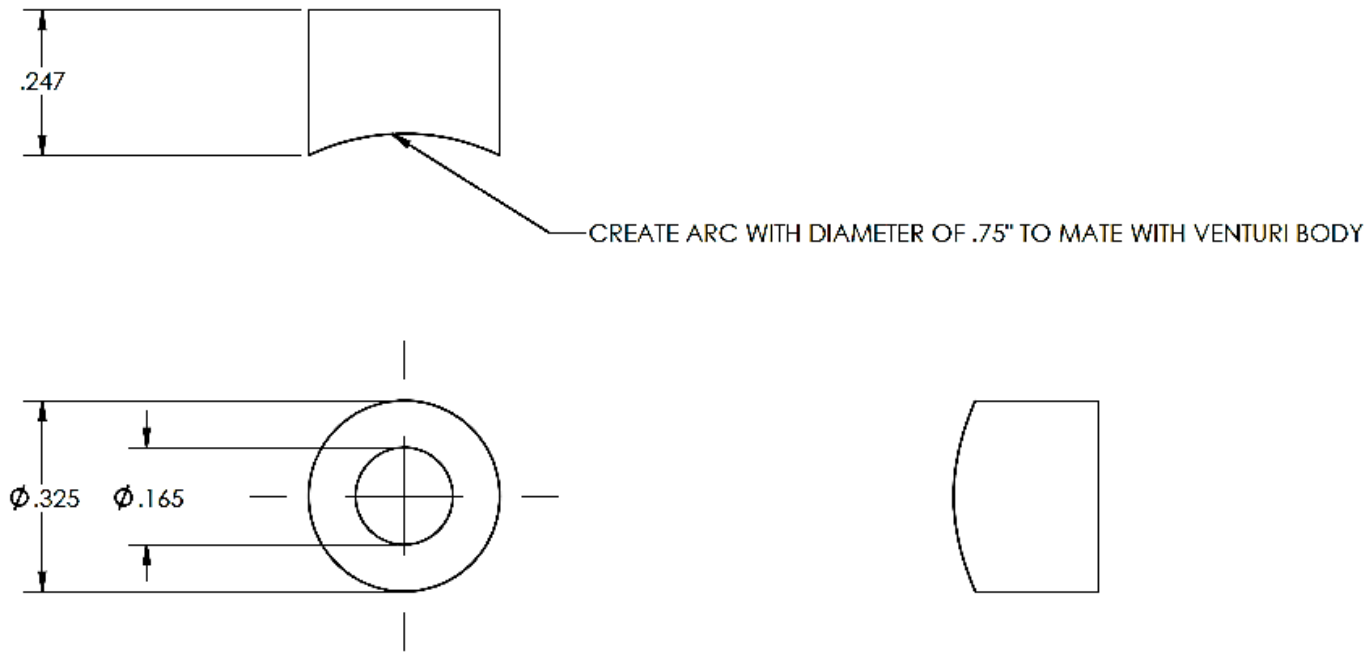

		NAME	DATE
UNLESS OTHERWISE SPECIFIED:			
DIMENSIONS ARE IN INCHES TOLERANCES: TWO PLACE DECIMAL ±.01	DRAWN	DCP	11/2/10
	CHECKED		
	ENG APPR.		
	MFG APPR.		
INTERPRET GEOMETRIC TOLERANCING PER:	Q.A.		
MATERIAL 304 SS	COMMENTS:		
FINISH			
DO NOT SCALE DRAWING			

TITLE:

Throat Tap

SIZE	DWG. NO.	REV
A	FE02	
SCALE: 8:1	WEIGHT:	SHEET 1 OF 1

5 4 3 2 1

ITEM NO.	PART NUMBER	DESCRIPTION	QTY.
1	CT-190	Kulite Pressure Sensor CT-190	1
2	-	1/16" OD 304 SS, .02" ID Overall Length 12"	1
3	SS-2-VCR-1	1/8" Female Nut	1
4	SS-1-VCR-3	1/8" x 1/16" Socket Weld Gland	1

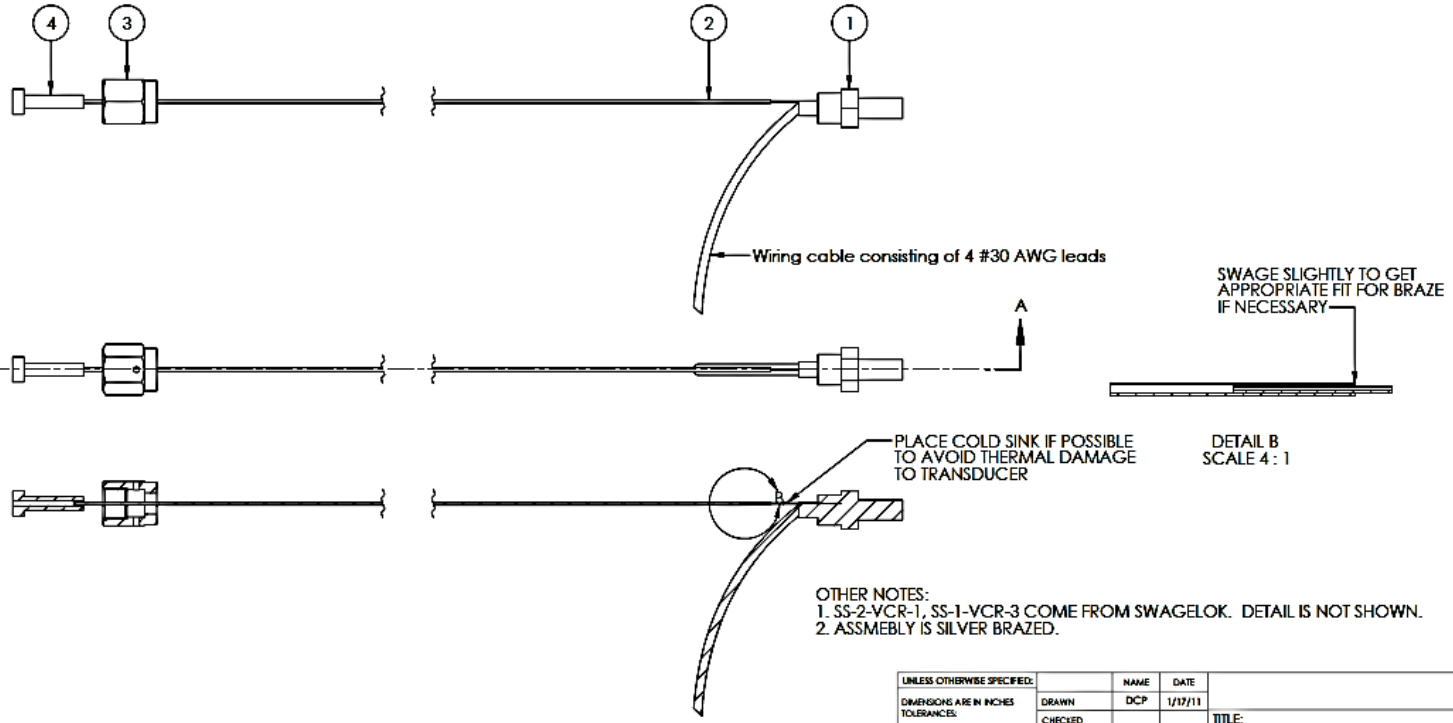

OTHER NOTES:
1. SS-2-VCR-1, SS-1-VCR-3 COME FROM SWAGELOK. DETAIL IS NOT SHOWN.
2. ASSMEBLY IS SILVER BRAZED.

UNLESS OTHERWISE SPECIFIED:		NAME	DATE
DIMENSIONS ARE IN INCHES TOLERANCES: TWO PLACE DECIMAL ± THREE PLACE DECIMAL ±	DRAWN	DCP	1/17/11
	CHECKED		
	ENG APPR.		
	MFG APPR.		
INTERPRET GEOMETRIC TOLERANCING PER:	Q.A.		
MATERIAL	COMMENTS:		
FINISH			
DO NOT SCALE DRAWING			

TITLE: Kulite Assembly

SIZE	DWG. NO.	REV
B	PT01	

SCALE: 1:1 WEIGHT: SHEET 1 OF 1